ANALYSIS OF CORROSION PRODUCTS

IN STRESS CORROSION CRACKS

by

THOMAS PHILIP NIKIFORUK

B.A.Sc. University of British Columbia, 1973

A THESIS SUBMITTED IN PARTIAL FULFILMENT OF THE

REQUIREMENTS FOR THE DEGREE OF

MASTER OF APPLIED SCIENCE

in the Department

of

METALLURGY

We accept this thesis as conforming to the

required standard

THE UNIVERSITY OF BRITISH COLUMBIA

April, 1976

In presenting this thesis in partial fulfilment of the requirements for

an advanced degree at the University of British Columbia, I agree that

the Library shall make it freely available for reference and study.

I further agree that permission for extensive copying of this thesis

for scholarly purposes may be granted by the Head of my Department or

by his representatives. It is understood that copying or publication

of this thesis for financial gain shall not be allowed without my

written permission.

Department of   Metallurgy

The University of British Columbia
Vancouver 8, Canada

Date   July 9th, 1976

ABSTRACT

Circumferentially notched rods of three types of austenitic stainless steel were stress corroded under freely corroding conditions at their yield stress in boiling 154°C MgCl$_2$, and boiling MgCl$_2$ with additions of HCl, CoCl$_2$, and FeCl$_3$. Alloy types 304, 316, and 310 were chosen because of their known different stress corrosion susceptibility. The corrosion products formed on the stress corrosion fracture surface were analyzed by electron diffraction and energy dispersive x-ray analysis.

Electron diffraction of corrosion products, both in situ and stripped from the fracture surface, showed the corrosion product was a spinel oxide in all cases. Qualitative x-ray analysis of corrosion products, in situ and stripped from the fracture surface, indicated the corrosion product formed on all alloys was enriched in chromium and contained lesser amounts of the elements iron, nickel, silicon, molybdenum, magnesium, phosphorous and chlorine.

Observations led to the conclusion that the corrosion product formed in the cracks of the various alloys was similar, being predominantly a chromium enriched oxide spinel with possible traces of metal chlorides or a corundum type oxide. The presence of the spinel oxide was consistent with anticipated E-pH equilibrium within the crack. However, it was felt the variation in s.c.c. behaviour between the different alloys could not be adequately accounted for in terms of the composition of the oxide.

ACKNOWLEDGMENT

TABLE OF CONTENTS

- v -

LIST OF TABLES

LIST OF FIGURES

1. INTRODUCTION

Austenitic stainless steels are notoriously susceptible to stress corrosion cracking (s.c.c.) in the presence of hot aqueous chloride solutions. Such environments frequently occur in the chemical industry where chloride residuals or contaminants are usually present, and the problem has been extensively studied in the laboratory by utilising boiling aqueous solutions of $MgCl_2$. The frequent testing of steels in $MgCl_2$ solutions has been justified because of the generally good correlation with industrial performance. However, despite the many published papers on the subject, few studies have been conducted on the nature of corrosion products on stress corrosion fracture surfaces and their relation to aqueous s.c.c.

In many situations some type of reaction film is considered necessary for s.c.c. [1], [2] process because of its influence on crack geometry and/or localized dissolution. The corrosion films may restrict lateral dissolution and prevent crack blunting, by either forming a passive type film, or by means of noble metal enrichment of the crack walls. The corrosion film may act as a local cathode to a crack tip undergoing anodic dissolution, depending on the environment and crack geometry [3]. The mechanical and electrochemical properties of the corrosion product at the crack tip may be the controlling factor in s.c.c., as is proposed by film rupture/slip step dissolution models [4].

Pourbaix [5] has studied the electrochemical aspects of corrosion in aqueous chloride environments with restricted geometry; pits, crevices, and cracks. He concludes that inside these occluded cells the corrosion of iron should occur with the evolution of hydrogen in an acidified solution saturated in both $FeCl_2 \cdot 4H_2O$ and Fe_3O_4. Latanision and Staehle

[4] proposed a mechanism where the sides of the crack become enriched in the noble element of the alloy, (nickel in the case of stainless steel) thus becoming inactive with respect to the crack tip. Evidence of this occurring has been found for ferritic stainless steels [6] and 304L austenitic stainless steel [3]. Slip dissolution models [7], where cracking occurs by the continuous rupture and reformation of passive films, depend on the mechanical and electrochemical properties of the corrosion product. For example, deformation studies on magnetite films [8] indicate they will crack in tension at strains of 0.05 - 0.08%, and the rate of repassivation may then be a major factor in s.c.c. of steels. Hydrogen cracking models for s.c.c. indirectly depend on the corrosion products. Corroding steel may hydrolyse according to; [3, 9-11]

$$3 \ Fe^{+2} + 4 \ H_2O \rightleftharpoons Fe_3O_4 + 8 \ H^+ + 2e^- \qquad (1)$$
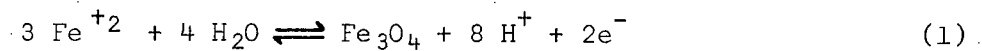
Thus, in aqueous $MgCl_2$ hydrogen ions are produced which are cathodically reduced according to $H^+ + e^- \rightleftharpoons H_{ad}$ and diffuse into the metal. The hydrogen in the metal lattice may precipitate in voids or induce deformation martensite [12] ahead of the crack; propagation of the crack could then occur by either cleavage or preferential dissolution along martensite austenite interfaces. Stress sorption models for s.c.c. require the adsorption of chloride ions onto defect sites at the plastically deforming crack tip, lowering the surface energy of the lattice and resulting in a physical parting of the surface [13]. A corrosion reaction which results in nickel enrichment of the surface will strongly affect the adsorption of chloride ions.

Nielsen [14] studied the role of corrosion products in s.c.c. crack

propagation of austenitic stainless steels in boiling $MgCl_2$ solutions
and concluded their primary effect was to exert a wedging action, which,
together with residual and applied stress was enough to trigger s.c.c.
He isolated the product from the stress corrosion crack by dissolving the
surrounding metal matrix in a solution containing 5% by volume of bromine in
methanol. This left "fan shaped" corrosion products a few hundred angstroms
thick. Electron diffraction patterns of the fans indicated a primarily
spinel M_3O_4 structure with traces of a rhombohedral oxide M_2O_3. He also
noted that the corrosion product underwent a transformation in the electron
beam; an initially "amorphous" area would convert to a microporous area
giving a distinct crystalline pattern. This was interpreted as a loss of
water due to heating effects, with subsequent recrystallization. Chemical
analysis, see Table 1, of the corrosion product, together with the electron
diffraction studies led Nielsen to conclude that the corrosion product was
a hydrated oxide enriched in chromium and deficient in nickel.

The series of events envisioned by Nielsen was as follows: The
corrosion products are deposited a finite distance behind the advancing
crack tip and the subsequent wedging action of the precipitated material
builds up stress within the crack to such a level that crack propagation
occurs. The chloride environment is drawn into the enlarged crack and
further corrosion of local anodes occur. The soluble metal ions migrate
under the electrical field away from the crack tip towards the cathodic
regions, reacting with hydroxide ions to precipitate metal hydroxides.
In the hot solution, the hydroxide would transform to hydrated metal
oxides and the process is repeated.

In the light of recent work by Smith et al.[9], Baker et al.[15],

Table I. Chemical Analysis of Corrosion Product Isolated from Stress Corrosion Cracks in Type 316 Stainless Steel, from Nielsen [14]

Element	wt %	Oxide	wt %
Cr	21.12	Cr_2O_3	30.9
Fe	13.23	Fe_2O_3	18.9
Ni	1.85	NiO	2.36
Mo	1.95	Mo_2O_3	1.49
Mg	-	MgO	-
Si	-	SiO_2	-

Brown [11], and Marek and Hochman [16] which indicate the hot chloride solution at the crack tip to be acidic with a pH 1-3, it is felt that hydroxides could not exist. Further more, although the observation of a spinel film on iron has been observed by others, it is felt that the wedging action of the corrosion products, while being significant, is not necessary for s.c.c. propagation.

Direct work by Birley [17], indirect studies by Baker et al.[15] and work by Staehle [7] indicate the presence of a chromium and iron spinel s.c.c. corrosion product. Staehle and his co-workers have shown for Fe-Cr-Ni alloys, that nickel will preferentially go into solution while chromium and iron will form an oxide film. This film will passivate the stress corrosion crack tip, which in turn will be ruptured by slip step emergence at the crack tip thus repeating the cycle. Baker et al.[15], working with 304 stainless steel in a solution of 67 wt % $MgCl_2 \cdot 6H_2O$, 8 wt % $FeCl_3 \cdot 6H_2O$ and 25 wt % distilled water maintained at a boiling point of 125°C, found that a protective corrosion film formed on the exterior of the sample when the pH was between 1.2 and 2.5, whereas, below pH 1-2 a non-protective film formed. However cracking occurred in both cases. It was found that the pH of the advancing crack was independent of the bulk solution pH and was always in the range of 1.2 - 2.5. The thin corrosion film found in the stress corrosion cracks was assumed to be the same as the films that formed on the exterior surfaces in solutions of the same pH. This film was a poor electrical conducting chromium enriched spinel. To determine the role of film deposition in crack formation, organic compounds were added in order to complex the iron and chromium ions thus preventing film formation.

General corrosion was observed but no precipitate or protective film developed on the specimen surface and no cracks were observed. Baker et al. concluded that a critical pH and a protective poor electrical conducting film were necessary for s.c.c. The pH is maintained by hydrolysis and the oxide film produced confines the electrochemical cell reaction to the crack tip.

Birley [17] in diffraction and chemical analysis studies on 304L and 310 austenitic stainless steels in 45 wt % $MgCl_2$ and $MgCl_2$ + $FeCl_3$ aqueous solutions, found the corrosion product in the s.c.c. crack to be primarily a spinel. Chemical analysis of oxides formed in boiling 45 wt % $MgCl_2$ solutions was not possible due to the thinness of the oxide. Oxides formed in the $FeCl_3$ + $MgCl_2$ solutions (the same as Baker et al.[15]) however, were thick enough to perform chemical analysis; the oxides were primarily iron, chromium, magnesium, and nickel. He concluded the oxide formed in $MgCl_2$ + $FeCl_3$ solutions was an iron enriched spinel with traces of magnesium oxychlorides.

Marek and Hochman [18] have observed by in situ energy dispersive x-ray analysis, a chromium enriched, iron and nickel deficient, corrosion product on the s.c.c. fracture surface of single crystals of 316 austenitic stainless steel in boiling 45 wt % $MgCl_2$ solutions. Davis and Wilde [19] have shown that a passive film does exist on the surface of stainless steels exposed to boiling $MgCl_2$ solutions. Wilde [20] has conducted controlled potential, corrosion and polarization studies on 304 austenitic stainless steels in boiling $MgCl_2$ and $LiCl_2$ solutions which showed a chromium enriched film is formed on the steel surface.

Despite the work of previous authors which support the presence of

an iron and chromium containing spinel in the stress corrosion crack,

no study has been performed on the effect of alloy elements in stainless

steel on the structure and composition of the stress corrosion product.

The austenitic stainless steels, 304, 316 and 310 have varying failure

times in hot chloride solutions at constant temperature and at constant

initial stress level. The nickel, chromium, and molybdenum content vary

in all three, but it's not known if the composition or structure of the s.c.c.

corrosion product varies likewise.

Francombe[21] and Francis [22] have studied the lattice changes in

iron spinels resulting from additions of chromium and nickel. The

normal spinel $(M^{+2})(M^{+3})_2O_4$ has the O^{-2} ions arranged in a face centred

cubic structure, with the M^{+2} ions in the tetrahedral sites and the

M^{+3} ions in the octahedral sites. The unit cell has 56 atoms; 32 oxygen,

8 M^{+2} and 16 M^{+3}. In iron spinels, the M^{+2} ions prefer to situate in

the octahedral sites, thus the structure is an inverse spinel,

$Fe^{+3}(Fe^{+2}Fe^{+3})O_4$. Additions of chromium ions will replace ferrous Fe^{+2}

ions in the octahedral sites with Cr^{+3} and move Fe^{+2} to the tetrahedral

sites. Large additions of chromium will convert the inverse spinel to

a normal spinel, the transition occurring at approximately $Fe_{1.8}Cr_{1.2}O_4$

Further additions of Cr^{+3} will lead to a stoichiometric oxide, $Fe^{+2}(Cr^{+3})_2O_4$,

known as chromite. The change from inverse to normal spinel is accompanied

by a change in lattice parameter (see Fig. 1) and conductivity. Magnetite

has a higher conductivity than chromite due to the presence of both ferric

and ferrous ions in the octahedral sites [37].

Nickel and manganese can also form spinels with iron and chromium;

$NiCr_2O_4$, $NiFe_2O_4$, $MnFe_2O_4$. A solid solution of mixed spinel phases may
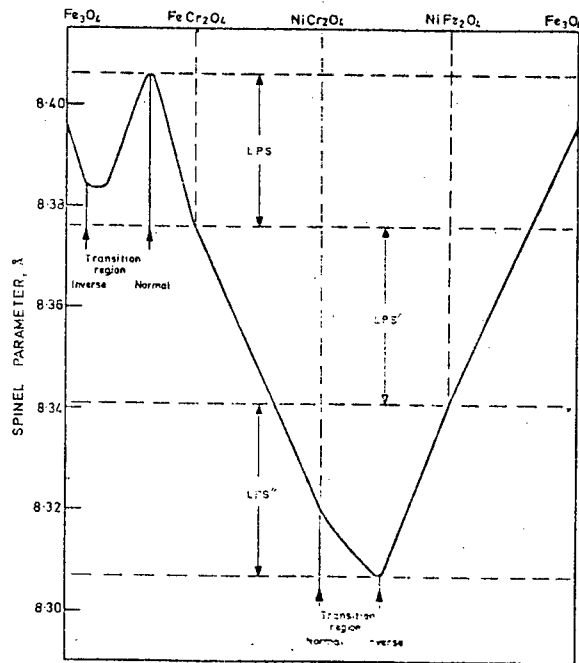
Fig. 1. Lattice parameter variation with composition for Ni, Cr, Fe spinels, from Francis [22].

occur since all types of iron-containing spinels are completely miscible [22]. Any mixture of spinels will result in a variation of lattice parameter of the entire oxide, thus spinel phases cannot be identified solely by electron or x-ray diffraction. Therefore, it is necessary for a chemical analysis to be performed to identify the spinel phase or phases present.

Electron and x-ray diffraction studies of oxide films, both in situ and stripped from the substrate, have been performed by several authors [14,15,17,23]. Transmission electron diffraction is easy and convenient and is applicable to thin and thick oxides. Chemical analysis of oxides can be accomplished in a variety of ways. In the present work, the most convenient and quickest was by means of an energy dispersive x-ray analyzer attachment mounted on a scanning electron microscope (S.E.M.) and a transmission electron microscope (T.E.M.). This allows a quick qualitative analysis for all elements above sodium, atomic number 11. With S.E.M. capabilities it is also possible to analyze selected areas up to approximately 60,000x magnification, making it possible to determine if there are any major composition variations in the oxide.

For the present study circumferentially notched rods of three austenitic stainless steels, 304, 316, and 310 were stress corroded under freely corroding conditions at their yield stress in a boiling aqueous solution containing 45 wt % of $MgCl_2$ (b.p. 154°C). The structure and composition of the resulting corrosion product on the fracture surface was then determined. Additions of HCl, $FeCl_3$ and $CoCl_2$ were made to the basic $MgCl_2$ solution to determine their effect on the oxide. Specimens were also partially cracked in an attempt to examine the solution inside

the stress corrosion crack.

In order to understand the mechanism of s.c.c., maximum information is required regarding the phases present at the crack tip. This study was an attempt to provide further information on the crack tip chemistry.

2. EXPERIMENTAL

2.1 General

Three austenitic stainless steels, 304, 316, and 310, were selected for load relaxation stress corrosion tests in boiling chloride solutions. Circumferentially notched steel rods were placed in the test environment, allowed to reach equilibrium temperature, then loaded until yielding occurred. Following stress corrosion, the fracture surface was washed in hot tap water, dried with ethanol and stored in a desiccator.

Electron diffraction and x-ray spectroscopy of the fracture surface corrosion product was performed in situ on the metal substrate and on the corrosion product stripped from the metal. The technique of Birley and Tromans [12] was employed for diffraction studies of corrosion products in situ, whereby a transmission electron microscope is used as a simple electron diffraction camera. X-ray spectroscopy was conducted with an energy dispersive spectrometer attached to the diffraction chamber of the transmission electron microscope (T.E.M.) and to the specimen chamber of a scanning electron microscope (S.E.M.)

Conventional transmission electron microscopy and diffraction studies were conducted on the stripped oxide films.

2.2 Materials

2.2.1 Steels

The stainless steels were received as 3/8 inch diameter rods. The analyses in weight percent are shown in Table II.

TABLE II: Composition of Stainless Steel

Element	304 wt %	316 wt %	310 wt %
Fe	69.89	65.84	49.82
Cr	18.67	17.92	25.74
Ni	8.91	11.61	21.57
C	0.05	0.045	0.09
Co	0.1	0.1	0.1
Cu	0.2	0.2	0.2
Mn	1.-2.	1.-2.	1.-2.
Mo	0.2	2.0	0.2
Si	0.5-1.0	0.5-1.0	0.5-1.0
V	0.03	0.03	0.03
S	0.006	0.013	0.006

TABLE III: Annealing Data for Stainless Steel

Steel	Temp. °C	Time (hr)	Room Temp. Notch yield stress (psi)
304	1150	1	65,000
316	1150	1	63,500
310	1150	1	69,000

2.2.2 <u>Environments</u>

Four different environments were used in this study;

1) $MgCl_2$ + water

2) $MgCl_2$ + HCl + water

3) $MgCl_2$ + $FeCl_3$ + water

4) $MgCl_2$ + $CoCl_2$ + water

All were made with reagent grade chemicals and distilled water. Tests were conducted at the boiling point of the solutions, temperatures usually fluctuating ± 2°C.

The basic environment was 45 wt % $MgCl_2$ and water (boiling point 154°C). For tests in an acidified solution, lcc of concentrated 37.5% HCl solution was added to 40 cc of the basic $MgCl_2$ solution to give an approximate concentration of 0.3 M/l HCl. The $MgCl_2$ + $FeCl_3$ solution was the same as Birley's [17] and Baker's [15]; 8 wt % $FeCl_3 \cdot 6H_2O$, 67 wt % $MgCl_2 \cdot 6H_2O$, and sufficient distilled water to adjust the boiling point to 125°C. Since $FeCl_3$ will decrease the time to failure, T_f , of austenitic stainless steels in boiling chloride solutions, and Co^{+2} has a higher reduction potential at 25°C than Fe^{+3} [24], then $CoCl_2$ might also decrease T_f . Therefore, $CoCl_2$ was added to $MgCl_2$ to make a solution having the same mole ratio Mg^{+2}/Co^{+2} as the mole ratio Mg^{+2}/Fe^{+3} in the $FeCl_3$ solution. The composition was 17 gr $CoCl_2 \cdot H_2O$, 203 gr $MgCl_2 \cdot 6H_2O$, boiling point 160°C.

2.3 <u>Specimen Preparation</u>

Stress corrosion specimens were 7 inch sections of 3/8 diameter rod, threaded at either end with a centrally located 60° circumferential

notch, machined to a 0.2 inch diameter to localize the s.c.c. The specimens were annealed according to Table III. After annealing, the notched region of each specimen was electropolished at 25-30 volts d.c. in a chromic-acetic acid solution; 25 gr chromic oxide, 133 cc acetic acid, 7 cc water, then stored in a desiccator until tested.

2.4 Stress Corrosion Tests

The stress corrosion tests performed are listed in Table IV. A floor model Instron was used for stress corrosion tests. The specimen and environment were contained in a Pyrex cell with an attached reflux condenser and thermometer, see Fig. 2. Heat was supplied by an electrical heating tape.

The procedure was as follows: The specimen, with the surface outside the notch area covered with Teflon tape, was placed in the Pyrex cell and the ends sealed with Teflon bungs, the lower being fixed tight and the upper one being a loose fit. The cell was wrapped with the heating tape, set in the Instron and connected to the reflux condenser. Turning on the heating tape prior to introducing the environment prevented the solution from freezing on the walls of the cell. The environment was added at its boiling point and the cell allowed to reach thermal equilibrium. This generally took at least 30 minutes. During this time a slight load was applied to counteract the expansion of the specimen due to heating and to monitor when the specimen was in thermal equilibrium with the solution. Upon reaching equilibrium a tensile load was applied to initiate yielding within the notch (see Table III for yield stress) and the crosshead of the

TABLE IV: Stress Corrosion Test Performed

Alloy	Environment	Temp. °C	Type of Test
304	$MgCl_2$ (boiling)	154	s.c.c. full and partial failure
304	$MgCl_2$ + HCl (boiling)	154	s.c.c. full failure
304	$MgCl_2$ + $FeCl_3$ (boiling)	125	s.c.c. full failure
304	$MgCl_2$ + $CoCl_2$ (boiling)	160	s.c.c. full failure
316	$MgCl_2$ (boiling)	154	s.c.c. full failure
316	$MgCl_2$ + HCl (boiling)	154	s.c.c. full failure
316	$MgCl_2$ + $CoCl_2$ (boiling)	160	s.c.c. full failure
310	$MgCl_2$ (boiling)	154	s.c.c. full failure
310	$MgCl_2$ + HCl (boiling)	154	s.c.c. full failure
310	$MgCl_2$ + $CoCl_2$ (boiling)	160	s.c.c. full failure
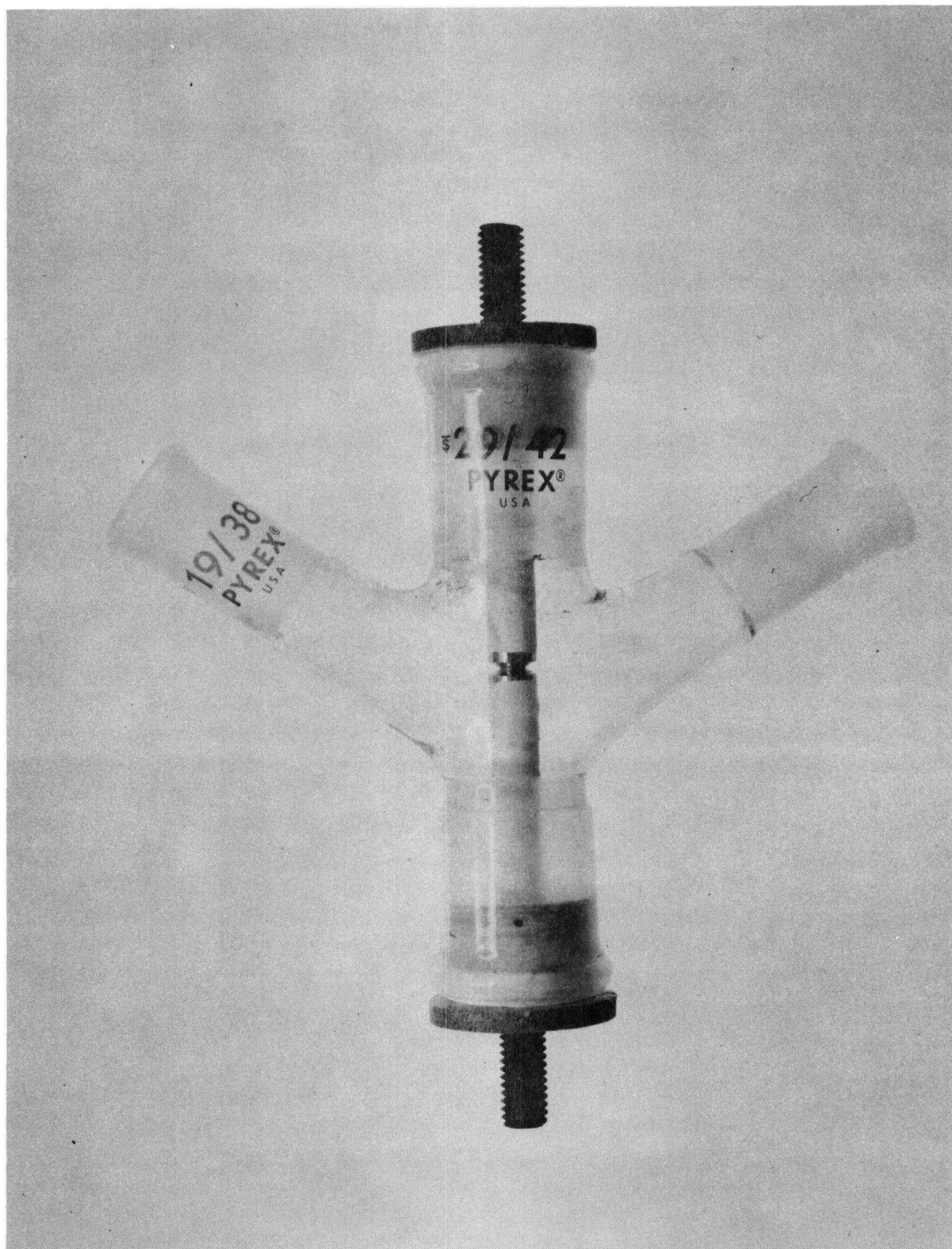
Fig. 2. S.C.C. cell with 7 inch long specimen in place.

Instron then locked. A circumferential stress corrosion crack originated
at the root of the notch and propagated to the centre of the specimen,
relaxing the load to zero, and producing a wholly s.c.c. fracture
surface devoid of overload failure. The specimen was removed from the
environment and the two fracture surfaces washed in hot tap water to remove the
solution, then dried with ethanol prior to storing in a desiccator.
Partially cracked specimens were removed from the environment when
the load had dropped to one-half the initial value. These specimens
were not washed, but placed immediately in a desiccator and later
mechanically fractured in a Hounsfield Tensometer at 25°C, at which
temperature the crack solution is a solid hydrated product and may be
examined in the S.E.M.

2.5 Corrosion Product Stripping

The fracture surface corrosion product was stripped by two different
methods; 1) dissolution of the metal substrate in a bromine-methanol
solution and 2) mechanically stripping the corrosion product with
cellulose acetate.

One of the two fracture surfaces was immersed in a solution of
1 vol % bromine, 99 vol % anhydrous methanol. Nielson [14] used a
5% bromine solution but this is a very aggressive solution and there
was some concern that it might damage the oxide. The 1% bromine solution
was used and was quite satisfactory. After a few hours in the solution
the corrosion product floated free of the metal substrate and was
washed in successive solutions of methanol. Cellulose acetate sheet,
softened in acetone, was pressed onto the other fracture surface and
stripped off when it had hardened. The resulting acetate replica was

coated with carbon, then dissolved in acetone and washed in methanol

leaving a carbon replica with the stripped corrosion product attached.

The two stripping methods, performed on separate fracture surfaces

of the same specimen, provided a means of testing the validity of using

the bromine-methanol method to strip corrosion products for chemical

analysis.

2.6 Electron Diffraction

Electron diffraction studies of the fracture surface corrosion

product, both in situ and stripped, were performed on a 100 kv Hitachi

transmission electron microscope (T.E.M.). Birley and Tromans

[12,17] described the technique for electron diffraction of corrosion

products in situ. The stress corrosion fractured specimen was placed

in the high resolution diffraction stage of the T.E.M. with the

macroscopic s.c.c. fracture plane parallel to the electron beam.

Diffraction patterns were obtained when protuberances on the fracture

surface intersected the electron beam, see Fig. 3. The advantages

of this technique were;

1) it permits examination of the corrosion film without any prior

treatment.

2) there is less likelihood that heating effects from the

electron beam will damage the corrosion product because of the large

heat sink provided by the metal substrate.

3) the relative intensities of the diffraction rings are similar

to those for randomly oriented powders.

Stripped corrosion films were mounted on specimen mounting grids

ELECTRON

BEAM

S.C.C.

FRACTURE

SURFACE

X-RAYS
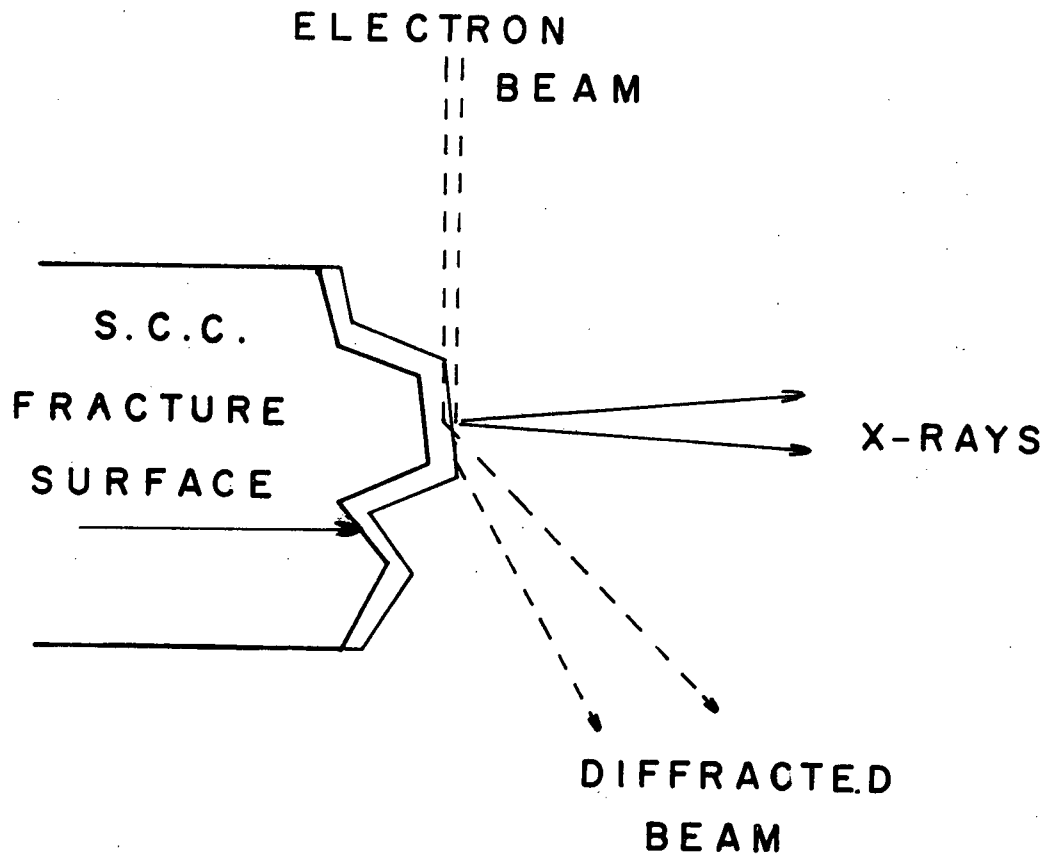
DIFFRACTED

BEAM

Fig. 3. Schematic representation of in situ diffraction of surface oxide
in high resolution diffraction stage of the T.E.M. The primary
electron beam strikes the surface film and is diffracted.

for the T.E.M., then placed in the specimen stage of the microscope and diffraction patterns obtained from selected areas. The chemically stripped films from the 304 and 316 stainless steel fracture surfaces were too thin to be detected in the bromine-methanol solution unless the s.c.c. fracture surface was carbon coated prior to stripping. Upon stripping the carbon floated free with the corrosion product attached.

2.7 X-ray Spectroscopy

2.7.1 Introduction

X-ray spectroscopy was conducted in the T.E.M. and S.E.M. using an Ortec energy dispersive x-ray spectrometer (E.D.S.). The S.E.M. equipped with an E.D.S. is similar to an electron probe. The primary function of the S.E.M. is to produce a high resolution image of the specimen surface. The primary electron beam has a low current and small diameter, approximately 150-200A°. The image is produced by low energy secondary electrons, created when primary electrons knock an orbital electron free from the surface atoms. The x-ray intensity resulting from the excitation by the electron beam of the S.E.M. is lower than the x-ray intensity produced by an electron probe which has a relatively high beam current (10^{-10} Amps vs. 10^{-7} Amps). The detection and identification of the x-rays is the function of the x-ray spectrometer of which there are two types, wavelength dispersive and energy dispersive.

The wavelength dispersive spectrometer (W.D.S.) is based on the Bragg law; $\lambda = 2d_{hkl} \sin\theta$, where d is the interplanar spacing, θ is the angle of diffraction and λ is the wavelength of the radiation.

X-rays originating from the specimen are diffracted by an analyzing crystal of specific interplanar spacing d_{hkl} and monitored by a counting device. Since each element has a set of characteristic x-rays, wavelength λ, elemental analysis can be performed on an unknown specimen by scanning the spectrometer through a range of angles. All elements above beryllium, atomic number 4, can be detected with the use of various diffracting crystals.

Only a small fraction of the x-rays produced will satisfy the Bragg law and be picked up by the collimated counter. Therefore, to achieve a good count rate, a large volume of x-rays must be generated. For this reason, the primary beam must have a high beam current which normally requires a larger diameter and makes the W.D.S. unsuitable for instruments like the S.E.M.

The resolution of the wavelength spectrometer is good, eg. characteristic x-rays 10 eV apart can be separated with high peak to background ratios. The major drawbacks to the W.D.S. are that the complete chemical analysis of an unknown specimen is time consuming and that the specimen surface must be normal to the primary electron beam to ensure high count rates.

Energy dispersive spectrometers separate characteristic radiation according to its energy. This can be achieved with flow proportional counters, or a solid state crystal detector. For the Ortec E.D.S., the detector is a lithium drifted silicon crystal Si(Li),(Ortec series 7000T).

When an x-ray from the specimen hits the Si(Li) crystal, electrons from the silicon atoms are excited. Each excited electron absorbs 3.8 eV of energy. Thus, a single x-ray photon excites many electrons, which

are collected, resulting in a current that is proportional to the energy of the x-ray photon. This current charge is amplified and stored in a multichannel analyzer (M.C.A.) which simultaneously stores the current for every other x-ray striking the Si(Li) crystal. The output of the analyzer is a continuous spectrum of frequency vs. energy for all x-rays striking the crystal. In the present studies an Ortec model 6200 M.C.A. was employed.

The advantages of the E.D.S. are;

1) the entire x-ray spectrum generated may be analyzed and displayed simultaneously, thus total elemental analysis may be done in a few minutes.

2) because no collimation is necessary, a high percentage of x-rays produced are analyzed. This allows the E.D.S. to be operated with the low beam currents associated with scanning electron microscopes.

3) specimen position and topography are not as critical as for wavelength dispersive spectrometers.

The disadvantages are;

1) only elements above sodium, atomic number 11, can be analyzed.

2) resolution is inferior to the W.D.S.; generally only peaks separated by 160 eV or more may be resolved.

3) peak to background ratios are inferior to the W.D.S.

It should be noted that x-ray energy analysis only detects the presence of elements, and conveys no information about their ionic or covalent state. For example chlorine may be present in a corrosion product and one may have to assume it is present as a chloride.

2.7.2 X-ray Spectroscopy of Thin Films

The usual intensity vs concentration corrections associated with x-ray spectroscopy, do not hold for very thin films. The mathematical models that relate intensities to concentrations are based on the assumption that for very thin specimens the x-rays generated by the beam can pass to the surface with negligible absorption and fluorescence. The validity of this has been verified for thin foils used in 40-100 kv transmission electron miscroscopy [25]. In general, if the specimen is transparent in a 100 kv transmission electronbeam, absorption and fluorescence effects can be ignored. The use of the lower electron voltages in the S.E.M. (20-30kv) should increase electron scattering but not affect the absorption of x-rays produced.

In conventional x-ray spectroscopy of thick materials there is no transmitted electron beam and considerable x-ray absorption and fluorescence. Quantitative elemental analysis can be performed by comparing specimen elemental intensities to elemental intensities of standards, and applying correction factors, providing both specimen and standards are excited under similar conditions. For thinner specimens where there are some transmitted electrons the correction factors may still be applied but the standard must be the same thickness as the specimen. For very thin films, while correction factors are negligible, standards must also be the same thickness as the specimen.

For corrosion product films from the fracture surface it is not possible to get an accurate measurement of the film thickness, nor is it possible to obtain a standard which would duplicate the surface topography of the oxide. Since x-ray intensity will vary with thickness

and roughness, as well as composition, quantitative analysis of the stress corrosion fracture surface corrosion product by x-ray spectroscopy is not possible.

Even though quantitative spectroscopy is not possible, semi-quantitative analysis of thin sections can be done. Since x-rays produced in the thin sections are not subject to absorption affects, the intensity ratios of different elements will be proportional to their concentration ratios assuming similar excitation efficiency (excitation efficiency is similar for elements with similar atomic numbers). These ratios, together with diffraction patterns from the corrosion product, provide an adequate means of corrosion product identification.

2.7.3 Mounting of Thin Films for S.E.M. X-ray Spectroscopy

When dealing with thin films it must be remembered that a good portion of the primary beam will pass through the film and strike the specimen holder the film is mounted on. Backscattered electrons will be reflected from the specimen holder back towards the specimen support grid, where they will produce further excitation and generation of characteristic x-rays. Thus, x-rays will be detected from both the support grid and areas remote from the primary electron beam, (see Fig. 4), resulting in misleading analyses. Characteristic x-rays generated from the specimen holder may be eliminated by coating with carbon.

Attempts to avoid this problem involved mounting the stripped corrosion film on a support grid, over a hole in a hollow analytical graphite cylinder. Transmitted electrons striking the bottom of the hollow cylinder will generate backscattered electrons which will be absorbed in the hollow cylinder instead of hitting the corrosion film (see Fig. 4).
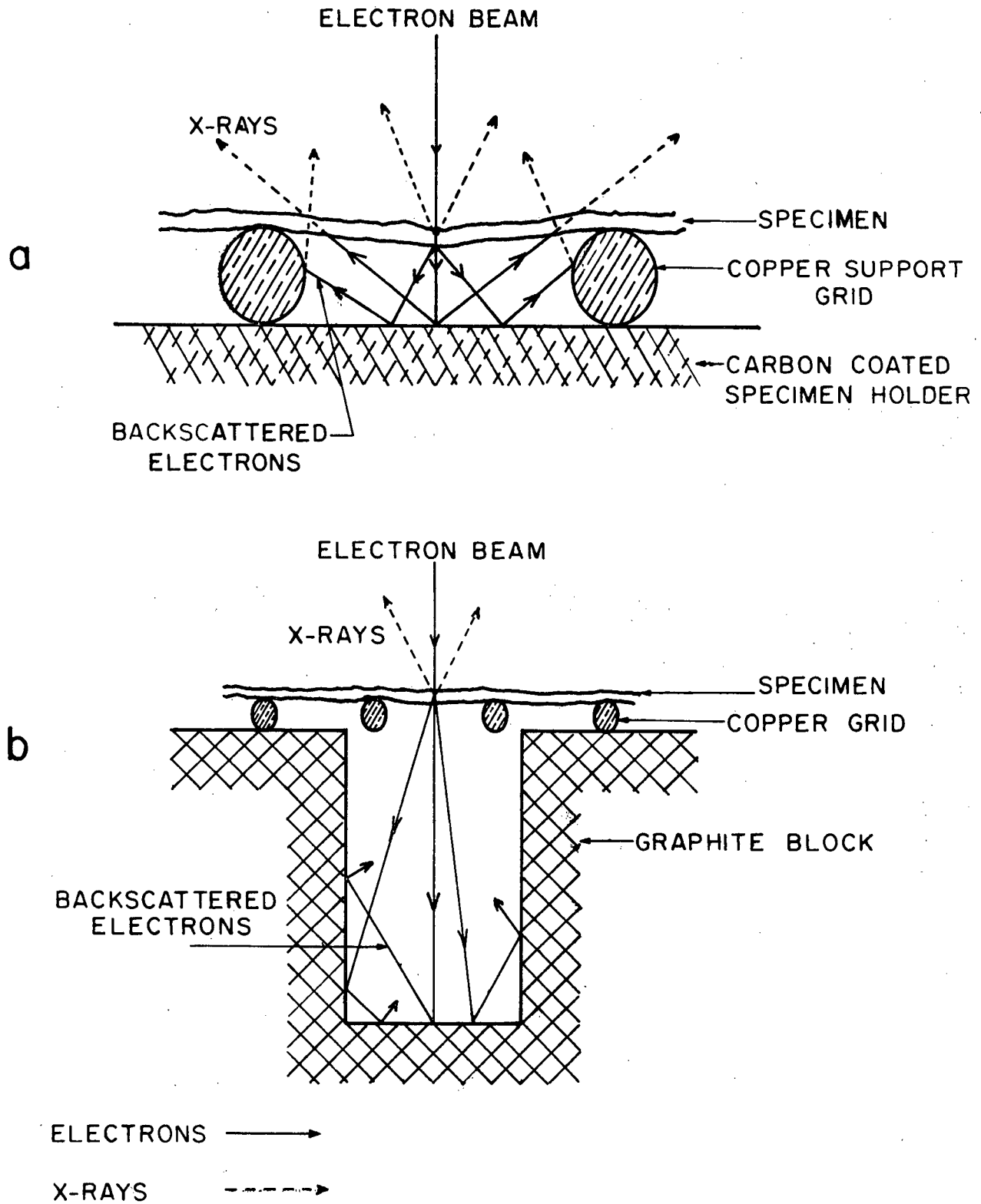
Fig. 4. Schematic diagrams of backscattered electron effect from specimen
holder during x-ray analysis of thin films
a) from conventional specimen holder
b) from hollow graphite block

This did not totally eliminate the backscattered electron and x-ray effect but did improve the situation.

2.7.4 Procedure for X-ray Spectroscopy

X-ray spectroscopy of the corrosion product in situ was performed by placing the stress corrosion fracture surface in the high resolution diffraction stage of the T.E.M. fitted with the Ortec x-ray analyzer. The advantage of this setup was that diffraction patterns and chemical analysis were obtained from the sample in the same piece of equipment. However the surface area covered by the beam in the T.E.M. was larger than the surface area covered by the beam in the S.E.M., thus it was not possible to isolate neighbouring phases of different composition in the corrosion film.

X-ray analysis of the stripped corrosion product was more involved. The stripped product, mounted on specimen grids, was examined by conventional techniques in the T.E.M., where diffraction patterns and surface features were studied, then placed on the hollow graphite cylinder for examination in the S.E.M. With the magnification capabilities of the S.E.M., it was possible to perform x-ray spectroscopy on pre-selected T.E.M. areas that gave good diffraction patterns, thus obtaining electron diffraction patterns and elemental analysis of the same area.

All x-ray analysis, in T.E.M. and S.E.M., was performed with the electron beam voltage set at 20 kv. Qualitative comparison of element intensities was performed by integrating the x-ray peaks over 5 channels (40 eV/channel) and subtracting the background intensity. All quoted Cr/Fe and Cr/Ni ratios were determined in this manner.

3. RESULTS AND OBSERVATIONS

3.1 Stress Corrosion Tests

The results of the stress corrosion tests are summarized in Table V. General stress corrosion fracture surface micrographs are shown in Fig. 5. On a macroscopic scale, the type 310 fracture surfaces were relatively flat, the type 304 fracture surfaces were very irregular, and the type 316 fracture surfaces were similar to type 304. The stress corrosion crack path varied; transgranular for 310 stainless steels, predominantly transgranular with some intergranular for 316, and a mixed mode failure for 304.

The type 310 stress corrosion fracture surfaces had a thick blue-green corrosion deposit. The 304 and 316 fracture surfaces had a shiny straw lustre and did not appear to have a thick corrosion film. These observations were the same for all the specimens tested in the various solutions, except 304 stress corroded in the $MgCl_2$ + $FeCl_3$ solution where a thick red brown corrosion product covered the fracture surface. Stress corroded specimens of 304 allowed to remain in the $MgCl_2$ solution for 40 hours did not form a noticeably thicker corrosion film than specimens removed immediately upon fracture.

The exposed electropolished areas on the surfaces of the specimens were not noticeably affected by the various solutions, except the acidified $MgCl_2$ solution and the $MgCl_2$ + $FeCl_3$ solution. On immersion in the acidified $MgCl_2$ solution the electropolished areas reacted, forming a smooth grey-black corrosion film and producing a steady stream of bubbles, believed to be H_2 gas. No pitting was observed. This reaction slowed and stopped within approximately one hour. The exposed surface

TABLE V: Stress Corrosion Test Results

Steel	# of Spec.	Load (psi)	Environment	Temp. °C.	Time to Failure (min)
304	3	61400/63200/65700	$MgCl_2$	154	74/99/89
304	1	59000	$MgCl_2 + HCl$	154	76
304	1	61000	$MgCl_2 + FeCl_3$	125	150
304	1	72000	$MgCl_2 + CoCl_2$	160	210
316	3	66000/63500/65800	$MgCl_2$	154	200/160/240
316	1	54800	$MgCl_2 + HCl$	154	230
316	1	63400	$MgCl_2 + CoCl_2$	160	250
310	3	85800/82600/82500	$MgCl_2$	154	2130/2436/2172
310	1	71900	$MgCl_2 + HCl$	154	2012
310	1	68900	$MgCl_2 + CoCl_2$	160	1910
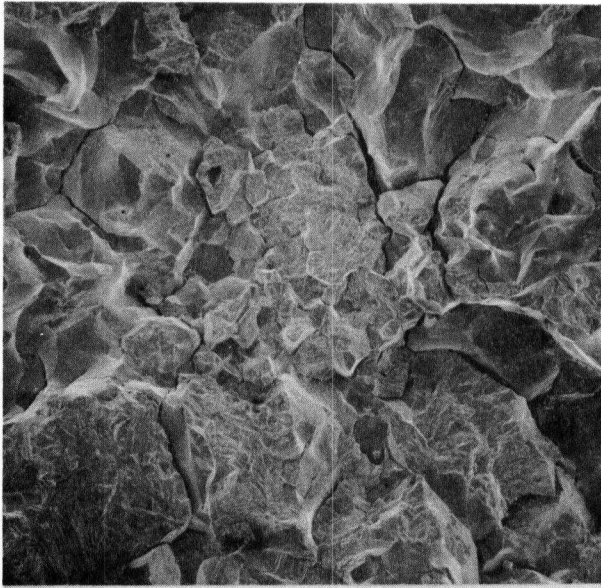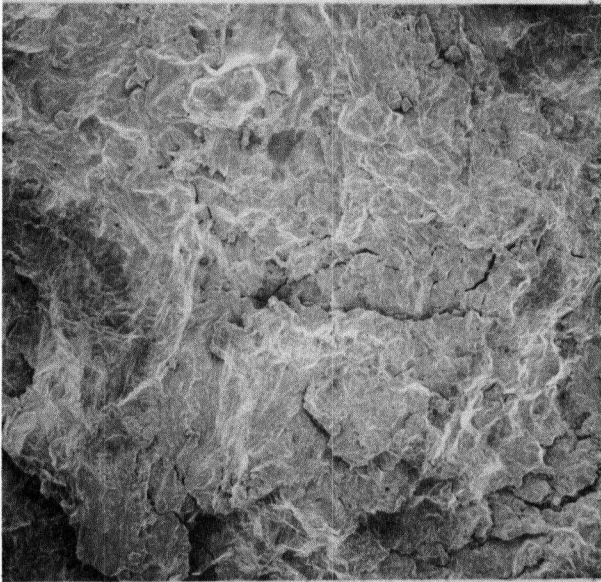
Fig. 5. Representative fractographs (40x magnification) from stainless
steels. a) 304, b) 316, C) 310

areas on the 304 specimen in the $MgCl_2$ + $FeCl_3$ solution were heavily pitted and covered with a rough red brown film spotted with a few small patches of a blue-green colour.

3.2 Stripping of Oxides

3.2.1 Bromine-Methanol Stripping

The bromine-methanol solution removed the corrosion product from the metal substrate within a few hours. The corrosion products on the stress corrosion fracture surfaces of 304 and 316 specimens were so thin that the fracture surfaces had to be coated with an evaporated carbon film; the corrosion product came off the metal substrate attached to the carbon support film. The corrosion product removed from the surface of 310 specimens was a thick sponge, retaining the shape of the fracture surface after the metal substrate had dissolved. The corrosion product morphology from the 310 surface was similar to the oxide observed by Nielsen [14] showing corrosion product fans as well as corrosion spikes (see Fig. 6).

The corrosion films formed on the crack surfaces of 304 and 316 in all environments, except $MgCl_2$ + $FeCl_3$, were very thin. The straw coloured interference colour on the fracture surfaces suggested the film was about 400-500A° thick [26]. Carbon coating the fracture surface prior to stripping was not too successful as there were only a few areas of corrosion product on the carbon films. The product that was picked up was too thin to be visually distinguished on the carbon films, and could only be detected by electron diffraction and x-ray spectroscopy. The
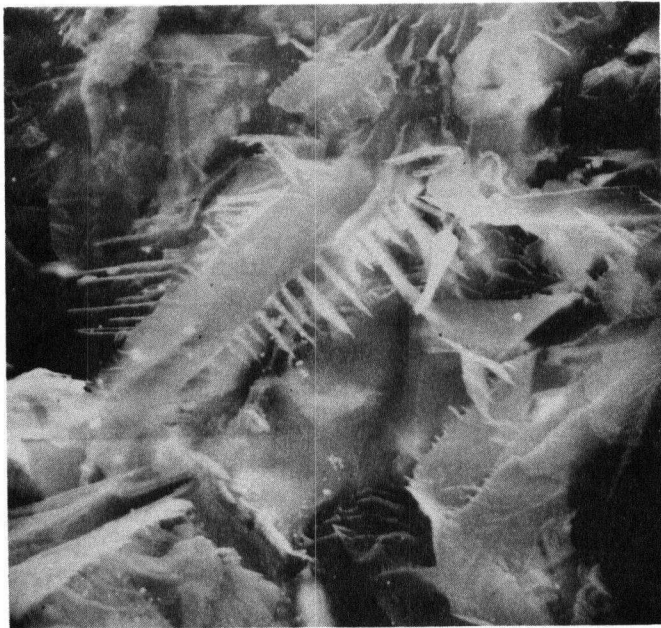
<u>Fig. 6.</u> Micrograph of corrosion product from fracture surface of type
310 stainless steel stress corroded in boiling MgCl$_2$ solution.
Stripped in bromine-methanol solution. (magnification 1200x)

carbon coated film was placed in the S.E.M. and an x-ray study made of the surface. Those regions which produced an x-ray spectrum were relocated in the T.E.M. and diffraction patterns taken. This analytical procedure for 304 and 316 corrosion products proved to be very tedious.

The corrosion product on the fracture surfaces of the 310 stainless steel was much thicker than that on 304 and 316, being easily stripped intact from the fracture surface. The stripped product was brittle and could easily be reduced to powder. Electron diffraction was difficult as heating and charging caused the corrosion product to break apart in the electron beam. X-ray spectroscopy of the stripped corrosion film in the S.E.M. required it to be held on the specimen grid with a carbon suspension paste (carbon dag). Heating and charging did not occur in the S.E.M. as the beam current was much lower than in the T.E.M.

3.2.2 Acetate Stripping

The acetate stripping technique was successful in removing the corrosion product from the surface of 310 specimens, but not too successful in the case of 304 and 316 specimens.

The stripped acetate picked up some corrosion product but also ripped out small segments of steel from the fracture surface. Direct x-ray analysis of the carbon coated acetate strip was not possible because of the difficulty in finding the product among the steel segments on the surface. In order for the stripped film to be analyzed, the carbon coated acetate film was dissolved in acetone. The carbon film with the corrosion product attached floated free and was examined in the T.E.M. and S.E.M. The acetate strip for the 304 and 316 fracture

surfaces had only small amounts of attached product. Thus, acetate

stripping was not a successful technique for removing corrosion films

from these surfaces. The acetate strip from the 310 fracture surface

had more patches of corrosion film which were easily analyzed in the

T.E.M. and S.E.M.

3.3 Electron Diffraction

The electron diffraction results are summarized in Table VI.

Electron diffraction patterns obtained from the stress corrosion

fracture surface corrosion product in situ and stripped, were similar

in all cases and could be fitted to a spinel oxide structure, M_3O_4.

The interplanar spacings (d) and x-ray intensities for Fe_3O_4, $FeCr_2O_4$

and γFe_2O_3 [23] are shown in Table VII. Sample patterns taken from

fracture surface oxides are shown in Fig. 7, with corresponding d-spacings

in Table VIII. Patterns of this quality were not the general rule,

the usual pattern being more diffuse (indicating small grain size).

Stripped corrosion products produced patterns which were clearer and

contained more lines than patterns obtained from corrosion products

in situ. In some cases, not all the diffraction pattern lines could be

fitted to the spinel. These lines were generally very faint and could

fit a rombohedral (corundum) type M_2O_3 oxide pattern, or a metal chloride

pattern. Diffraction patterns taken from the oxide in situ on 304 and

316 fracture surfaces sometimes contained extra lines produced by diffraction

of the underlying austenite due to the thinness of the oxide on these surfaces.

Examination of the stripped oxide films in transmission showed both

diffuse ring patterns and sharp ring patterns from both thick areas and thin
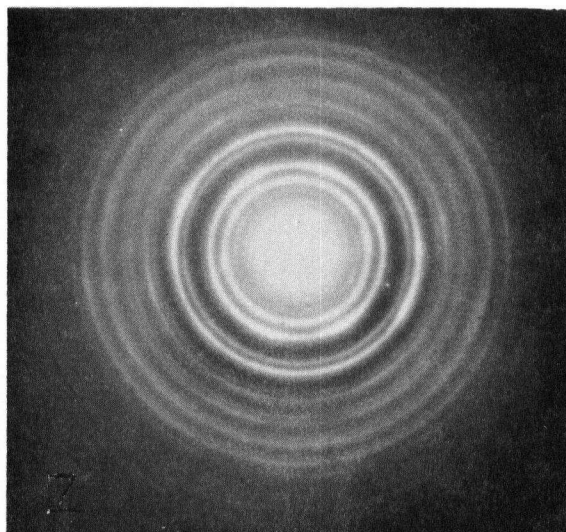
TABLE VI: Summary of Electron Diffraction Results

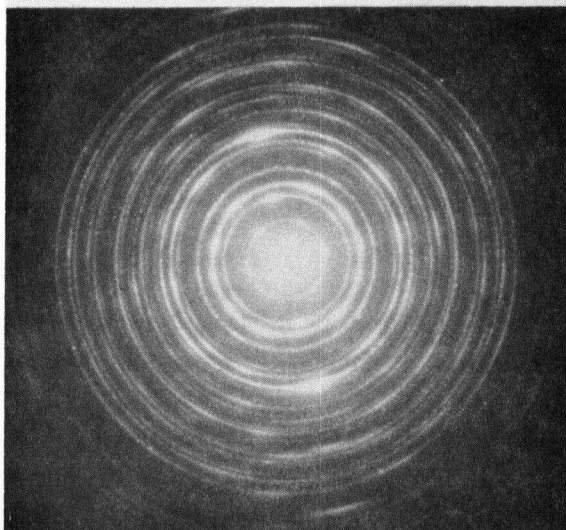| Alloy	Environment	Oxide	Structure
304	$MgCl_2$	s.c.c. fracture surface	M_3O_4
304	$MgCl_2+HCl$	s.c.c. fracture surface	M_3O_4
304	$MgCl_2+HCl$	exterior specimen surface	M_3O_4
304	$MgCl_2+CoCl_2$	s.c.c. fracture surface	M_3O_4
304	$MgCl_2+FeCl_3$	s.c.c. fracture surface	M_3O_4
304	$MgCl_2+FeCl_3$	exterior specimen surface	M_2O_3/M_3O_4
316	$MgCl_2$	s.c.c. fracture surface	M_3O_4
316	$MgCl_2+HCl$	s.c.c. fracture surface	M_3O_4
316	$MgCl_2+HCl$	exterior speciment surface	M_3O_4
316	$MgCl_2+CoCl_2$	s.c.c. fracture surface	M_3O_4
310	$MgCl_2$	s.c.c. fracture surface	M_3O_4
310	$MgCl_2+HCl$	s.c.c. fracture surface	M_3O_4
310	$MgCl_2+HCl$	exterior specimen surface	M_3O_4
310	$MgCl_2+CoCl_2$	s.c.c. fracture surface	M_3O_4

Table VII. d-Spacings and Relative Intensities for the Spinels of Iron, Fe_3O_4, γFe_2O_3, $FeCr_2O_4$, from ASTM X-ray Diffraction Cards

Fe_3O_4				$\gamma-Fe_2O_3$			$FeCr_2O_4$		
d A°	I/I$_1$	hkl	d A°	I/I$_1$	hkl	d A°	I/I$_1$	hkl
4.85	40	111	5.90	2	110	4.83	50	111
2.966	70	220	4.82	5	111	2.95	50	220
2.53	100	311	4.18	1	200	2.51	100	311
2.49	10	222	3.73	5	210	2.08	50	400
2.096	70	400	3.41	2	211	1.91	75	331
1.712	60	422	2.95	34	220	1.71	25	422
1.614	85	333/511	2.78	19	221	1.61	75	511/333
1.483	85	440	2.64	–	310	1.49	75	440
1.327	20	620	2.52	100	311	1.33	10	620
1.279	30	533	2.41	1	222	1.28	50	533
1.264	10	622	2.32	6	320	1.21	25	444
1.211	20	444	2.23	.5	321	1.17	10	711/551
1.1214	30	642	2.08	24	400	1.12	10	642
1.0922	60	553/731	1.87	.5	420	1.08	50	731
1.0489	40	800	1.70	12	422	1.05	25	800
0.989	10	660/822	1.61	33	511/333	0.965	50	751/555
0.962	40	555/751	1.55	.5	432/520	0.933	25	840
			1.53	1	521			
			1.48	53	440			
			1.43	1	433/530			
			1.32	7	620			
			1.27	11	533			
			1.26	3	622			
			1.21	5	444			
			1.12	7	642			
			1.09	19	553/731			
			1.07	1	650			
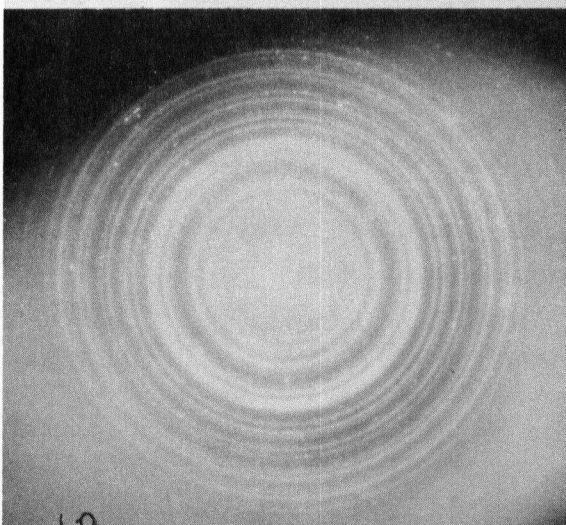
<u>Fig. 7.</u> **Sam**ple diffraction patterns from stripped stress corrosion fracture
surface oxides. a) 304, b) 316, C) 310

Table VIII. D, and d-Spacings of Diffraction Patterns Shown in Fig. 7

304 pattern #23462			316 pattern #23404			310 pattern #23418		
D in.	dA°	I/I$_o$	D in.	dA°	I/I$_o$	D in.	dA°	I/I$_o$
0.38	4.74	M	0.385	4.96	M	0.40	4.78	S
0.61	2.95	W-M	0.45	4.24*	VVW	0.53	3.60*	Dots
0.72	2.50	S	0.64	2.98	M	0.65	2.94	M
0.75	2.40	W	0.745	2.56	S	0.77	2.48	VS
0.81	2.22*	VVW	0.785	2.43	W	0.92	2.08	S
0.85	2..2	M	0.90	2.12	M	1.00	1.91	W
0.94	1.92	W	0.985	1.94	VVW	1.06	1.80*	Dots
1.06	1.70	W	1.02	1.88*	VVW	1.14	1.68	W
1.13	1.60	W-M	1.1	1.74	M-W	1.2	1.60	M
1.23	1.46	W-M	1.17	1.63	M	1.31	1.46	S
1.29	1.40	W	1.28	1.49	M	1.37	1.39	W
1.36	1.32	VVW	1.335	1.43	VW	1.46	1.30	VW
1.42	1.27	W	1.425	1.34	VW	1.51	1.26	W
1.49	1.21	W	1.48	1.29	W	1.6	1.2	M
1.54	1.17	VW	1.56	1.22	W	1.65	1.16	W

S- strong
M- medium
W- weak
VW- very weak
VVW- very, very weak
*- denotes a line which does not fit in the spinel (M_3O_4) pattern

D= diameter of diffraction ring on diffraction pattern
d= interplanar spacing

areas. Transformation of a diffuse ring pattern to a sharp ring pattern under the influence of the beam, as observed by Nielsen [14], was not observed in this study.

A comparison between the diffraction pattern from a chemically (bromine-methanol) stripped oxide and the diffraction pattern from a mechanically (acetate) stripped oxide is shown in Fig. 8, with corresponding d-spacings in Table IX. These patterns were similar. Chemical stripping did not alter the crystal structure of the corrosion product.

Diffraction patterns taken from oxides stripped from the exposed notch surface regions of specimens exposed to acidified $MgCl_2$ and $MgCl_2$ + $FeCl_3$ solutions are shown in Fig. 9. Two distinct patterns were observed on the oxides formed in $MgCl_2$ + $FeCl_3$. One pattern belongs to a spinel structure, the other fits a corundum M_2O_3 structure. This duplex structure was not observed on the fracture surface oxide formed in the same solution. The patterns taken from the exterior surface oxides formed in $MgCl_2$ + HCl solution were similar to patterns taken from the stress corrosion fracture surface oxides.

The lattice parameters of the oxides were determined to see if there was a variation between oxides. Francis [22] and Francombe[21] determined that the lattice parameter varied with composition for chromium, iron and nickel spinels. The determination of lattice parameters of cubic crystals can be made from a plot of D vs $(h^2 + k^2 + l^2)^{\frac{1}{2}}$ where D is the diameter of the ring on the electron diffraction pattern which corresponds to the lattice plane $\{hkl\}$. This is derived from the camera constant relation for analyzing diffraction patterns taken in a T.E.M., Dd = constant (K), where $d = a_o / (h^2 + k^2 + l^2)^{\frac{1}{2}}$ a_o is the lattice

a)
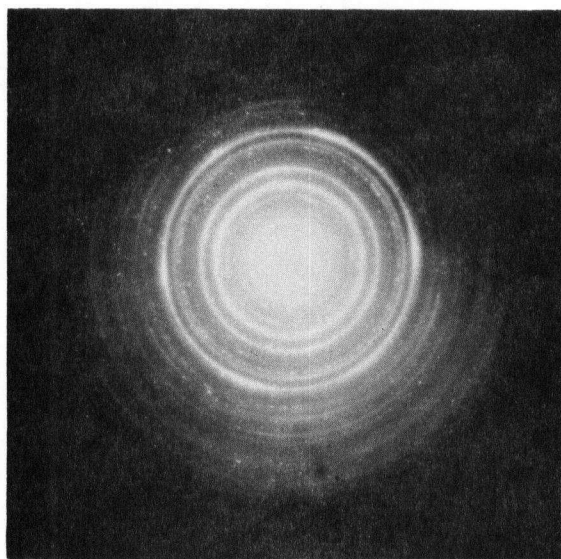
b)
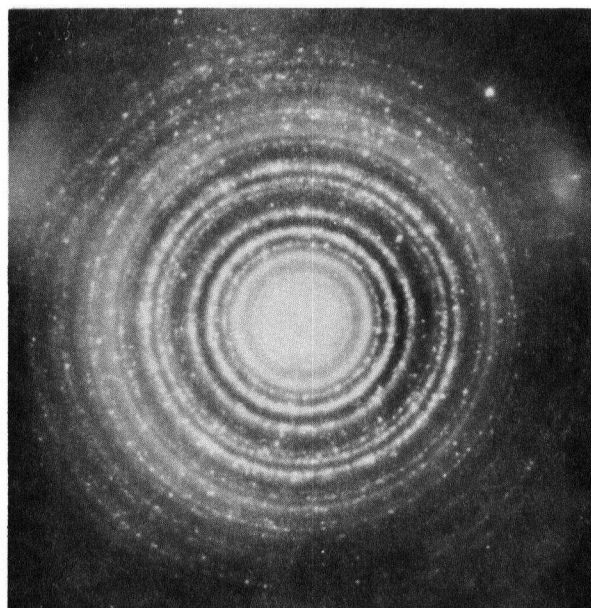
Fig. 8. Diffraction patterns taken from stress corrosion fracture
surface oxides of type 310 stress corroded in $MgCl_2$
a) bromine-methanol strip
b) cellulose acetate strip

Table IX. D, d-Spacings, and Relative Visual Intensities from Diffraction Patterns Taken from Bromine Strip and Acetate Strip Oxides (see Figure 8)

310 MgCl$_2$ - Bromine strip			310 MgCl$_2$ - Acetate Strip		
D in.	dA°	Intensity	D in.	dA°	Intensity
0.395	4.76	M	0.475	4.86	M
0.52	3.62*	VW	0.545	4.24*	Dots
0.64	2.94	W	0.63	3.67*	Dots
0.72	2.61*	VVW	0.78	2.96	M
0.75	2.51	S	0.905	S.55	S
0.86	2.19*	VVW	1.1	2.10	M
0.915	2.06	S	1.26	1.83*	Dots
0.98	1.92	VVW	1.34	1.72	W
1.04	1.81*	VVW	1.43	1.62	M
1.11	1.69	VW	1.56	1.48	M
1.18	1.59	W	1.62	1.43	Dots
1.275	1.47	M	1.74	1.33	Dots
1.325	1.42	VW	1.8	1.28	W
1.47	1.28	VW			
1.57	1.20	VW			

*- denotes a line that does not fit in the spinel M$_3$O$_4$ pattern
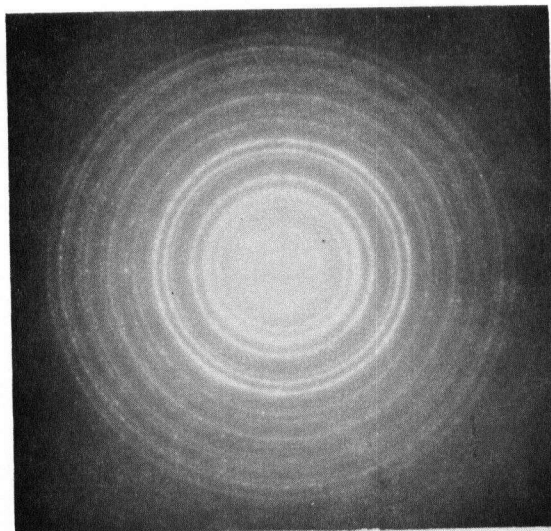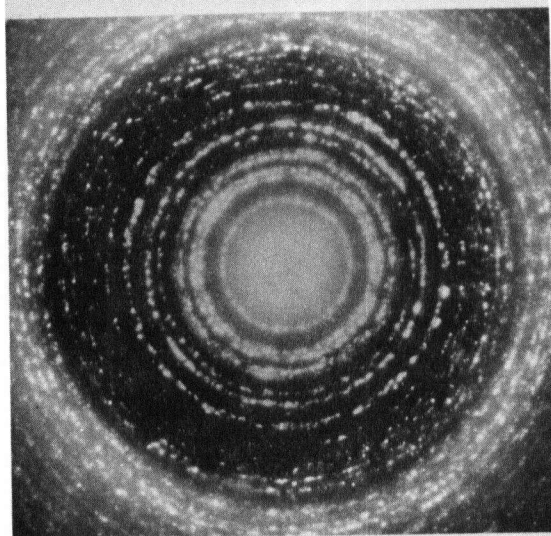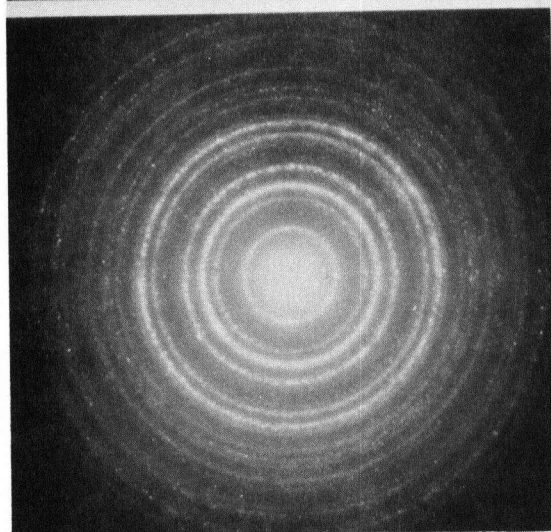
Fig. 9. Diffraction patterns taken from exposed notch areas of specimens
a) type 304 in $MgCl_2$ + $FeCl_3$. M_3O_4(spinel) pattern.
b) type 304 in $MgCl_2$ + $FeCl_3$. M_2O_3(rhombohedral) pattern
c) type 304 in $MgCl_2$ + HCl. M_3O_4(spinel) pattern

parameter, and d is the interplanar spacing. The constant K is obtained

by recording the diffraction pattern from a material of known d and

$\{hkl\}$ (usually gold) at the same instrument settings as the diffraction

pattern of the unknown specimen. Thus, the relation;

$$D = K/a_o \ (h^2 + k^2 + l^2)^{\frac{1}{2}} \tag{2}$$

Graphical plots of D vs $(h^2 + k^2 + l^2)^{\frac{1}{2}}$ for the different oxides are shown

in Appendix A. The excellent linearity of the plots provides overwhelming

evidence for the presence of a spinel crystal structure. The lattice

parameters determined from these plots are tabulated in Table X. They

vary inconsistently and are generally higher than the lattice parameters

determined by Francis [22] and Francombe[21]. This is probably due to the

presence of impurities and the inaccuracy of using electron diffraction patterns

to determine a_o values.

3.4 X-ray Spectroscopy

The x-ray spectroscopy results are summarized in Table XI.

3.4.1 X-ray Spectroscopy of Stripped Oxides

X-ray spectroscopy of stripped oxide films, showed the elemental

composition to be predominantly chromium and iron with lesser amounts

of nickel, silicon, molybdenum, magnesium, phosphorous, and chlorine.

The characteristic energy peaks of chlorine, phosphorous, molybdenum,

silicon and magnesium were inconsistent. They showed no correlation

between time to failure, alloy composition, environment, or between

samples from the same specimen. In some instances, a spectrum from a

sample of fracture surface oxide would have a large Si Kα peak. However,

a spectrum from another part of the same oxide would have a relatively

Table X. a_o Values Calculated from Plots of D vs $(h^2 + k^2 + l^2)^{\frac{1}{2}}$ in Appendix A, where Slope M = K/a_o, M Determined from Least Squares Analysis. All Oxides Stripped in 1% Bromine-Methanol Solution Except Where Noted

Alloy	a_o(A°) for oxides in various environments			
	$MgCl_2$	$MgCl_2$ + HCl	$MgCl_2$ + $CoCl_2$	$MgCl_2$ + $FeCl_3$
304	8.36	8.41	8.52	8.52
	8.41	8.45	8.52	8.44
	8.39	8.45	8.33	8.44
316	8.36	8.45	8.49	
	8.35	8.38	8.45	
	8.30	8.45	8.58	
310	8.36	8.27	8.45	
	8.36	8.23		
	8.41			
310	*8.38			
	*8.40			
	*8.44			

*- Oxide stripped with cellulose acetate

TABLE XI: Summary of Xray Spectroscopy Results   See Appendix B

Alloy	Environment	Oxide	Predominant Elements	CrKα/FeKα
304	$MgCl_2$	fracture surface	Cr,Fe,Ni,Cl,Mo,P,Si,Mg	>1
304	$MgCl_2$ + HCl	fracture surface	Cr,Fe,Ni,Cl,Mo,P,Si,Mg	>1
304	$MgCl_2$ + HCl	exterior notch surface	Cr,Fe,Ni,Cl,Mo,P,Si,Mg	>1
304	$MgCl_2$ + $CoCl_2$	fracture surface	Cr,Fe,Ni,Cl,Mo,P,Si,Mg	>1
304	$MgCl_2$ + $FeCl_3$	fracture surface	Cr,Fe,Ni,Cl,Mo,P,Si,Mg	variable
304	$MgCl_2$ + $FeCl_3$	exterior notch surface	Cr,Fe,Ni,Cl,Mo,P,Si,Mg	variable
316	$MgCl_2$	fracture surface	Cr,Fe,Ni,Cl,Mo,Si,P,Mg	>1
316	$MgCl_2$ + HCl	fracture surface	Cr,Fe,Ni,Cl,Mo,P,Si,Mg	>1
316	$MgCl_2$ + $CoCl_2$	fracture surface	Cr,Fe,Ni,Cl,Mo,P,Si,Mg	>1
310	$MgCl_2$	fracture surface	Cr,Fe,Ni,Cl,Mo,P,Si,Mg	>1
310	$MgCl_2$ + HCl	fracture surface	Cr,Fe,Ni,Cl,Mo,P,Si,Mg	>1
310	$MgCl_2$ + $CoCl_2$	fracture surface	Cr,Fe,Ni,Cl,Mo,P,Si,Mg	>1

minor SiKα peak. The intensity of these lower energy peaks was felt

to be dependent upon the success with which samples were washed to remove

traces of $MgCl_2$, and upon the random presence of magnesium oxychlorides

[17], as well as alloy inclusions (eg. sulphides and silicates) in the

oxide. Consequently, major deductions were obtained by confining attention

to the more consistent Fe, Cr, Ni peaks. Representative spectra taken from

the stripped oxide films formed in the various solutions are shown in

Appendix B. These spectra, as well as others appearing in the text are

normalized with respect to the chromium Kα peak. In general, the

same elements were present in the spectra taken from the different

alloys and environments although the peak heights vary. This variation

could be due to differences in composition, or it could result from

fluorescence and absorption occurring in the oxide. It is also possible

that scattering effects caused by the rough nature of the fracture

surface oxide caused the peak variations.

Chromium Kα was the strongest peak, usually followed by the iron

Kα. The spectra taken from the oxide formed on 304 and 316 specimens

in the various environments had integrated CrKα/FeKα ratios ranging from

1.5/1 to 6/1. Some of the spectra taken from these oxides could be

related to diffraction patterns, see Fig. 10, thus confirming the

assumption of thin corrosion films, and negligible absorption

and fluorescence effects. The spectra from the fracture surface

corrosion products of the 310 specimens had very high integrated CrKα/FeKα

ratios, as high as 10/1 in some cases. This was thought to be inconsistent

with a spinel structure. However, x-ray spectroscopy of chromite ore,

$FeCr_2O_4$, (see Fig. 11), gave similar results. Thus, the high integrated
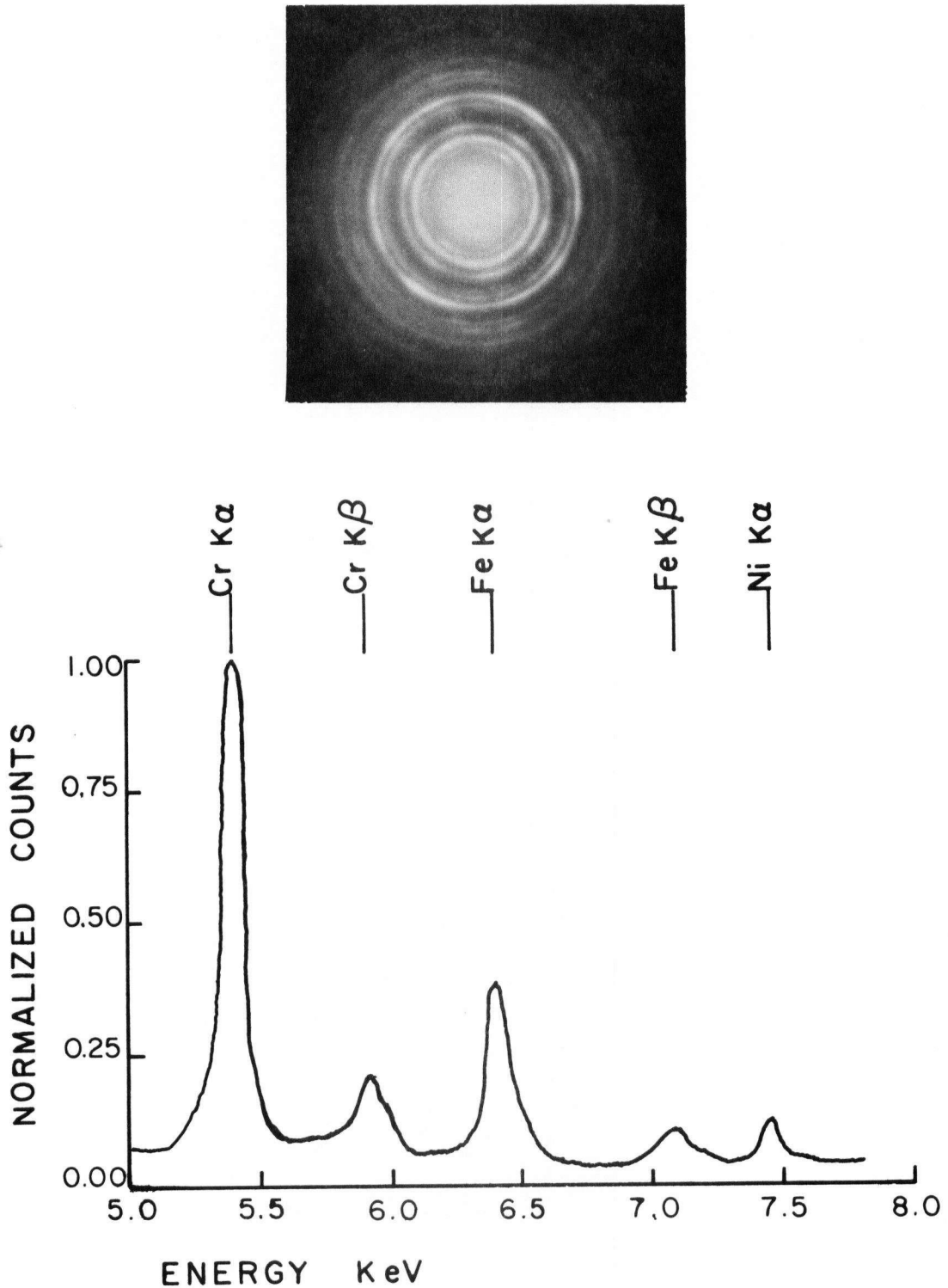
Fig. 10. Diffraction pattern and x-ray spectrum taken from the same area on a fracture surface oxide stripped from 316-type specimen stress corroded in $MgCl_2$ + $CoCl_2$ solution.
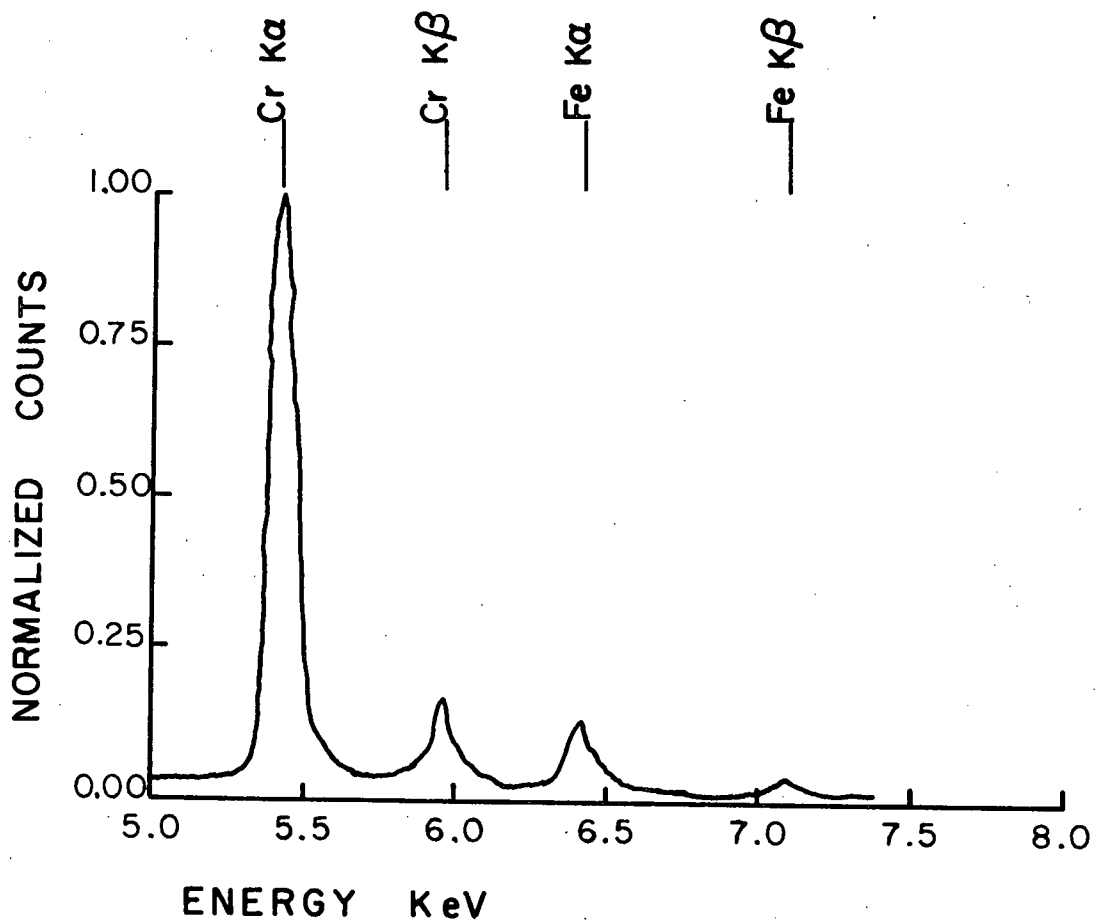
Fig. 11. X-ray spectrum taken from chromite ore.

CrKα/FeKα ratio was due to absorption and fluorescence effects in the oxide; the thin film assumption being invalid for the thick corrosion product on the 310 specimens.

X-ray spectroscopy of the corrosion product on the stress corrosion fracture surface of 304 cracked in the $MgCl_2$ + $FeCl_3$ solution showed the oxide had a variable composition. Spectra in Fig. 12 show the integrated CrKα/FeKα ratio changes from $\leqslant 1$ to $\geqslant 1$. Variations like this were not observed in any of the other oxides. Optical examination of the oxide showed that it had two distinct coloured layers; a silver gray colour on the metal/oxide interface, and a red brown colour on the oxide/ solution interface. Analysis of the red brown oxide always showed the integrated CrKα/FeKα ratio $\leqslant 1$ while analysis of the silver gray side always showed ratios $\geqslant 1$. Electron diffraction of this composite oxide produced a spinel pattern. This could indicate the composite oxide formed on the s.c.c. surface in the $MgCl_2$ + $FeCl_3$ solution is a spinel, chromium enriched at the metal interface and iron enriched at the solution interface. Iron and chromium spinels are miscible [22], thus there was probably no distinct boundary within the oxide. The oxide structure could remain the same while the composition varied from chromium enriched to iron enriched at the oxide solution interface.

The oxide that formed outside the crack on the specimen surface in the $MgCl_2$ + $FeCl_3$ solution had a similar x-ray spectrum as the oxide that formed in the crack. X-ray spectroscopy showed the oxide contained regions of varying integrated CrKα/FeKα ratios. Chromium rich regions existed as nodules of oxide while the iron enriched regions formed a layer. The two distinct colour layers observed on the stress corrosion crack

Fig. 12. X-ray spectra taken from the fracture surface oxide stripped from a type 304 specimen stress corroded in $MgCl_2$ + $FeCl_3$ solution. The three different spectra represent the variation in integrated $CrK\alpha/FeK\alpha$ ratio observed for this oxide.

     a) $CrK\alpha/FeK\alpha$ = 4.99/1
     b) $CrK\alpha/FeK\alpha$ = 1.01/1
     c) $CrK\alpha/FeK\alpha$ = 0.405/1

surface oxide were not observed on the oxide formed on the exterior surface of the specimen.

X-ray spectra of the oxide stripped from the outer notch surface of specimens exposed to acidified $MgCl_2$ solutions were similar to the spectra of the oxide formed on the s.c.c. fracture surfaces. No variation in peak ratios were observed and no surface irregularities were observed.

Spectra obtained from the mechanically and chemically stripped oxide formed on the 310 fracture surface are shown in Fig. 13. A characteristic peak at 1.48 eV in the chemically stripped spectrum was identified as a bromine $L\alpha$ peak. Thus during the stripping process bromine had become incorporated into the oxide. However, the major peaks were similar, with the exception of the relative heights (which could be due to fluorescence and absorption effects). Thus bromine-methanol stripping did not strongly alter the elemental composition of metal in the corrosion product.

The presence of chlorine peaks in all the x-ray spectra, after the oxide had been washed extensively, suggested that chloride ions could be part of the corrosion product and not a portion of solidified s.c.c. solution that had not been washed from the fracture surface. Oxychlorides may be present, however, Pourbaix [5] suggested that $FeCl_2 \cdot 4H_2O$ could be part of the corrosion product formed in s.c.c. cracks. X-ray diffraction charts for $FeCl_2$ show that its pattern would be masked to a certain extent by the spinel patterns, see Table XII. Thus, the detection of small quantities of metal chlorides by electron diffraction of the oxide would be difficult in this case. Hence it is possible that metal chlorides could be present in the corrosion product.
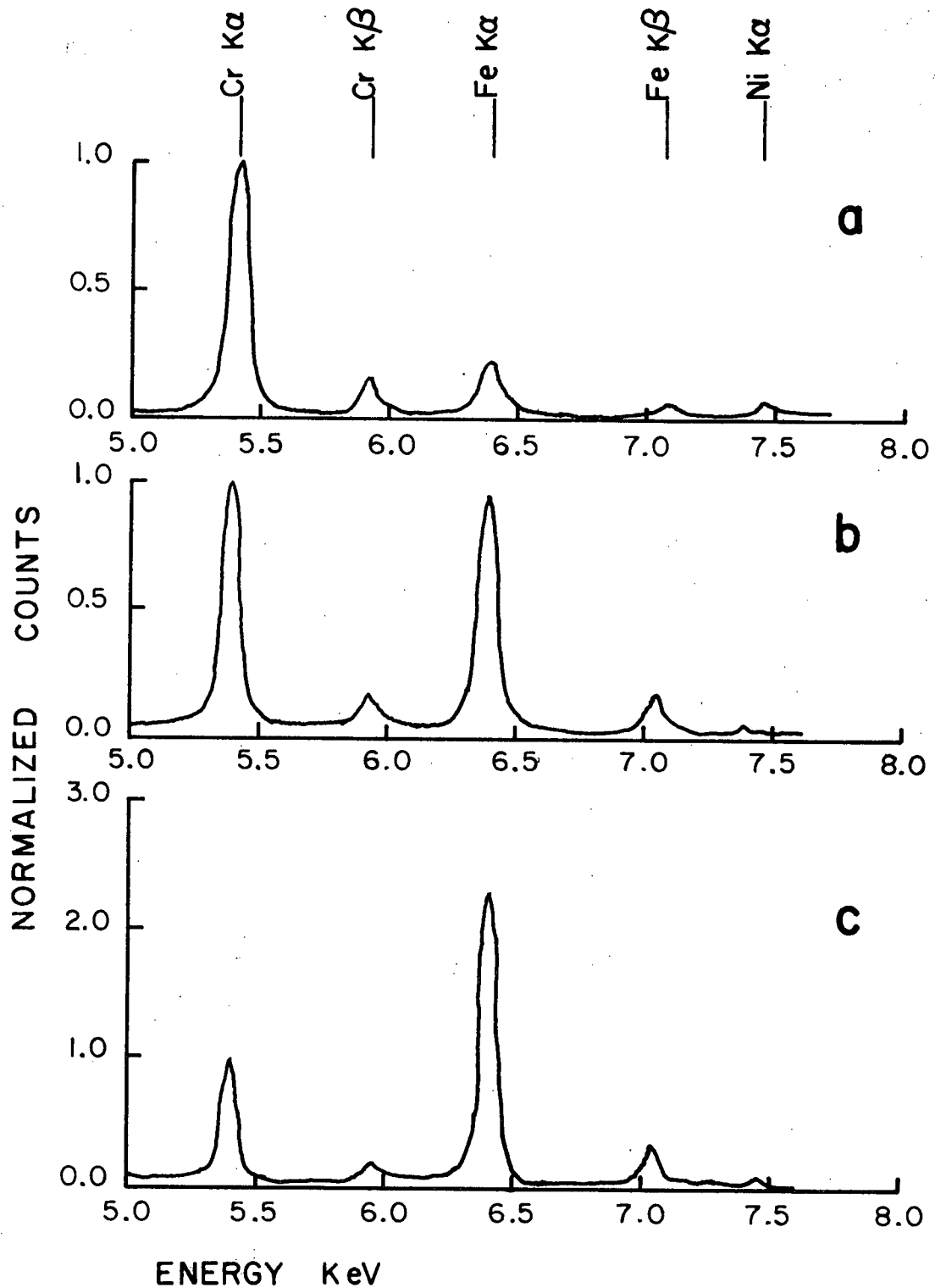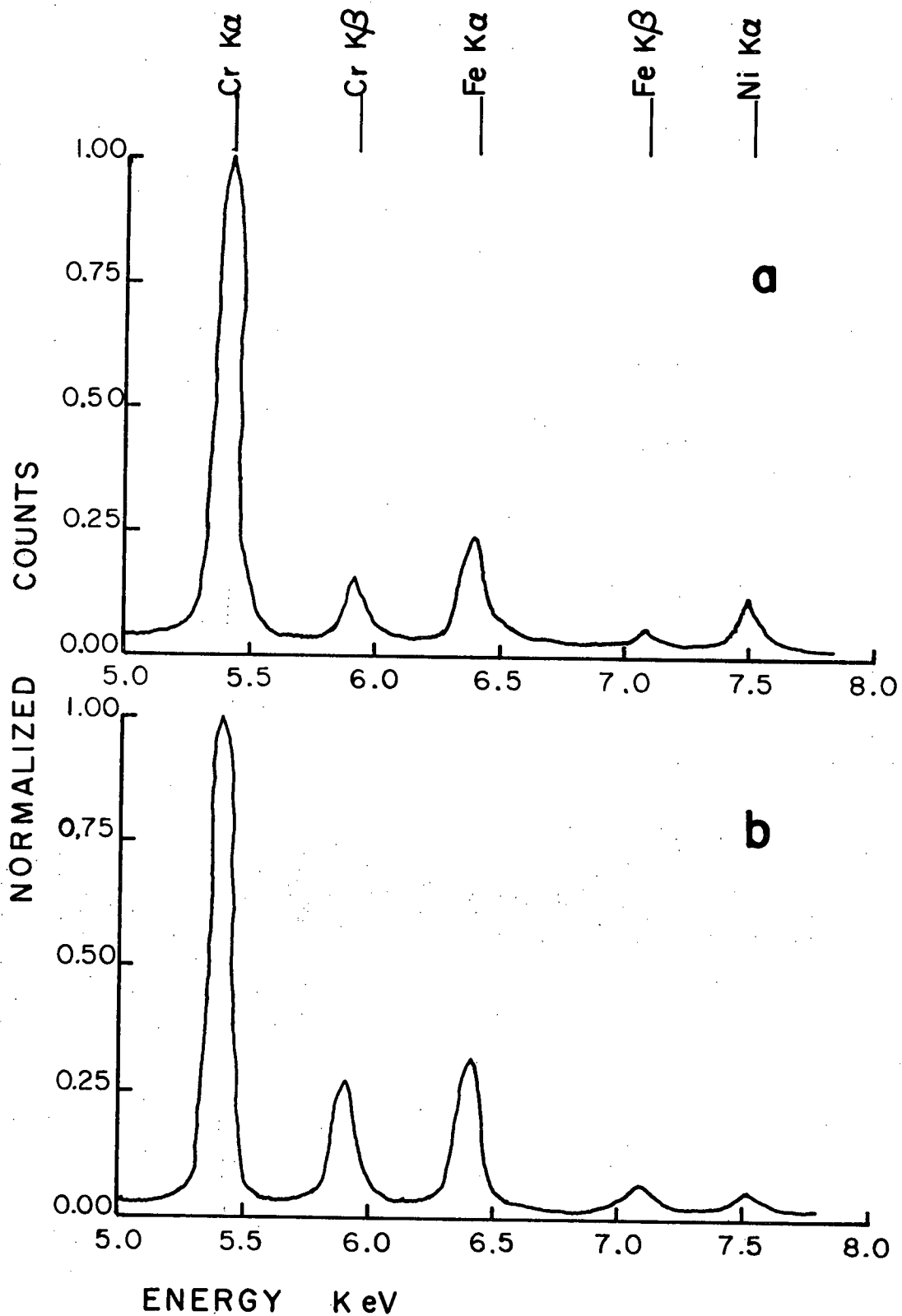
Fig. 13. X-ray spectra taken from fracture surface oxide stripped from a
type 310 specimen stress corroded in $MgCl_2$ solution.
a) oxide stripped with bromine-methanol solution
b) oxide stripped with cellulose acetate

TABLE XII: Xray Intensities and d-Spacings for Fe_3O_4 and $FeCl_2$ from ASTM Index Cards #11-614 and 1-1106 Respectively.

Fe_3O_4			$FeCl_2$		
dA°	I/I_1	hkl	dA°	I/I_1	hkl
4.85	40	111	5.9	63	003
2.966	70	220	3.07	30	101
2.530	100	311	2.54	100	104
2.419	10	222	2.32	7	015
2.096	70	400	2.09	7	N.I.
1.712	60	422	1.953	13	009
1.614	85	333/511	1.80	63	018
1.483	85	440	1.721	13	112
1.327	20	620	1.632	2	N.I.
1.279	30	533	1.552	4	021
1.264	10	622	1.467	20	0012/024
1.211	20	444	1.421	5	0111/205
1.1214	30	642	1.272	3	208
1.0922	60	553/731	1.173	2	0015/211
1.0489	40	800	1.138	18	1112/214

3.4.2 In Situ Spectroscopy

It was found that meaningful in situ x-ray spectroscopy of corrosion products was not possible unless the oxide was sufficiently thick that the volume of x-ray excitation was within the oxide and not the metal substrate. If the stress corrosion fracture surface was parallel to the electron beam (as in the high resolution diffraction stage of the T.E.M.), work by Bolon and Lifshin on scattering in thin films [28] indicates that the oxide should be about one micron thick for a significant amount of x-rays to be produced in the oxide.

X-ray spectra were taken in the high resolution diffraction stage of the T.E.M., from type 304, 316, and 310 stainless steels mechanical fracture surfaces, and compared to x-ray spectra taken from the stress corrosion fracture surfaces of type 304, 316, and 310 stainless steels (see Fig. 14). The spectra obtained from the s.c.c. surfaces of 304 and 316 were similar to the spectra obtained from the mechanical fracture surfaces. The corrosion product films on the 304 and 316 s.c.c. fracture surfaces were so thin that most of the x-rays came from the metal substrate. The corrosion products formed on the fracture surfaces of all type 310 specimens and type 304 in $MgCl_2$ + $FeCl_3$ solutions were sufficiently thick that most of the x-rays came from the oxide. Spectra taken from these fracture surfaces indicated the oxide was enriched in chromium and iron with nickel, silicon, molybdenum, and chlorine impurities, similar to the results from stripped oxide analysis.

In order to minimize the excitation of the metal substrate, stress corrosion fracture surfaces of 310 in $MgCl_2$ and 304 in $MgCl_2$ + $FeCl_3$ solutions were left in the bromine solution for 24 hours, dissolving the
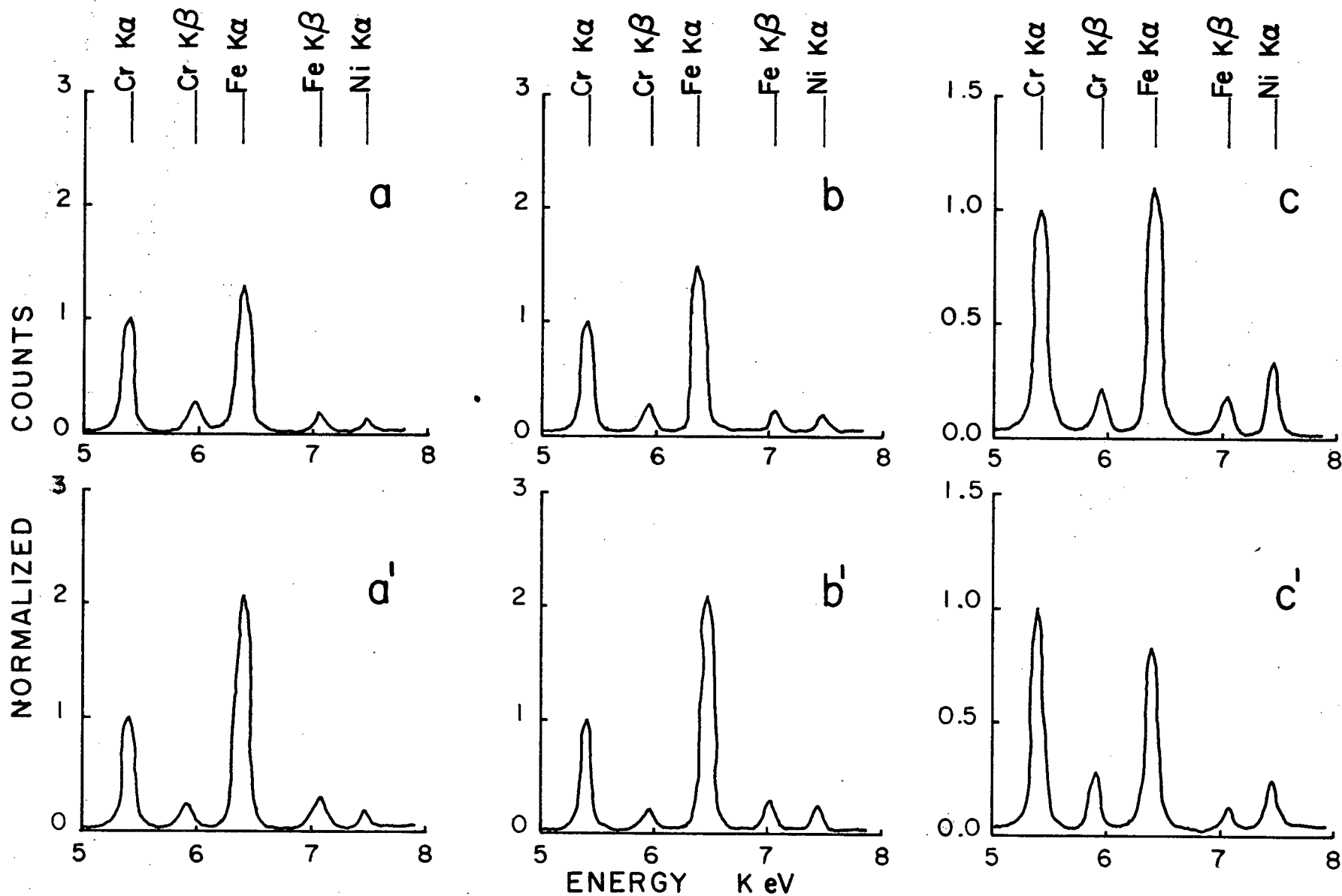
Fig. 14. Comparison of in situ x-ray spectra from mechanical fracture surfaces, with fracture surfaces from specimens s.c.c. in MgCl₂ solution.

a) type 304 mechanical fracture   b) type 316 mechanical fracture   c) type 310 mechanical fracture
a') type 304 s.c.c.   b') type 316 s.c.c.   c') type 310 s.c.c.

steel and leaving the surface oxide as a sponge on the surface. The
in situ spectra taken from the s.c.c. surfaces of the 304 specimen
in $MgCl_2$ + $FeCl_3$ solutions showed a variation in the integrated $CrK\alpha$/$FeK\alpha$
ratios from <1 to >1 as the oxide sponge was moved further into the
beam (see Fig. 15). This could indicate an oxide enriched in iron
at the surface, or the increasing chromium intensity could be due to
absorption and fluorescence effects occuring as the volume of oxide
exposed to the beam increases. However, x-ray spectra taken from the
corrosion product sponge on the 310 s.c.c. surface did not show this
variation in the $CrK\alpha$/$FeK\alpha$ ratio as the oxide was moved into the beam.
The integrated $CrK\alpha$/$FeK\alpha$ ratio was consistently greater than one.
Thus, the variation in the integrated $CrK\alpha$/$FeK\alpha$ ratio in the 304
specimen could be due to a concentration gradient in the oxide, as
observed in x-ray spectroscopy of this oxide stripped from the fracture
surface.

3.5 Partial Crack

Cooling a partially cracked specimen to room temperature caused
the whole solution which was trapped within the crack to form a hydrated
solid. This hydrate (predominantly hydrated $MgCl_2$ plus traces of metal
ions from the steel) will be referred to as the solidified crack solution.
Stripping this solidified solution from the crack was unsuccessful.
There was very little solidified solution on the specimen surface and,
also, it absorbed moisture from the air and flowed from the surface.

Observation of the partial crack surface in the S.E.M. showed
the solidified crack solution had collected in the bottom of fissures
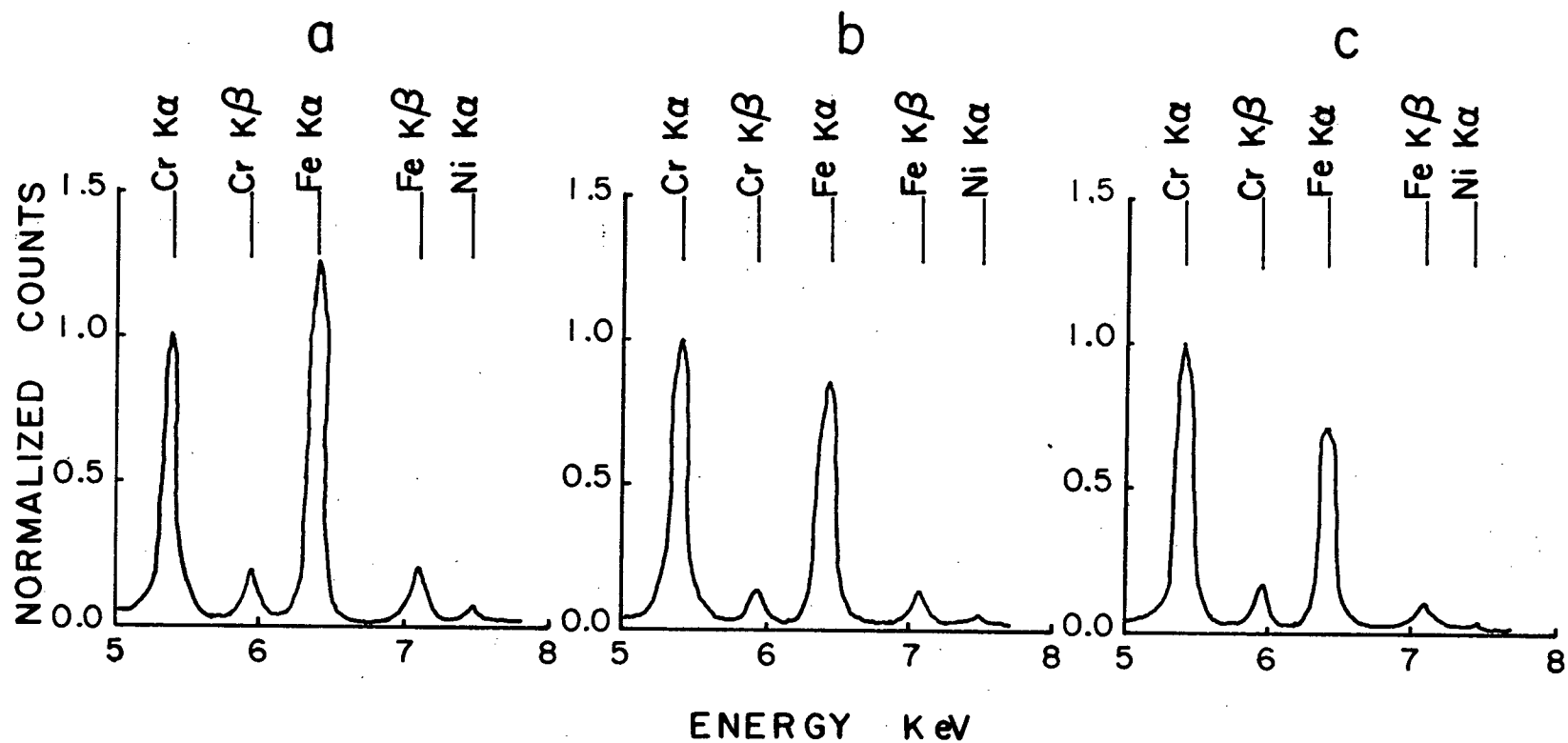
Fig. 15. In situ x-ray spectra taken from fracture surface oxide of type 304 specimen s.c.c. in a $MgCl_2$ + $FeCl_3$ solution. Shows variation in x-ray spectrum with beam penetration (as indicated by increasing x-ray count rate)
a) CrKα/FeKα = .764/1 (100 counts/sec)
b) CrKα/FeKα = 1.15/1 (300 counts/sec)
c) CrKα/FeKα = 1.40/1 (900 counts/sec)

on the surface (see Fig. 16). Direct x-ray spectroscopy of this solidified

solution showed large magnesium and chlorine peaks, together with small

peaks of chromium, iron and nickel in the same ratio as the underlying

metal. This was inconclusive as it was possible that the iron, chromium

and nickel peaks were caused by the underlying metal, and not from the

presence of these elements in the crack solution.

Using the techniques of qualitative aqueous inorganic chemical analysis,

it was possible to detect the presence of ferrous ions as opposed to ferric

ions in the solidified crack solution [29]. Partially cracked specimens

were taken from the stress corroding environment and immediately mechanically

fractured. A drop of potassium ferricyanide solution was placed on one

fracture surface and ammonium thiocyanate solution on the other.

Potassium ferricyanide turned the hydrate on the fracture surface deep

blue forming a precipitate, indicating the presence of ferrous ions in

the solidified crack solution. Ammonium thiocyanate should turn the

solidified crack solution deep red in the presence of ferric ions but

the only reaction was a faint pink color indicating that the ferrous

ion was the predominant ion within the crack environment.

During bromine-methanol stripping experiments on washed surfaces of

partially cracked specimens of 310, it was observed that the oxide removed

from the fracture surface was thinner than the oxide stripped from the

fracture surface of fully cracked specimens. Further evidence that

the oxide was thinner could be seen by comparing in situ x-ray spectra

Fig. 16. Solidified crack solution on fracture surface of type 304 specimen partially stress corroded in boiling $MgCl_2$ solution and mechanically fractured at room temperature (800x magnification)

from fully cracked type 310 specimens to those taken from partially

cracked type 310 specimens. It was observed that the height of the

CrKα, FeKα, and NiKα peaks obtained from the partially cracked surface

were of the same ratio as peaks obtained from mechanically fractured

specimens. Thus, the oxide was sufficiently thin that the majority

of the x-rays were coming from the metal substrate.

4. DISCUSSION

4.1 Diffraction Studies

Electron diffraction patterns from corrosion products, both in situ and stripped, were consistent with a spinel structure. This is in agreement with the observations and predictions of others [5,17,14]. On some diffraction patterns, faint lines not related to the spinel were observed and identified as possibly belonging to oxides of the type M_2O_3(either Cr_2O_3 or Fe_2O_3), or possibly to metal chlorides. Birley [17] observed extra lines in spinel patterns taken from corrosion products formed on the stress corrosion fracture surfaces of 304 and 310 stainless steels in boiling 154°C $MgCl_2$ solutions and boiling 125°C $MgCl_2$ + $FeCl_3$ solutions. He interpreted them as belonging to magnesium oxychlorides. However, the lines observed on Birley's diffraction patterns could also be associated with Cr_2O_3, or Fe_2O_3. Nielsen [14] also observed lines not associated with spinel patterns and concluded they belonged to a rhombohedral type oxide, M_2O_3(eg. Cr_2O_3, Fe_2O_3).

Diffraction patterns taken from oxides formed on the exterior surface of the 304 specimen in $MgCl_2$ + $FeCl_3$ solutions were different from patterns taken from the oxide on the stress corrosion fracture surface. The oxide on the exterior surface produced two distinct patterns, one belonging to a corundum type oxide M_2O_3, and the other belonging to a spinel. This is in contrast to the observations of Baker et al. [15] who observed only a spinel oxide pattern on the exterior surface. In contrast, the s.c.c. fracture surface oxide in this study had a spinel type structure in which no distinct M_2O_3 type oxide pattern was observed. This suggests there was a difference

between the crack environment and the bulk solution environment, resulting in two different oxides.

Nielsen [14] observed transformations in corrosion products isolated from stress corrosion cracks and speculated they were caused by hydrated oxides losing water under the influence of the beam. Transformation of iron hydroxides in the electron beam has been observed by others, the end result being a spinel [30,31]. No transformations were observed in the oxides during this study, but it is not possible to say they did not occur while the specimen was in the evacuated microscope column. It was felt, however, that hydroxides would not be stable in s.c.c. environments of such low pH as reported for boiling $MgCl_2$ solutions. Sato et al. [32] studied passive films on iron in solutions of various pH and concluded that in acid environments of pH ≤5 the oxide on the surface was an anhydrous spinel. Thus, there is some doubt as to whether a hydrated oxide exists in the crack environment. Transformations were observed in the present study during diffraction analysis of reagent grade $FeCl_2 \cdot 4H_2O$. Pourbaix [5] suggested that metal chlorides could exist as a stable phase in the stress corrosion crack environment and this was supported by the presence of chlorine peaks in the x-ray spectra taken from the stress corrosion fracture surface corrosion products. The dehydration of a hydrated metal chloride could be the transformation observed by Nielsen [14]; the $FeCl_2$ pattern being similar to an Fe_3O_4 pattern (Table XII). Nielsen isolated corrosion products from stress corrosion cracks by dissolving the surrounding metal and washing the oxide in methanol. In our study, the corrosion products were taken from the fracture surface after it

had been washed in hot water. It is likely that the corrosion products

isolated from cracks would contain more metal chlorides and trapped

solidified solution than products stripped from washed fracture surfaces.

Therefore, it is more probable that a dehydration of a hydrated metal

chloride would be observed in Nielsen's [14] study than in the present

study. Since Nielsen conducted no analysis for elements other than nickel,

iron, chromium, and molybdenum, the possibility that the corrosion product

isolated from cracks contained some metal chlorides dispersed in the

spinel oxide cannot be ruled out.

4.2   X-ray Analysis

X-ray spectroscopy, although qualitative, was consistent. It

indicated a chromium enriched Fe-Cr oxide onthe stress corrosion fracture

surface in all cases except the $MgCl_2$ + $FeCl_3$ solution. Diffraction and

x-ray analysis of similar areas on stripped corrosion products showed

the oxide was primarily a chromite spinel ($FeCr_2O_4$) with impurities of

nickel, silicon, molybdenum, magnesium, phosphorous, and chlorine. The

presence of impurities suggests that the oxide is defective and is not

a stoichiometric $FeCr_2O_4$ spinel. These results were in general agreement

with Nielsen's [14] work on 316 stainless steel in $MgCl_2$ solutions and

Marek and Hochman's [18] observations on type 316 single crystals in

$MgCl_2$ solutions.

The addition of CoCl$_2$ and HCl to the basic $MgCl_2$ solution had

no effect on the structure or composition of the stress corrosion

fracture surface oxide. Smith et al. [9] in studies on 4340 steel in

$MgCl_2$ solutions observed that the pH inside the crack did not vary,

being constantly pH 3.5-3.9, while the bulk solution was varied from pH 2-10. Similarly Baker et al. [15] observed the crack solution to have a constant pH 1.2-2.5 in 304 stainless steel. These observations suggest that the crack pH is controlled by conditions within the crack. Hence, acid additions to the bulk solution would not be expected to affect the crack environment or oxide. The absence of any effect by $CoCl_2$ is not surprising considering the selectivity of s.c.c. environments. Although at room temperature Co^{+2} has a higher reduction potential than Fe^{+3}, the thermodynamics of this ion could be quite different in a deoxygenated, high chloride concentration, low pH solution.

Addition of $FeCl_3$ to the basic $MgCl_2$ solution decreased the time to failure (see Table V) and produced a layered spinel oxide with a composition gradient. The nature of the composition gradient suggests a spinel approaching an Fe_3O_4 composition at the solution interface and a spinel approaching an $FeCr_2O_4$ composition at the metal interface. The composition gradient could be explained by assuming that the environment was the same at the crack tip for both $MgCl_2$ solutions and $MgCl_2$ + $FeCl_3$ solutions. In both cases, the only iron ions entering solution during electrochemical dissolution at the propagating crack tip are ferrous ions Fe^{+2}, and the corrosion product approached an $FeCr_2O_4$ spinel. However, in the situation with $MgCl_2$ + $FeCl_3$ solutions, ferric ions migrating from the bulk solution are able to participate in cathodic reactions occurring on the crack walls remote from the crack tip. The reduction of ferric ions to ferrous ions, will yield a solution containing both Fe^{+3} and Fe^{+2}. Hydrolysis reactions in

such solutions could yield spinels approaching an Fe_3O_4 composition which deposit on the pre-existing $FeCr_2O_4$. eg;

$$\text{reduction} \quad Fe^{+3} + e^- \rightleftharpoons Fe^{+2} \tag{3}$$

$$\text{hydrolysis} \quad 2Fe^{+3} + Fe^{+2} + 4H_2O \rightleftharpoons Fe_3O_4 + 8H^+ \tag{4}$$
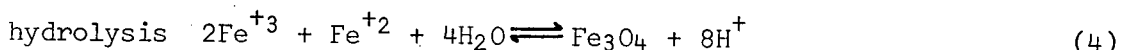
Furthermore, the reduction of ferric ions in the $MgCl_2$ + $FeCl_3$ solution should yield a higher corrosion potential and corrosion current than in the $MgCl_2$ solution. The higher corrosion current would lead to increased dissolution rates at the crack tip, and a corresponding reduced time to failure, as observed.

4.3 Potential -pH Equilibria Within the S.C.C. Crack

Potential -pH diagrams for the austenitic stainless steels in boiling chloride environments do not exist. Therefore, it is not possible to predict the stable phases in these environments. However, E -pH diagrams for iron, chromium, and nickel in water at 150°C are available [31,33], as are diagrams for chromium in water + 0.1 M Cl⁻ at 25°C, and for $Fe-FeCl_2-H_2O$ system at 25°C [5,34] (see Fig. 17-20, where E is measured with reference to the standard hydrogen electrode,S.H.E.).These diagrams are no substitute for stainless steel-$MgCl_2$ diagrams, but they do provide useful information. The pH inside cracks has been reported to vary between pH 1 at the tip and pH 4.5 in the bulk of the crack [16,15,9,36]. Newburg and Uhlig [35] measured critical applied potentials below which no stress corrosion was observed for austenitic stainless steels in boiling 154°C $MgCl_2$ solutions, -0.128V (S.H.E.) for 304 and -0.103V (S.H.E.) for 310 (these are applied potentials, not crack tip potentials). Comparing this data with the E -pH diagrams shows that the crack environment is in the active area for all three alloys. Under these conditions only a
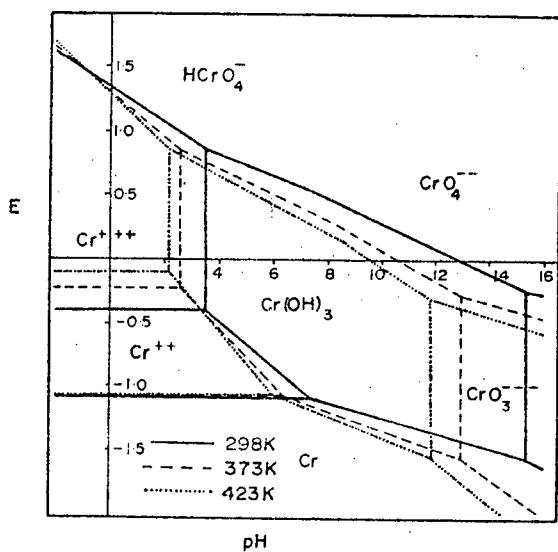
Fig. 17. Potential -pH (E-pH) diagram for the Cr-H_2O system. Concentration of soluble species 10^{-6}M., from Brook [33].
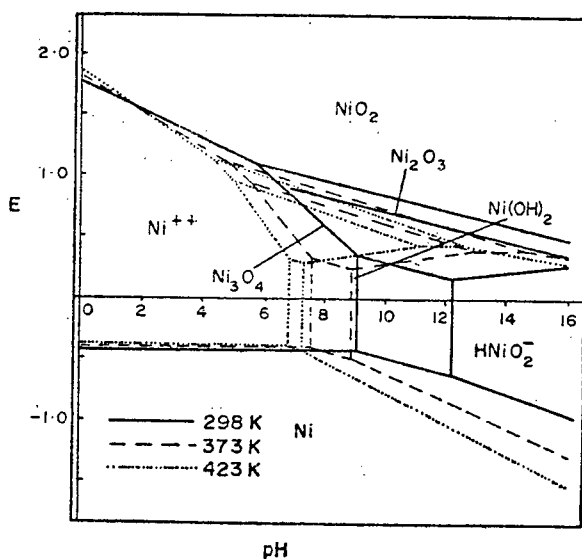
Fig. 18. Potential -pH (E-pH) diagram for the Ni-H_2O system. Concentration of soluble species 10^{-6}M., from Brook [33].
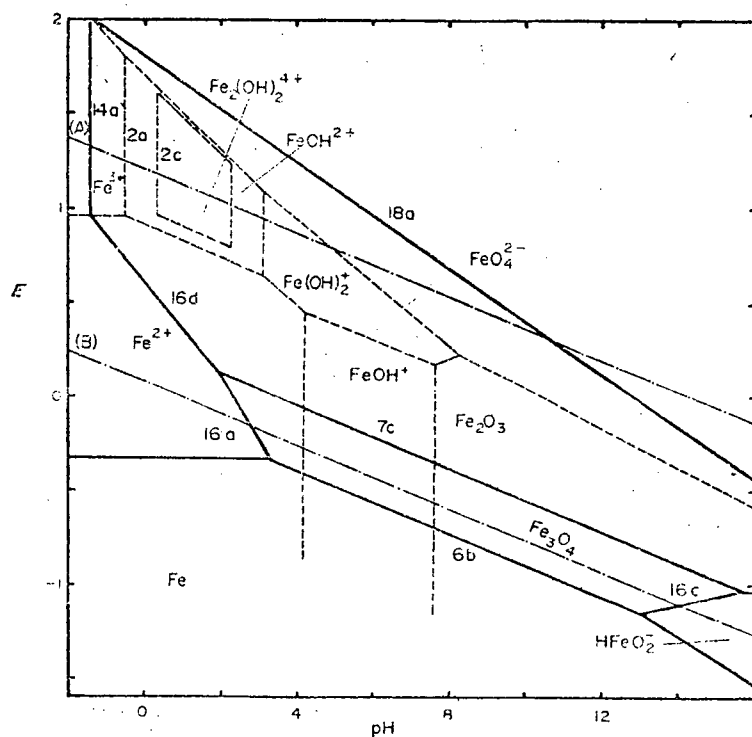
Fig. 19. Potential -pH (E-pH) diagram for the Fe-H₂0 system at 150°C.
Unit activity of soluble species, from Biernat and Robins [31].
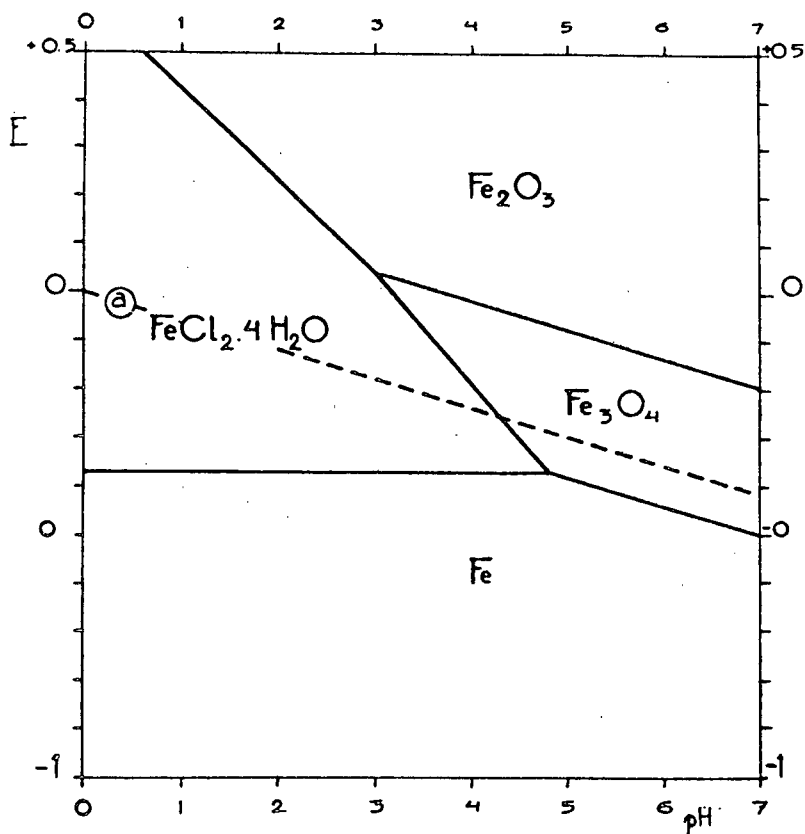
Fig. 20. Calculated areas of stability of Fe, FeCl₂·4H₂0, and Fe₃0₄ in the
presence of a solution electroneutral in FeCl₂, (schematic) from
Pourbaix [5].

chromium hydroxide (oxide) is stable. Consequently, $FeCr_2O_4$

would probably be stable in this environment.

These E -pH diagrams indicate the crack solution will contain

Fe^{+2}, Ni^{+2}, Cr^{+3}, and Cr^{+2} ions. Ferrous ions were detected in the

solidified crack solution trapped on the fracture surface of partially

cracked specimens. No tests for nickel or chromium ions were

performed in this study, however, Wilde [20] has performed controlled

potential corrosion tests of 304 austenitic stainless steels in boiling

$MgCl_2$ solutions and determined the metal ions in solution. His work

showed that the solution enriched in iron compared to the steel

composition and was depleted in chromium, which he assumed made up

the bulk of the corrosion product oxide. The Cr^{+3}/Cr^{+2} ratios

at -0.103V and -0.128V (S.H.E.) obtained from Fig. 17 by using

the Nernst equation [$E = E_o + \dfrac{RT}{nF} 2.303 \log (aCr^{+3}/aCr^{+2})$]

are .949 and .494, indicating a significant fraction of Cr^{+2} ions

present. It is possible that these chromous ions could react

with chloride ions to form $CrCl_2$, as well as $FeCr_2O_4$. The fate of the

nickel appears to be unresolved. Staehle [7] reports that the nickel

is preferentially dissolved from the alloy surface, but Wilde [20] reported

that nickel dissolved uniformly, neither enriching the alloy surface

nor depleting it. The E -pH diagram of Fig. 17 for pure nickel in

water indicates that the activity of Ni^{+2} ions at the aforementioned

potentials should be quite low. However, the effect of the presence

of other ions (eg. Cr^{+2}, Fe^{+2}, Cl^-) at high concentrations on the ionic

activity of Ni^{+2} is unknown.

Wilde [20] and Staehle's [7] work, on austenitic stainless steels

in chloride solutions has been performed in the bulk solutions on the bulk specimen surface. Studies of surface properties in bulk solutions may be significant for crack initiation, but care must be used when applying these results to crack propagation. The crack tip solution is very different from the bulk solution as is evidenced by pH studies in stress corrosion cracks, and the variation in oxides formed on exterior surfaces and fracture surfaces in $MgCl_2$ + $FeCl_3$ solutions.

4.4 Growth of Oxide Films

It was observed that the oxide on the stress corrosion fracture surface of type 310 specimens was uniformly thicker than the oxide on the stress corrosion fracture surface of 304 and 316 specimens. However, fully cracked specimens of 304 left in the boiling $MgCl_2$ solution for 40 hours did not have a noticeably thicker film than specimens removed immediately upon fracture. Also, specimens of 304 and 310 mechanically fractured in the presence of boiling 154°C $MgCl_2$ and left for one hour in the solution had a similar fracture surface appearance. Thus 310 does not inherently form a thicker oxide in the bulk solution. Observations of oxide stripped from fracture surfaces of partially cracked specimens of 310 indicated that the oxide thickened with time in the stress corrosion crack. Similarly, oxides isolated by Nielsen [14], and Marek and Hochman [18], in boiling $MgCl_2$ solutions were thicker than oxides in this study. This suggests dynamic conditions inside the crack cause the 310 oxide to thicken.

The oxide could grow by general dissolution of the underlying metal through a porous oxide with resulting oxide formation. However,

it is not likely that the oxide thickened by underlying metal dissolution
because the cracked sample of 304 left in solution for 40 hours did not
thicken. Also, anodic dissolution of the crack walls would not be
anticipated as this would lead to crack blunting and absence of s.c.c.

Assume the crack walls are cathodic to an anodic crack tip, then it
is possible for hydrogen ions to be reduced on the crack walls, providing
the oxide is conductive. Chromite is not a good conductor. However,
the fracture surface oxide was not totally chromite, but contained
other elements which may modify the conductivity. Since ferrous ions
and very limited concentrations of ferric ions are present within the
crack solution, it is possible for some Fe_3O_4 to be present in the oxide.
The presence of small amounts of both Fe^{+3} and Fe^{+2} will result in a
significant increase in conductivity [37]. Furthermore, it is possible for
the crack oxide to be porous. If metal chlorides, form at the crack
tip [5], and then dissolve after the crack has propagated, the oxide
could contain pores, which allow hydrogen ions to be reduced on the
metal interface. The hydrogen ions could arise from the hydrolysis
of metal ions produced by dissolution at the crack tip; eg.

$$Fe^{+2} + 2Cr^{+3} + 4H_2O \rightleftharpoons FeCr_2O_4 + 8H^+ \tag{5}$$
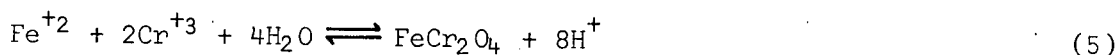
Equation (5) is consistent with both the present observations of
chromium enriched spinels and the observation of others of low pH
within the crack. Consequently, reduction of hydrogen ions on the
crack walls would displace equation (5) to the right and cause further
growth of the spinel film. Specimens of 310 take approximately 40 hours
to break in boiling 154° C $MgCl_2$ solutions, while specimens of 304
and 316 take approximately 2-4 hours. If a process similar to the above
occurs, it suggests that the corrosion products would be thicker in the s.c.c.
cracks in 310 specimens as observed.

4.5 Envisioned Events within the Stress Corrosion Crack

The results of this study were consistent with an electrochemical mechanism of s.c.c., whereby the crack advanced by anodic dissolution of the crack tip followed by precipitation of the corrosion products on the walls of the crack. Precipitation of the corrosion products prevented lateral attack of the crack walls and localized dissolution to the crack tip.

Hydrolysis of anodically dissolved metal ions (see equation 5) gave rise to the observed spinel corrosion product and increased the hydrogen ion concentration within the crack. Reduction of the hydrogen ions on the crack walls provided the cathodic reaction necessary for maintenance of anodic dissolution. Thus there was an autocatalytic reaction within the crack. [The role of stress could be confined to the rupture of any corrosion product (film) which tends to block the crack tip and prevent exposure to the environment].

The envisioned process requires the corrosion product to be electrically conducting, as it has to function as the cathode for the anodic crack tip. It could be conductive either because it is a non-stoichiometric spinel, or because porosity in the film exposes the underlying metal.

Porosity could arise from conjoint precipitation of metal chlorides and spinels, followed by dissolution of the metal chlorides after the crack tip had advanced. The possibility that metal chlorides are formed at the crack tip has been proposed by Beck [38]. Working with titanium alloys, Beck proposed that an oxide could not form fast enough to explain the current time behaviour he observed, whereas a metal chloride could. The formation of a spinel unit cell requires 56 atoms. Thus, a unit cell

of $FeCr_2O_4$ would require 8 ferrous and 16 chromic ions in their solvation
sheaths to come together, react and form the oxide. Meanwhile, the metal
ions are surrounded by a high concentration of chloride ions. Therefore,
it is possible that formation of metal chlorides and/or hydrated metal
chlorides may have more favourable reaction kinetics than oxide formation.

4.6 Effect of Alloy Composition

There was no evidence to support a consistent variation in corrosion
product composition with variation in alloy composition. Consequently,
the corrosion product film was not the only factor in stress corrosion
cracking. The effects of alloy composition on electrochemical kinetics,
crack path, dislocation structure, and stacking fault energy were equally
important, as is evident by the different fracture paths. Certainly
the effect of nickel on the stress corrosion cracking behaviour has yet
to be satisfactorily explained. Nickel-free, iron and chromium ferritic
stainless steels are resistant to s.c.c. in hot aqueous chloride environments.
Additions of a few percent nickel renders austenitic stainless steels,
very susceptible to s.c.c. Additions of nickel greater than 20 wt %
results in resistance to s.c.c. again [4]. Crystal structure alone cannot
explain the variation, as ferritic stainless steels will stress corrode [36].

Shibata and Takeyama [40] and Staehle [7] studied the effect of nickel
content on the dissolution kinetics of iron chromium alloys in boiling
$MgCl_2$ solutions. Shibata and Takeyama found the maximum dissolution
current density, I_{max}, observed during straining electrode experiments,
decreased with increasing nickel content. Staehle [7] observed that
the activation energy for dissolution increased as the nickel content

increased, leading to a decrease in dissolution current. Shibata

and Takeyama also found that the current density decay dI/dT is more

rapid for 304 than 310. They interpreted this as meaning 304 had a

higher film formation (repassivation) rate than 310. If 304 does

repassivate faster it means there could be more general corrosion at the

crack tip in 310 alloys, thereby blunting the crack and lowering the

stress intensity at the crack tip.

An alternative and important effect of the nickel composition

may be through its effect on the reversible electrode potential,

E_o, of the bare alloy surface. Nickel has been noted to raise both

the critical potential for s.c.c. and the corrosion potential [13,35].

A higher corrosion potential, E_{corr}, could lead to a reduced corrosion

current, I_{corr}, and a reduced rate of metal dissolution at the anodically

propagating crack tip. This is most easily visualized with respect

to an Evans diagram [41], as shown in Fig. 21.
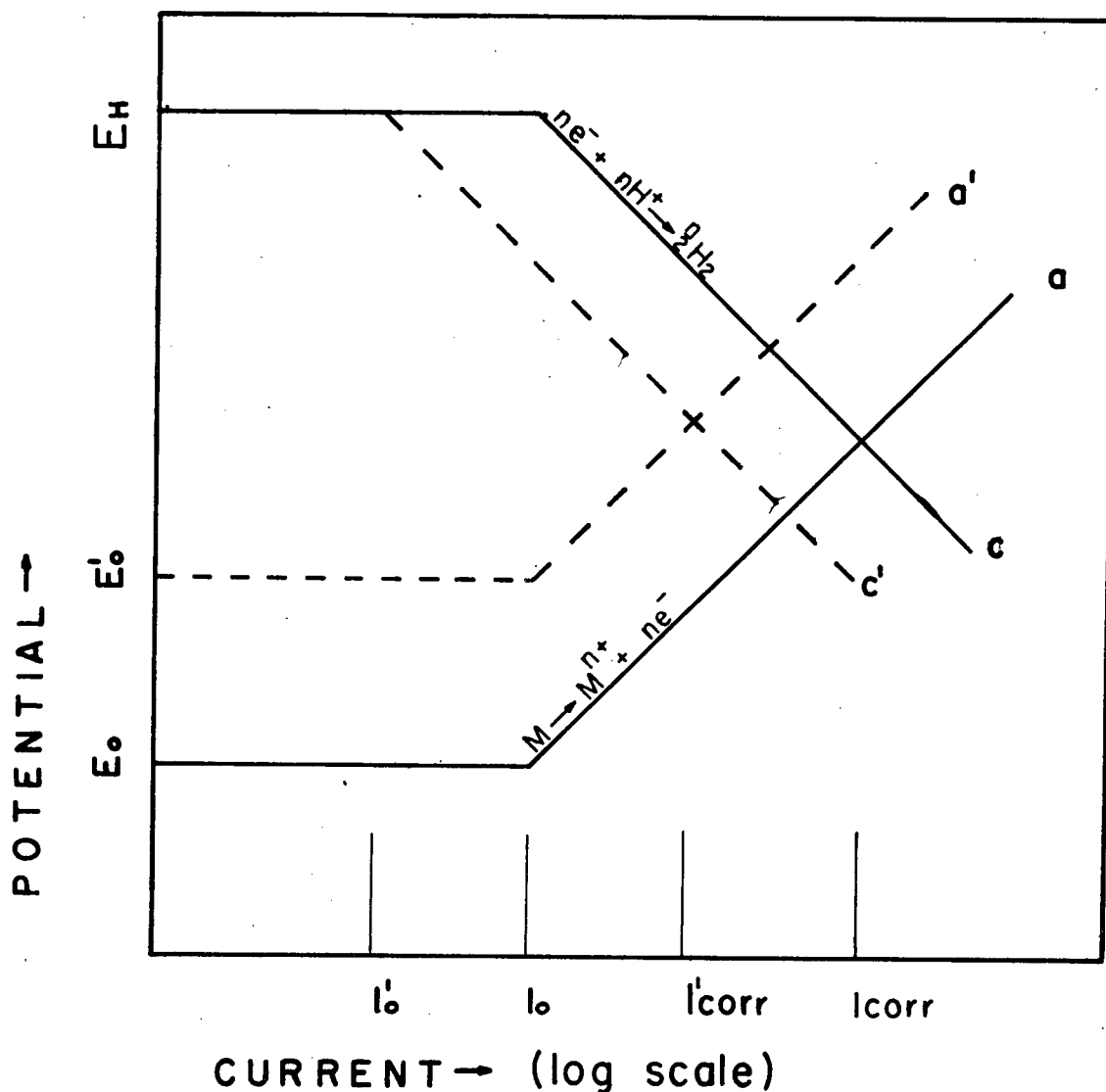
Fig. 21. Schematic Evans diagram showing possible effects of alloying on electrochemical behaviour. Base alloy has electrochemical behaviour depicted by curves a and c. Upon alloying with nickel, the alloy reversible potential increases from E_o to E_o', resulting in a lower corrosion current I_{corr} to I'_{corr}. Alloying may lower the exchange current density for hydrogen reduction from I_o to I'_o, again, lowering I_{corr} to I'_{corr} [39].

5.   CONCLUSIONS

Electron diffraction and qualitative x-ray analysis of corrosion products formed in stress corrosion cracks of the austenitic stainless steels 304, 316, and 310 tested in boiling aqueous $MgCl_2$ solutions led to the following conclusions;

1) The corrosion product on the stress corrosion fracture surface of the different alloys was similar, being a chromium enriched spinel oxide containing lesser amounts of the elements iron, nickel, molybdenum, silicon, phosphorous, magnesium, and chlorine.

2) There was a significant difference between the oxide (and environment) on the exterior specimen notch surface, and the oxide (and environment) in the stress corrosion crack.

3) The presence of spinel oxide was consistent with the observations of others on the pH and electrochemical potential (E) of stress corrosion cracks in austenitic stainless steels. These results indicate the crack environment was in the low pH "active triangle" region of the E-pH diagrams for the alloys.

4) The variation in s.c.c. behaviour between the different alloys could not be adequately accounted for in terms of the composition of the oxide.

BIBLIOGRAPHY

1. ENGELL, H.J. Theory of Stress Corrosion Cracking in Alloys, P. 86, Nato Scientific Affairs Division (1971).

2. STAEHLE, R.W. Fundamental Aspects of Stress Corrosion Cracking, P. 3, Proccedings of Conference, published by National Association of Corrosion Engineers (1969).

3. NIELSEN, N.A. Corrosion, Vol. 27, #5, P. 173 (1971).

4. STAEHLE, R.W. Fundamental Aspects of Stress Corrosion Cracking, P. 214, Proceedings of Conference, published by National Association of Corrosion Engineers (1969).

5. POURBAIX, M. Theory of Stress Corrosion Cracking in Alloys, P. 17, Nato Scientific Affairs Division (1971).

6. BOND, A.P. and DUNDAS, H.J. Corrosion, Vol. 24, #10, P. 344 (1968).

7. STAEHLE, R.W. Theory of Stress Corrosion Cracking in Alloys, P. 223, Nato Scientific Affairs Division (1971).

8. McCARTHY, H.A. and HARRISON, P.L. Corrosion Science, Vol. 14, P. 469 (1974).

9. SMITH, J.A.; PETERSON, M.H. and BROWN, B.F. Corrosion, Vol. 26, #12, P. 539 (1970).

10. RHODES, P.R. Corrosion, Vol. 25, #11, P. 462 (1969).

11. BROWN, B.F.; FUJII, C.T. and DAHLBERG, E.P. J. Electrochem. Soc., Vol. 116, #2, P. 218 (1969).

12. BIRLEY, S.S. and TROMANS, D. Corrosion, Vol. 27, #2, P. 63 (1971).

13. LEE, H.H. and UHLIG, H.H. J. Electrochem. Soc., Vol. 117, #1, P. 18 (1970).

14. NIELSEN, N.A. Physical Metallurgy of Stress Corrosion Cracking, Metallurgical Society Conferences, Vol. 4, Interscience Publishers, New York, N.Y. (1959).

15. BAKER, H.R.; BLOOM, M.C.: BOLSTER, R.N. and SINGLETERRY, C.R.
         Corrosion, Vol. 26, #10, P. 420 (1970).

16. MAREK, M. and HOCHMAN, R.F. Corrosion, Vol. 26, #1, P. 5 (1970).

17. BIRLEY, S.S. Ph.D. Thesis, University of British Columbia,
         Vancouver, Canada (1972).

18. MAREK, M. and HOCHMAN, R.F. Corrosion, Vol. 27, #9, P. 361 (1971)

19. DAVIS, J.A. and WILDE, B.E. J. Electrochem. Soc., Vol. 117, #11
         P. 1348 (1970).

20. WILDE, B.E. J. Electrochem. Soc., Vol. 118, #11, P. 1717 (1971)

21. FRANCOMBE, M.H. J. Phys. Chem. Solids, Vol. 3, P. 37 (1957).

22. FRANCIS, J.M. J. Appl. Chem., Vol. 16, Sept., P. 264 (1966).

23. NAKAYAMA, T. and OSHIDA, Y. Corrosion, Vol. 24, #10, P. 336 (1966).

24. LATIMER, W.M. The oxidation states of the elements and their potentials
         in aqueous solutions, 2nd ed., Prentice Hall, New York (1952).

25. JACOBS, M.H. and BABOROVSKA Proc. Fifth European Congress on
         Electron Microscopy (1972).

26. KUBASCHEWSKI and HOPKINS Oxidation of Metals and Alloys, 2nd ed.,
         Butterworth and Co. Ltd. (1962).

27. ASTM STANDARDS, X-ray diffraction cards #11-614, 4-0755, 4-0759.

28. BOLON, R.B. and LIFSHIN, E. Scanning Electron Microscopy, P. 285,
         Proceedings of the 6th annual Scanning Electron Microscopy
         Symposium, IIT Research Institute, Chicago, Illinois (1973).

29. VOGEL, A.J. Macro and Semicro Qualitative Inorganic Analysis,
         fourth edition, Longmans, Green and Co. Ltd., London

30. FEDORCHENKI, I.M. and TRUSHKO, P.V.   Doklady Akademii Nauk S.S.S.R.,
         Vol. 211, #4, P. 905 (1973).

31. BIERNAT, R.J. and ROBINS, R.G. Electrochimica Acta, Vol. 17,

     P. 1261 (1972).

32. SATO, N.; NODA, T. and KUDO, K. Electrochimica Acta, Vol. 19,

     P. 471 (1974).

33. BROOK, P.A. Corrosion Science, Vol. 12, P. 307 (1972).

34. POURBAIX, M. Atlas of Electrochemical Equilibria in Aqueous

     Solutions, Pergamon Press (1966).

35. NEWBURG, R.T. and UHLIG, H.H. J. Electrochem. Soc., Vol. 120,

     #12, P. 1629 (1973).

36. BROWN, B.F. Theory of Stress Corrosion Cracking in Alloys,

     P. 186, Nato Scientific Affairs Difision (1971).

37. STANDLEY, K.J. Oxide Magnetic Materials, Oxford University Press

     (1962).

38. BECK, T.R. Corrosion, Vol. 30, #11, P. 408 (1974).

39. KRUGER, J. Fundamental Aspects of Stress Corrosion Cracking,

     P. 296, Proceedings of Conference, Published by National

     Association of Corrosion Engineers (1969).

40. SHIBATA, T. and TAKEYAMA, T. Boshoku Gijutsu, 23, P. 379 (1974).

41. EVANS, V.R. The Corrosion and Oxidation of Metals: Scientific

     Principles and Practical Applications, Edward Arnold Ltd.

     London (1960).

APPENDIX A

This appendix contains the data summarized by Tables VI and X.

Analysis of representative diffraction patterns from the various fracture

surface oxides are presented as are graphical plots of D vs $(h^2 + k^2 + l^2)^{\frac{1}{2}}$

(from which the lattice parameters in Table X were determined). The

diffraction patterns are all taken from stripped corrosion product

films by conventional means in the transmission electron microscope.

The symbols used in this appencix are as follows;

hkl - Miller indices of crystal lattice planes

K   - camera constant (see page 38) units of ins·A$^{\circ}$

D   - diameter of the electron diffraction ring on the diffraction

       pattern, units of inches

d   - the interplanar spacing corresponding to plane $\{hkl\}$ which

       rive rise to diffraction ring D. units of Angstroms

I_v - relative visual intensity of diffraction ring

M   - slope of D vs $(h^2 + k^2 + l^2)^{\frac{1}{2}}$ determined by least squares fit

a_o - lattice parameter of cubit crystal as obtained from plots

       of D vs $(h^2 + k^2 + l^2)^{\frac{1}{2}}$ where a_o = K/M

Table A1. 304 S.C.C. in $MgCl_2$, Oxide Stripped with 1% Bromine-Methanol
Solution
pattern #22217   camera constant K = 1.88 ins·A°

line	D in.	dA°	I_v	$FeCr_2O_4$ (hkl)	$\sqrt{h^2 + k^2 + l^2}$
1	0.39	4.82	W	111	1.73
2	0.63	2.98	W	220	2.83
3	0.74	2.54	S	311	3.32
4	0.77	2.44	VVW	222	3.46
5	0.835	2.25	VW	-	-
6	0.90	2.09	S	400	4.0
7	0.98	1.92	VVW	331	4.36
8	1.05	1.79	VVW	-	-
9	1.115	1.68	VVW	422	4.9
10	1.16	1.62	M	333/511	5.2
11	1.275	1.47	S	440	5.66
12	1.33	1.41	VVW	531	5.92
13	1.385	1.36	Dots	620	6.32
14	1.47	1.28	VW	533	6.56
15	1.555	1.21	W	444	6.93
16	1.59	1.18	Dots	551/711	7.14

Data plotted in Fig. A1, D vs $(h^2 + k^2 + l^2)^{\frac{1}{2}}$

Slope $M = \dfrac{K}{a_o} = 0.225$ in

$a_o = \dfrac{1.88}{0.225}$ A°

Lattice parameter $a_o = 8.36$A°
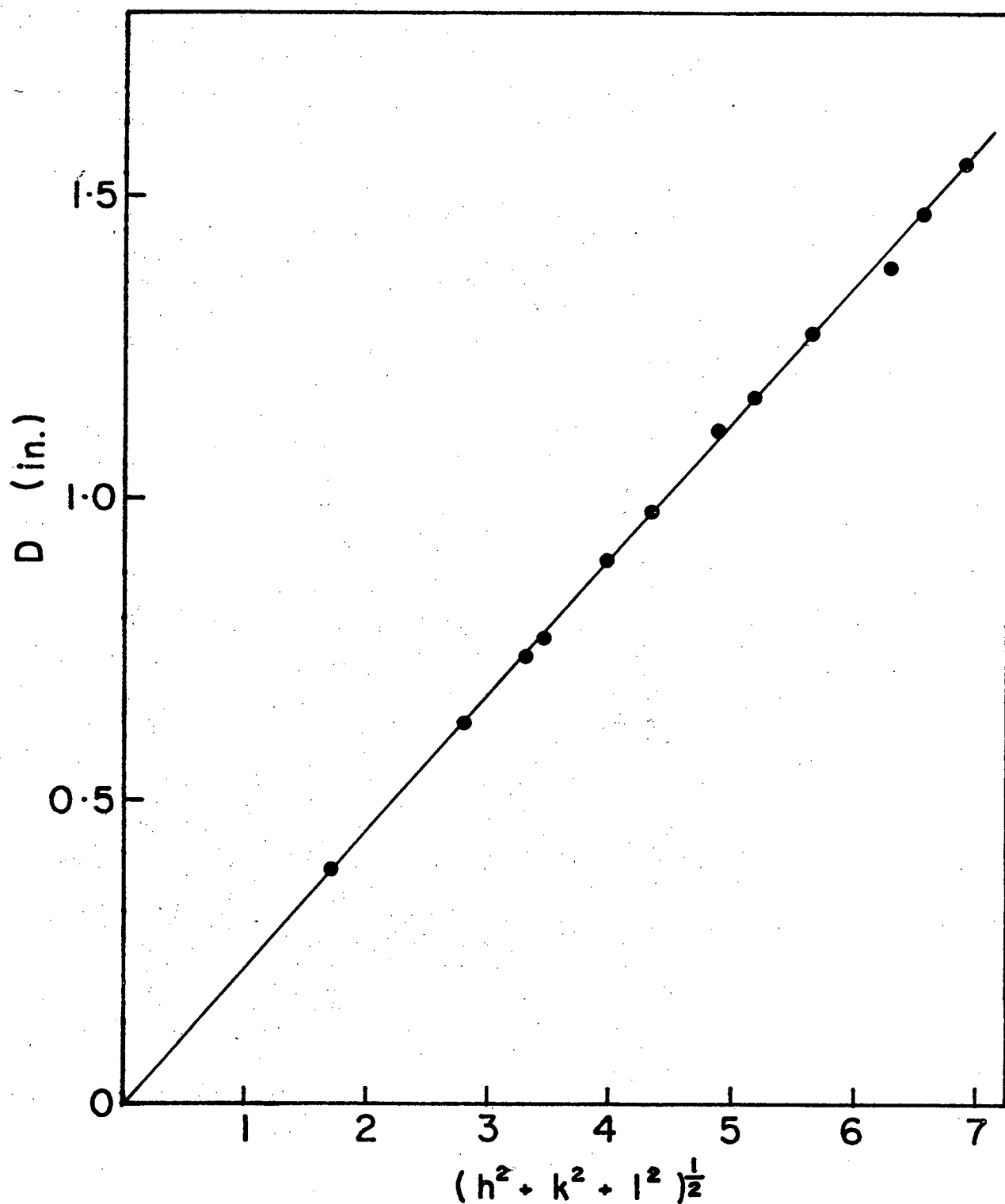
Fig. A1. Plot of D vs $(h^2 + k^2 + l^2)^{\frac{1}{2}}$ from Table A1. Diffraction pattern #22217, 304 s.c.c. in $MgCl_2$, oxide stripped with 1% bromine-methanol solution

<u>Table A2.</u> 304 S.C.C. in $MgCl_2$, Oxide Stripped with 1% Bromine-Methanol
Solution
pattern #23299   camera constant K = 1.95 ins·A°

line	D in.	dA°	I_v	$FeCr_2O_4$ (hkl)	$\sqrt{h^2 + k^2 + l^2}$
1	0.79	2.47		311	3.32
2	0.82	2.38		222	3.46
3	0.93	2.10		400	4.0
4	1.32	1.48		440	5.66
5	1.53	1.27		533	6.56
6	1.61	1.21		444	6.93
7	1.86	1.05		800	8.00
8	2.00	0.975		555/751	8.66
9	2.10	0.93		840	8.94

Data plotted in Fig. A2, D vs $(h^2 + k^2 + l^2)^{\frac{1}{2}}$

Slope $M = \dfrac{K}{a_o}$ = 0.232 in

$a_o = \dfrac{1.95}{0.232}$ A°

Lattice parameter a_o = 8.41A°
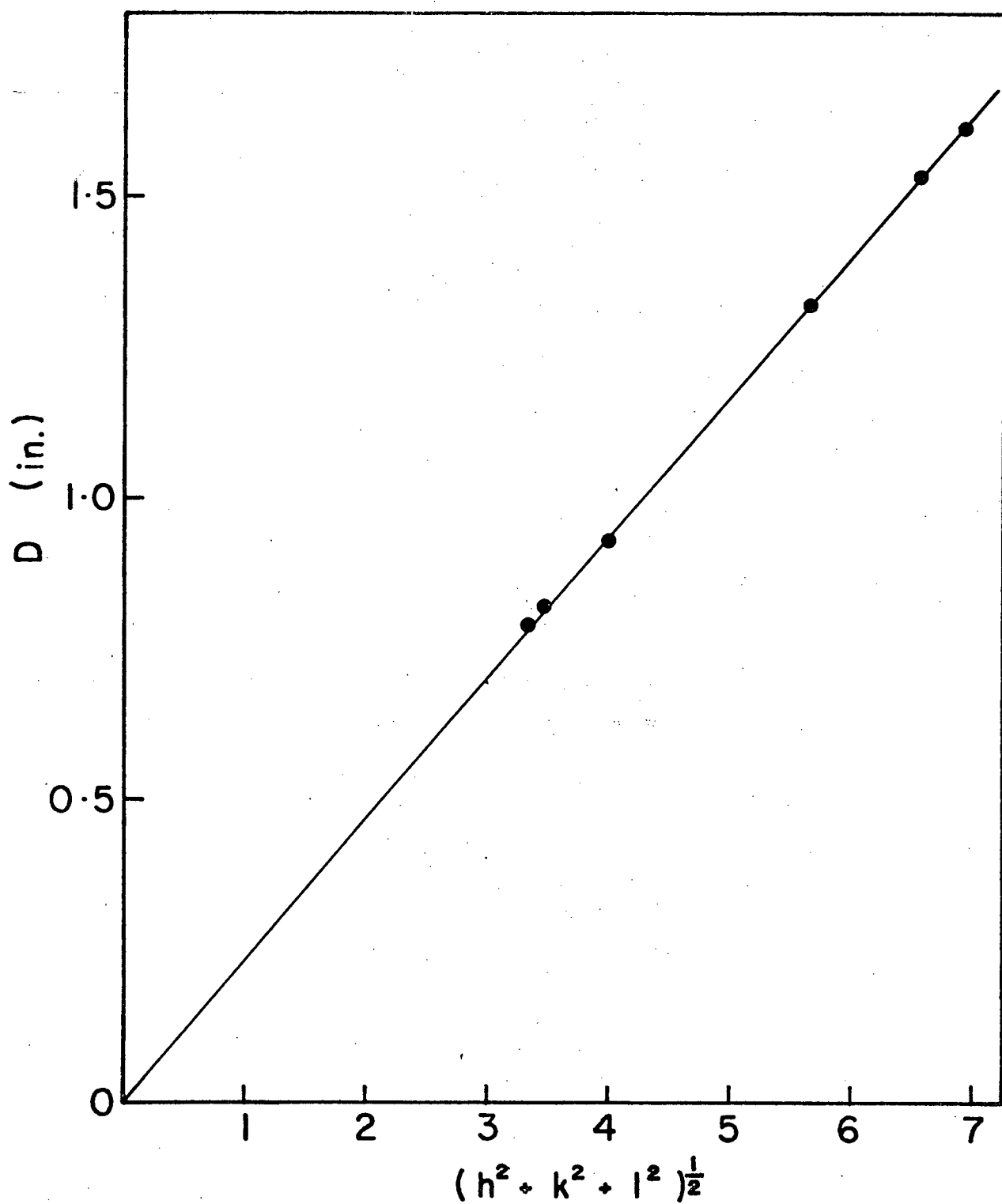
<u>Fig. A2.</u> Plot of D vs $(h^2 + k^2 + l^2)^{\frac{1}{2}}$ from Table A2. Diffraction
pattern #23299, 304 s.c.c. in $MgCl_2$, oxide stripped with 1%
bromine-methanol solution.

Table A3. 304 S.C.C. in $MgCl_2$, Oxide Stripped with 1% Bromine-Methanol Solution
pattern #23389   camera constant K = 1.88 ins·A°

line	D in.	dA°	I_v	$FeCr_2O_4$ (hkl)	$\sqrt{h^2 + k^2 + l^2}$
1	0.39	4.90	W	111	1.73
2	0.63	3.03	M	220	2.83
3	0.75	2.55	S	311	3.32
4	0.90	2.12	M	400	4.0
5	1.05	1.82	VVW	-	-
6	1.1	1.74	VVW	422	4.9
7	1.17	1.63	W	511/333	5.2
8	1.28	1.49	M	440	5.66
9	1.47	1.30	W	533	6.56
10	1.55	1.23	W	444	6.93
11	1.72	1.11	W	553/731	7.68
12	1.80	1.06	W	800	8.0

Data plotted in Fig. A3, D vs $(h^2 + k^2 + l^2)^{\frac{1}{2}}$

Slope $M = \dfrac{K}{a_o} = 0.224$ in

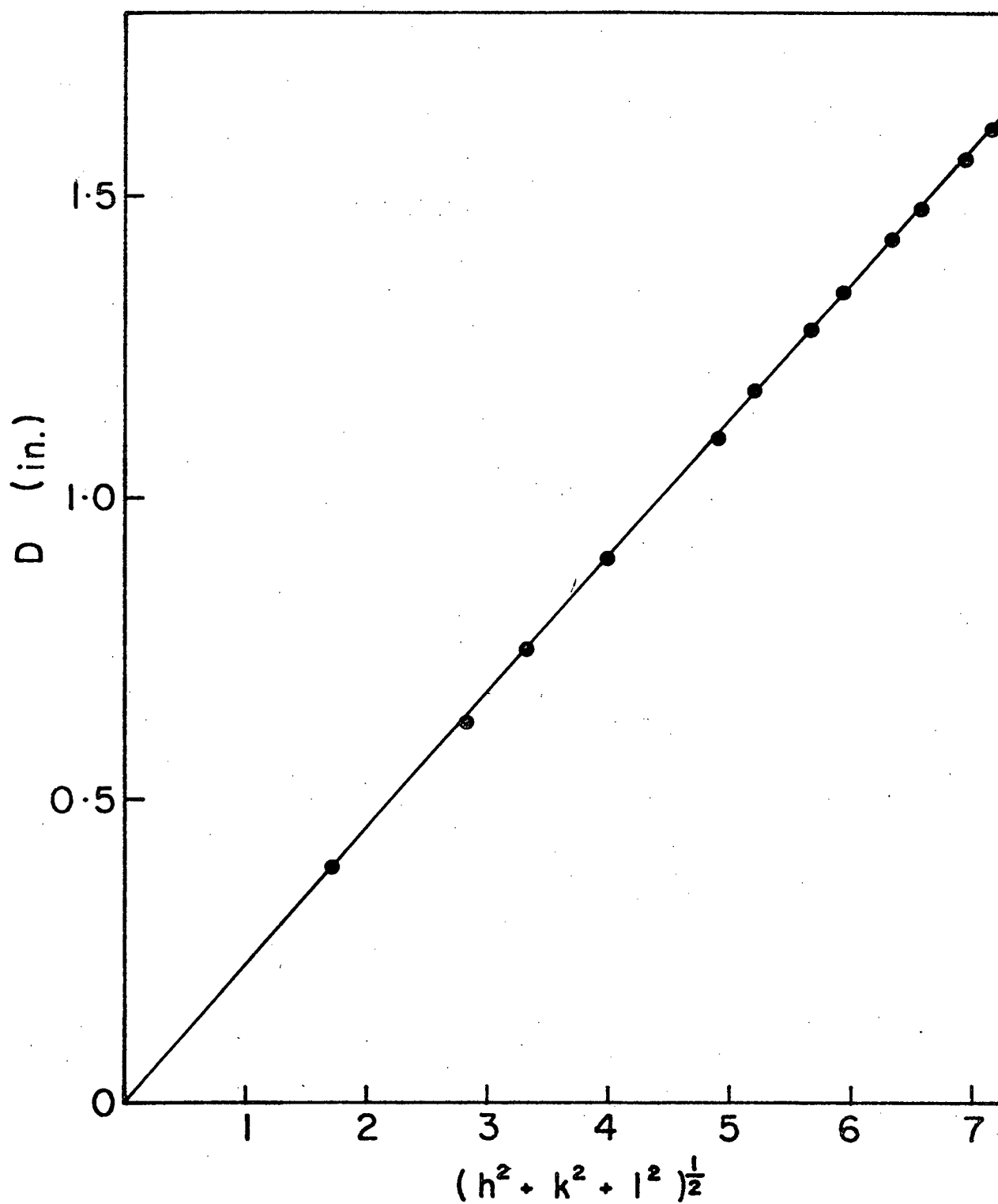$a_o = \dfrac{1.88 \text{ A}°}{0.224}$

Lattice parameter $a_o = 8.39$ A°
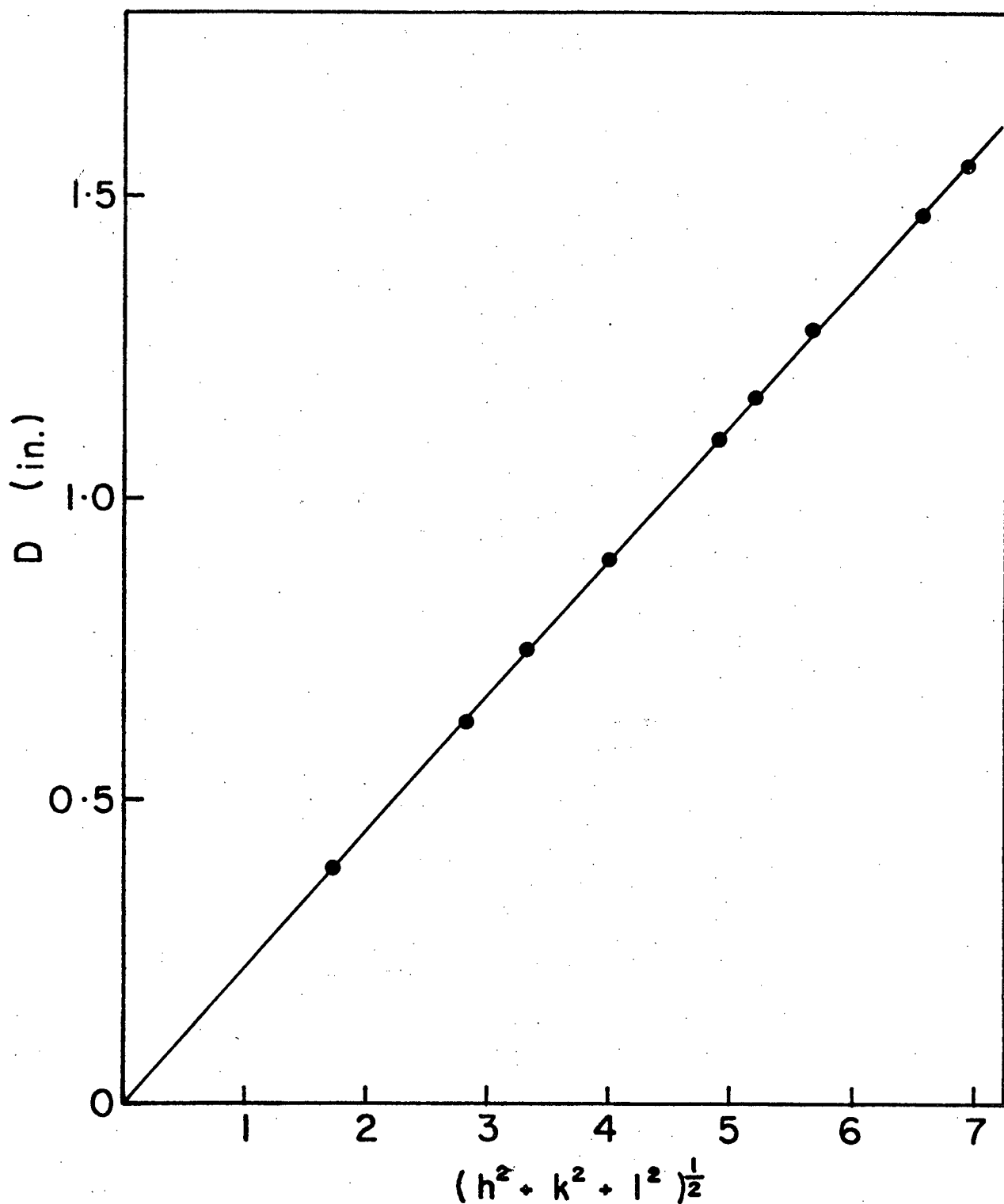
Fig. A3. Plot of D vs $(h^2 + k^2 + l^2)^{\frac{1}{2}}$ from Table A3. Diffraction pattern #23389, 304 s.c.c. in $MgCl_2$, oxide stripped with 1% bromine-methanol solution.

Table A4. 304 S.C.C. in $MgCl_2$ + $CoCl_2$, Oxide Stripped in 1% Bromine-
Methanol Solution
pattern #23462   camera constant K = 1.84 ins·A°

line	D in.	dA°	I_v	$FeCr_2O_4$ (hkl)	$\sqrt{h^2 + k^2 + l^2}$
1	0.375	4.91	M	111	1.73
2	0.61	3.02	W	220	2.83
3	0.72	2.55	S	311	3.32
4	0.87	2.12	S	400	4
5	1.12	1.64	WM	511/333	5.2
6	1.22	1.51	M	440	5.66
7	1.29	1.43	VW	–	–
8	1.42	1.30	VW	533	6.56
9	1.50	1.23	W	444	6.93
10	1.55	1.19	VW	711/551	7.14
11	1.66	1.11	VW	553/731	7.6
12	1.73	1.06	VW	800	8.0

Data plotted in Fig. A4, D vs $(h^2 + k^2 + l^2)^{\frac{1}{2}}$

Slope $M = \frac{K}{a_o} = 0.216$

$a_o = \frac{1.84 \text{ A°}}{0.216}$

Lattice parameter a_o = 8.52 A°
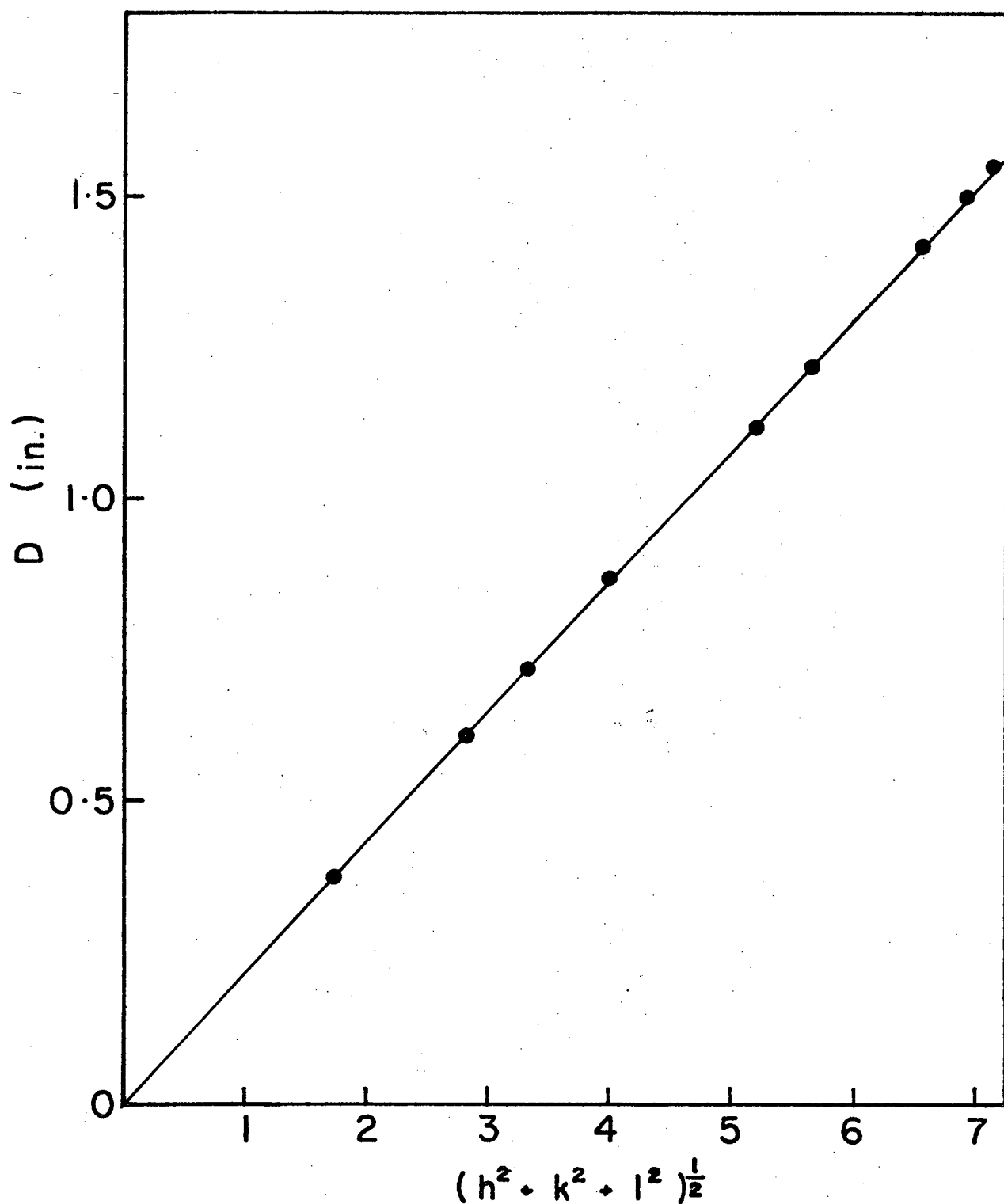
Fig. A4. Plot of D vs $(h^2 + k^2 + l^2)^{\frac{1}{2}}$ from Table A4. Diffraction pattern #23462, 304 s.c.c. in $MgCl_2$ + $CoCl_2$, oxide stripped with 1% bromine-methanol solution.

<u>Table A5.</u>   304 S.C.C. in $MgCl_2$ + $CoCl_2$, Oxide Stripped in 1% Bromine-
Methanol Solution
pattern #23459   camera constant K = 1.84 ins· A°

line	D in.	dA°	I_v	$FeCr_2O_4$ (hkl)	$\sqrt{h^2 + k^2 + l^2}$
1	0.38	4.84	M	111	1.73
2	0.62	2.97	W	220	2.83
3	0.72	2.55	S	311	3.32
4	0.87	2.12	M	400	4
5	0.95	1.94	VVW	331	4.36
6	1.08	1.70	VW	422	4.90
7	1.12	1.64	M	511/333	5.2
8	1.22	1.51	W	400	5.66
9	1.29	1.43	VW	-	-
10	1.43	1.29	VVW	533	6.56
11	1.50	1.23	VVW	444	6.93
12	1.55	1.19	VVW	711/551	7.14

Data plotted in Fig. A5, D vs $(h^2 + k^2 + l^2)^{\frac{1}{2}}$

Slope $M = \dfrac{K}{a_o} = 0.216$ in

$a_o = \dfrac{1.84}{0.216}$ A°

Lattice parameter a_o = 8.52 A°

Fig. A5. Plot of D vs $(h^2 + k^2 + l^2)^{\frac{1}{2}}$ from Table A5. Diffraction pattern #23459, 304 s.c.c. in $MgCl_2$ + $CoCl_2$, oxide stripped with 1% bromine-methanol solution.

Table A6. 304 S.C.C. in $MgCl_2$ + $CoCl_2$, Oxide Stripped with 1% Bromine-Methanol Solution

pattern #23464   camera constant K = 1.80 ins·A°

line	D in.	dA°	I_v	$FeCr_2O_4$ (hkl)	$\sqrt{h^2 + k^2 + l^2}$
1	0.38	4.74	M	111	1.73
2	0.61	2.95	W-M	220	2.83
3	0.72	2.50	S	311	3.32
4	0.75	2.40	W	222	3.46
5	0.81	2.22	VVW	-	-
6	0.85	2.12	M	400	4
7	0.94	1.92	W	331	4.36
8	1.06	1.70	W	422	4.90
9	1.13	1.60	W-M	511/333	5.2
10	1.23	1.46	W-M	440	5.66
11	1.29	1.40	W	531	5.92
12	1.36	1.32	VVW	620	6.32
13	1.42	1.27	W	533	6.56
14	1.49	1.21	W	444	6.93
15	1.54	1.17	VW	711	7.14

Data plotted in Fig. A6, D vs $(h^2 + k^2 + l^2)^{\frac{1}{2}}$

Slope $M = \dfrac{K}{a_o}$ = 0.216 in

$a_o = \dfrac{1.80}{0.216}$ A°

Lattice parameter a_o = 8.33 A°
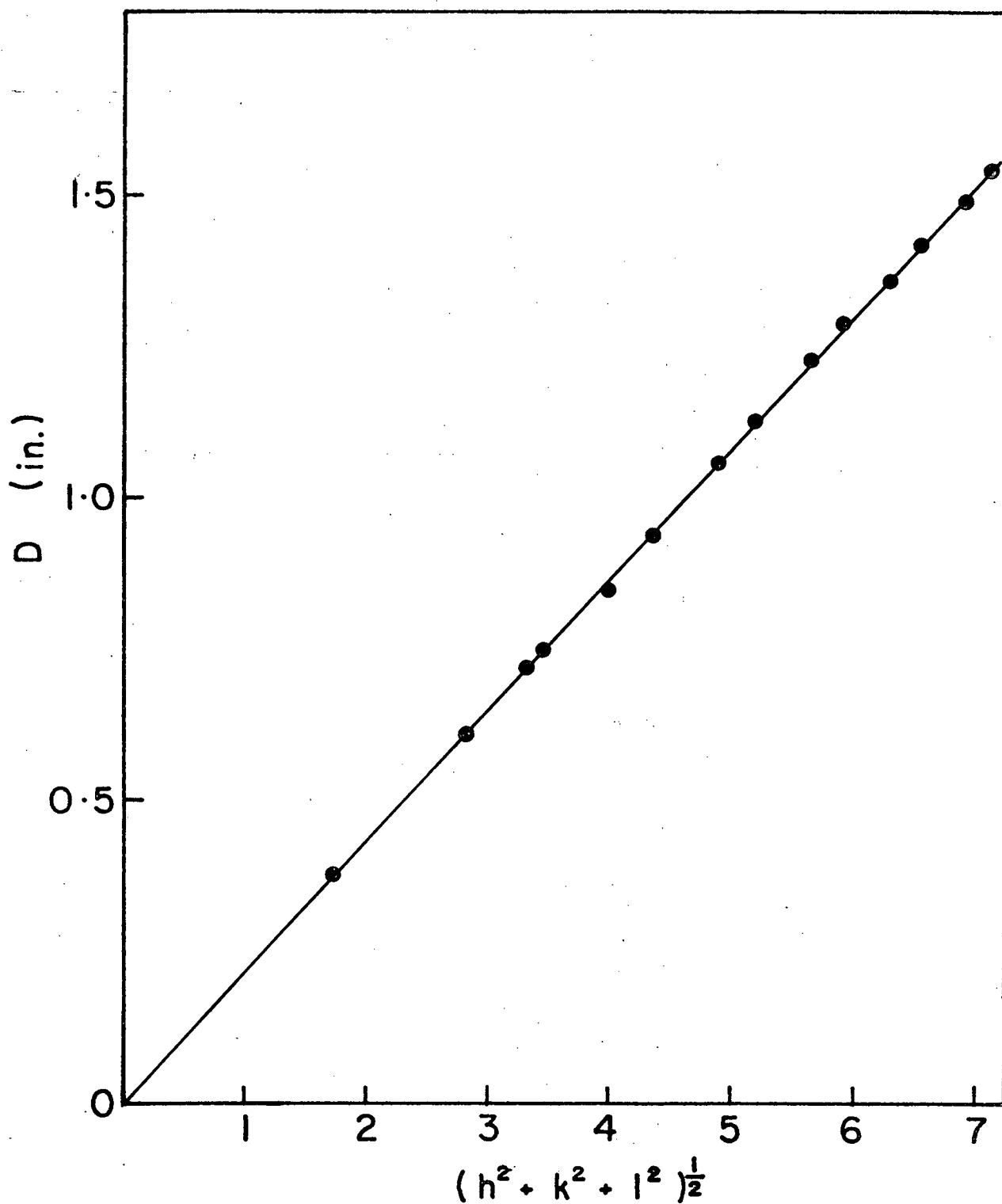
<u>Fig. A6.</u> Plot of D vs $(h^2 + k^2 + l^2)^{\frac{1}{2}}$ from Table A6. Diffraction pattern #23464, 304 s.c.c. in $MgCl_2$ + $CoCl_2$, oxide stripped with 1% bromine-methanol solution.

Table A7.   304 S.C.C. in $MgCl_2$ + HCl, Oxide Stripped with 1% Bromine-
Methanol Solution
pattern #23452   camera constant K = 1.91 ins·A°

line	D in.	dA°	I_v	$FeCr_2O_4$ (hkl)	$\sqrt{h^2 + k^2 + l^2}$
1	0.39	4.90	M	111	1.73
2	0.44	4.34	VVW	-	-
3	0.64	2.98	M	220	2.83
4	0.75	2.55	S	311	3.32
5	0.90	2.12	M	400	4.0
6	1.00	1.9.	VVW	331	4,36
7	1.11	1.72	W	422	4.9
8	1.18	1.62	M	511/333	5.2
9	1.28	1.49	M	440	5.66
10	1.34	1.42	VW	-	-
11	1.44	1.33	VW	620	6.32
12	1.49	1.28	W	533	6.56
13	1.57	1.22	W	444	6.93
14	1.62	1.18	VW	711/551	7.14

Data plotted in Fig. A7, D vs $(h^2 + k^2 + l^2)^{\frac{1}{2}}$

Slope $M = \dfrac{K}{a_o} = 0.227$ in

$a_o = \dfrac{1.91 \text{ A°}}{0.227}$

Lattice parameter a_o = 8.41 A°
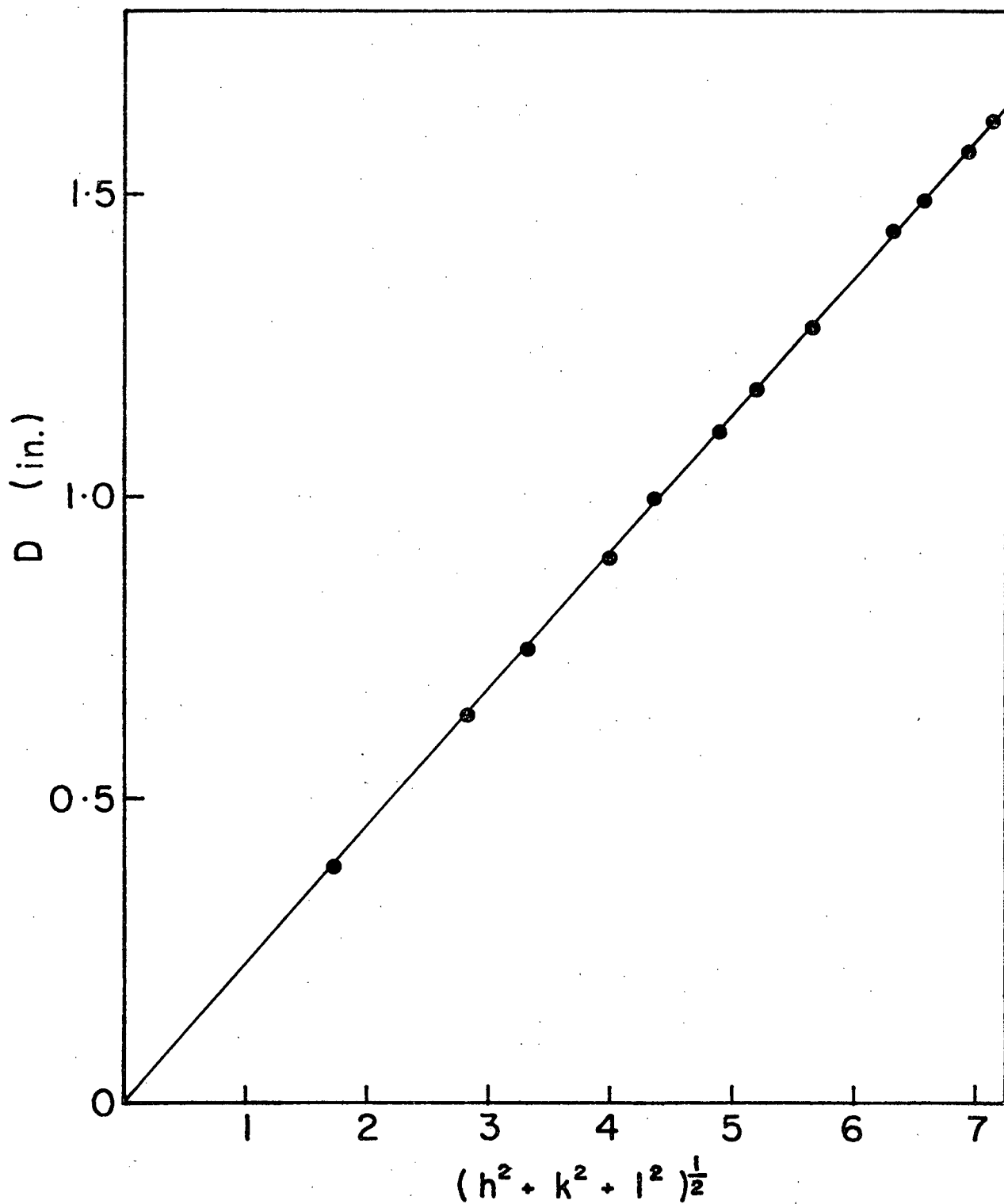
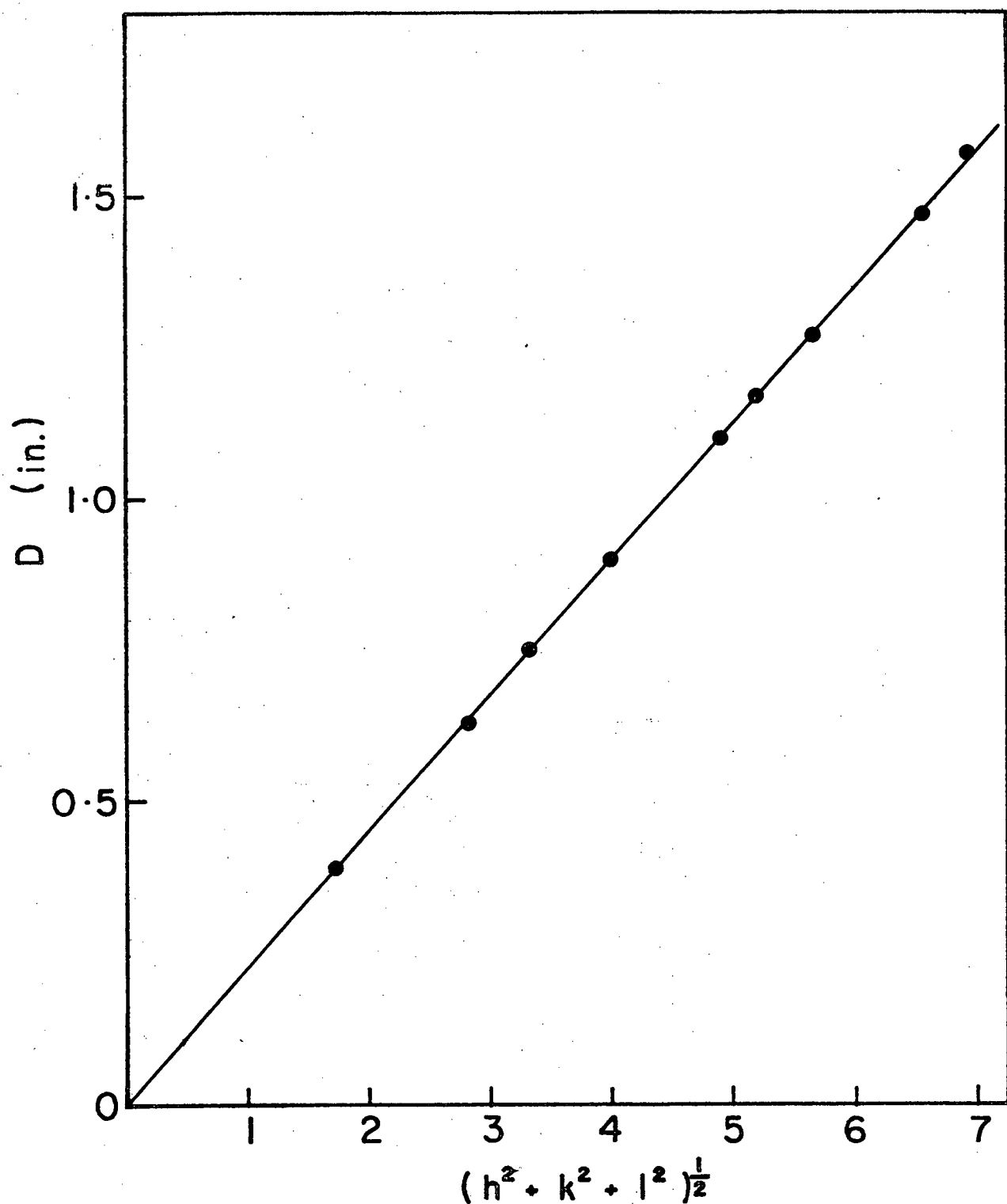Fig. A7. Plot of D vs $(h^2 + k^2 + l^2)^{\frac{1}{2}}$ from Table A7. Diffraction pattern #23452, 304 s.c.c. in $MgCl_2$ + HCl, oxide stripped with 1% bromine-methanol solution

Table A8. 304 S.C.C. in $MgCl_2$ + HCl, Oxide Stripped with 1% Bromine-Methanol Solution
pattern #23434   camera constant K = 1.91 ins·A°

line	D in.	dA°	I_v	$FeCr_2O_4$ (hkl)	$h^2 + k^2 + l^2$
1	0.39	4.90	M	111	1.73
2	0.64	2.98	M	220	2.83
3	0.76	2.51	VS	311	3.32
4	0.91	2.10	S	400	4.0
5	1.11	1.72	W	422	4.9
6	1.18	1.62	M	511/333	5.2
7	1.29	1.48	M	440	5.66
8	1.44	1.33	VW	620	6.32
9	1.48	1.29	W	533	6.56
10	1.57	1.22	W	444	6.93
11	1.61	1.19	VW	711/551	7.14

Data plotted in Fig. A8, D vs $(h^2 + k^2 + l^2)^{\frac{1}{2}}$

Slope $M = \dfrac{K}{a_o} = 0.226$ in

$$a_o = \frac{1.91 \text{ A°}}{0.226}$$
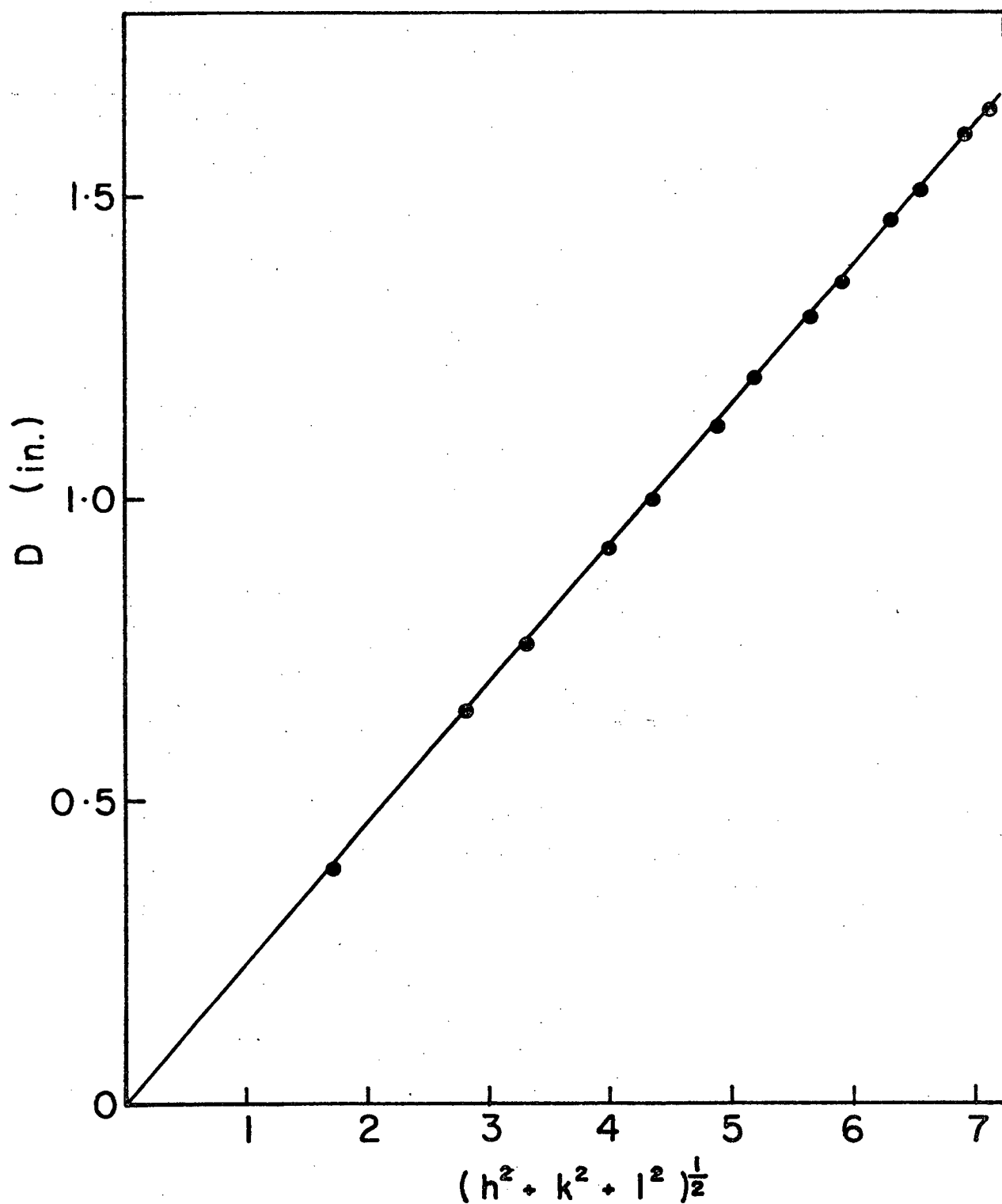
Lattice parameter $a_o = 8.45$ A°
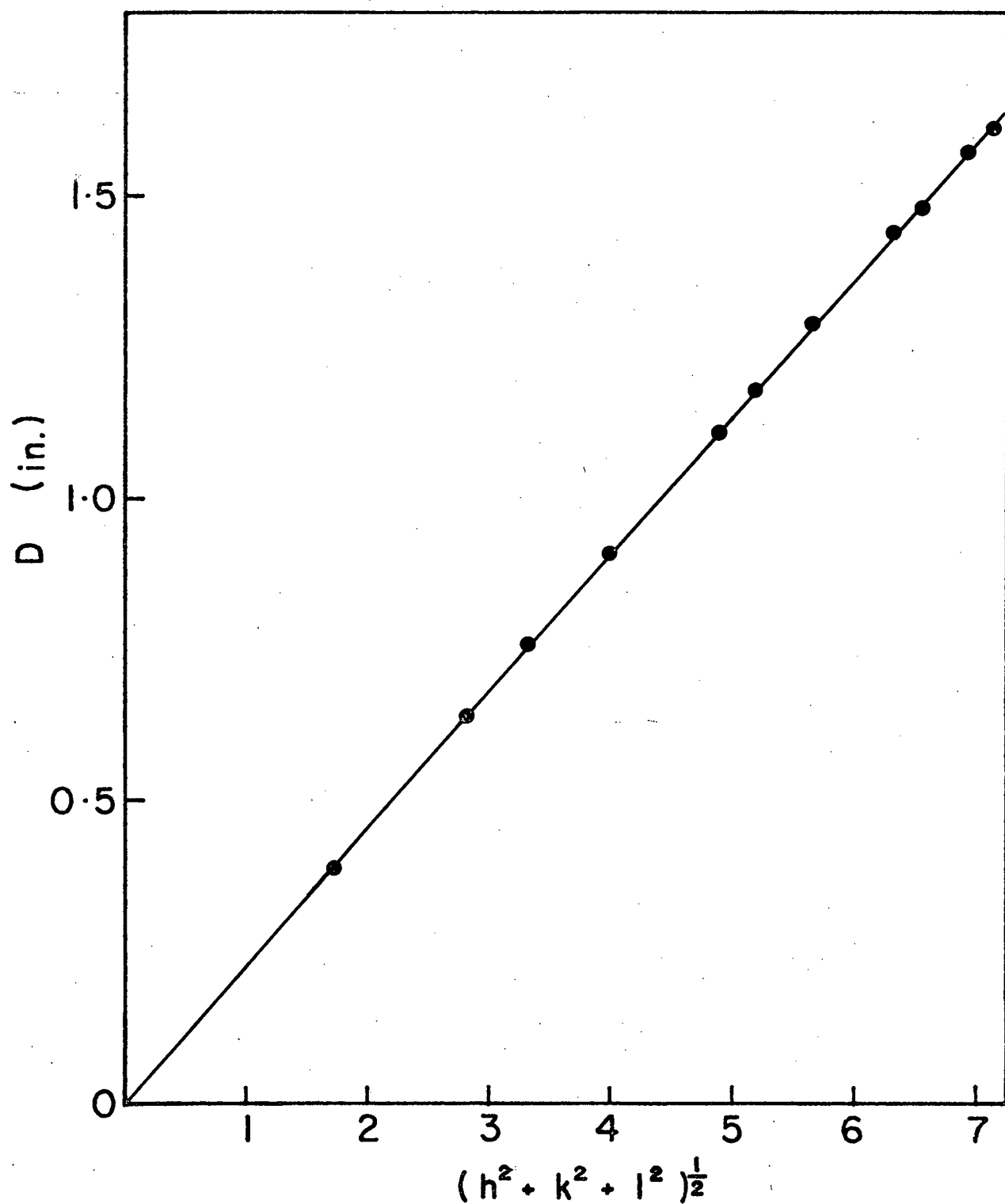
Fig. A8. Plot of D vs $(h^2 + k^2 + l^2)^{\frac{1}{2}}$ from Table A8. Diffraction pattern #23434, 304 s.c.c. in $MgCl_2$ + HCl, oxide stripped with 1% bromine-methanol solution.

Table A9. 304 S.C.C. in $MgCl_2$ + HCl, Oxide Stripped with 1% Bromine-
Methanol Solution
pattern #23436   camera constant K = 1.91 ins·A°

line	D in.	dA°	I_v	FeCr O_4 (hkl)	$\sqrt{h^2 + k^2 + l^2}$
1	0.39	4.90	M	111	1.73
2	0.51	3.75	VVW	-	-
3	0.63	3.03	S	220	2.83
4	0.75	2.55	VS	311	3.32
5	0.90	2.12	S	400	4.0
6	1.10	1.74	M	422	4.9
7	1.18	1.62	S	511/333	5.2
8	1.28	1.49	S	440	5.66
9	1.34	1.42	W	531	5.92
10	1.43	1.34	VW	620	6.32
11	1.48	1.29	W	533	6.56
12	1.56	1.22	W	444	6.93
13	1.61	1.19	VW	711/551	7.14

Data plotted in Fig. A9, D vs $(h^2 + k^2 + l^2)^{\frac{1}{2}}$

Slope $M = \dfrac{K}{a_o} = 0.226$ in

$a_o = \dfrac{1.91}{0.226}$ A°
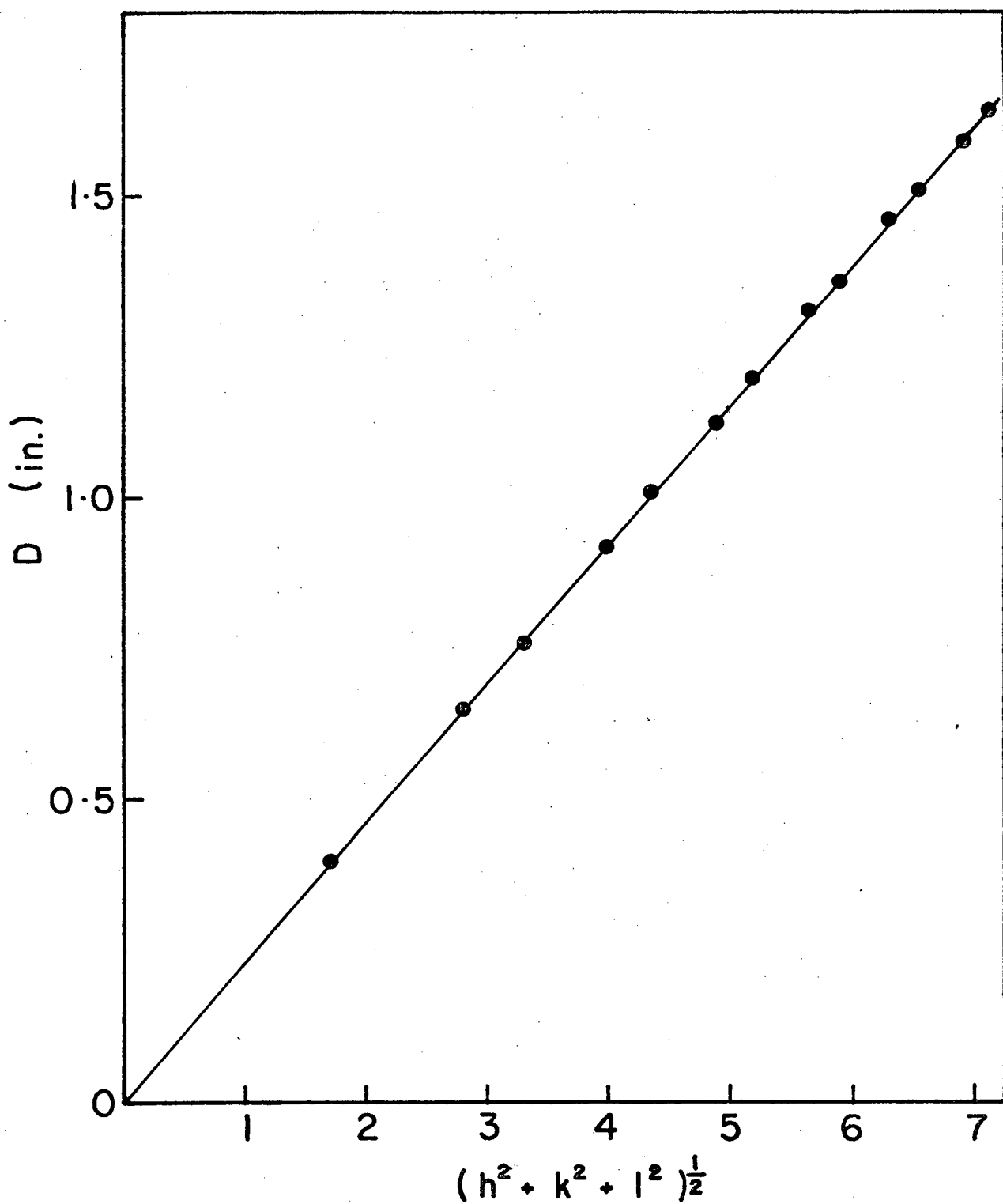
Lattice parameter $a_o = 8.45$ A°

Fig. A9. Plot of D vs $(h^2 + k^2 + l^2)^{\frac{1}{2}}$ from Table A9. Diffraction pattern #23436, 304 s.c.c. in $MgCl_2$ + HCl, oxide stripped with 1% bromine-methanol solution.

Table A10. 304 S.C.C. in $MgCl_2$ + $FeCl_3$, Oxide Stripped with 1% Bromine-Methanol Solution
pattern #23580   camera constant K = 1.90 ins·A°

line	D in.	dA°	I_v	$FeCr_2O_4$ (hkl)	$\sqrt{h^2 + k^2 + l^2}$
1	0.385	4.94	M	111	1.73
2	0.445	4.28	VVW	–	–
3	0.63	3.02	M	220	2.83
4	0.75	2.53	S	311	3.32
5	0.90	2.11	M	400	4.0
6	0.99	1.92	VVW	331	4.36
7	1.09	1.74	W	422	4.90
8	1.16	1.64	M	333/511	5.20
9	1.26	1.51	M	440	5.66
10	1.32	1.44	VW	531	5.92
11	1.41	1.35	VW	620	6.32
12	1.47	1.29	W	533	6.56
13	1.55	1.23	VW	444	6.93
14	1.60	1.19	VW	551/711	7.14

Data plotted in Fig. A10, D vs $(h^2 + k^2 + l^2)^{\frac{1}{2}}$

Slope $M = \dfrac{K}{a_o} = 0.223$ in

$a_o = \dfrac{1.90 \text{ A}°}{0.223}$

Lattice parameter $a_o = 8.52$ A°
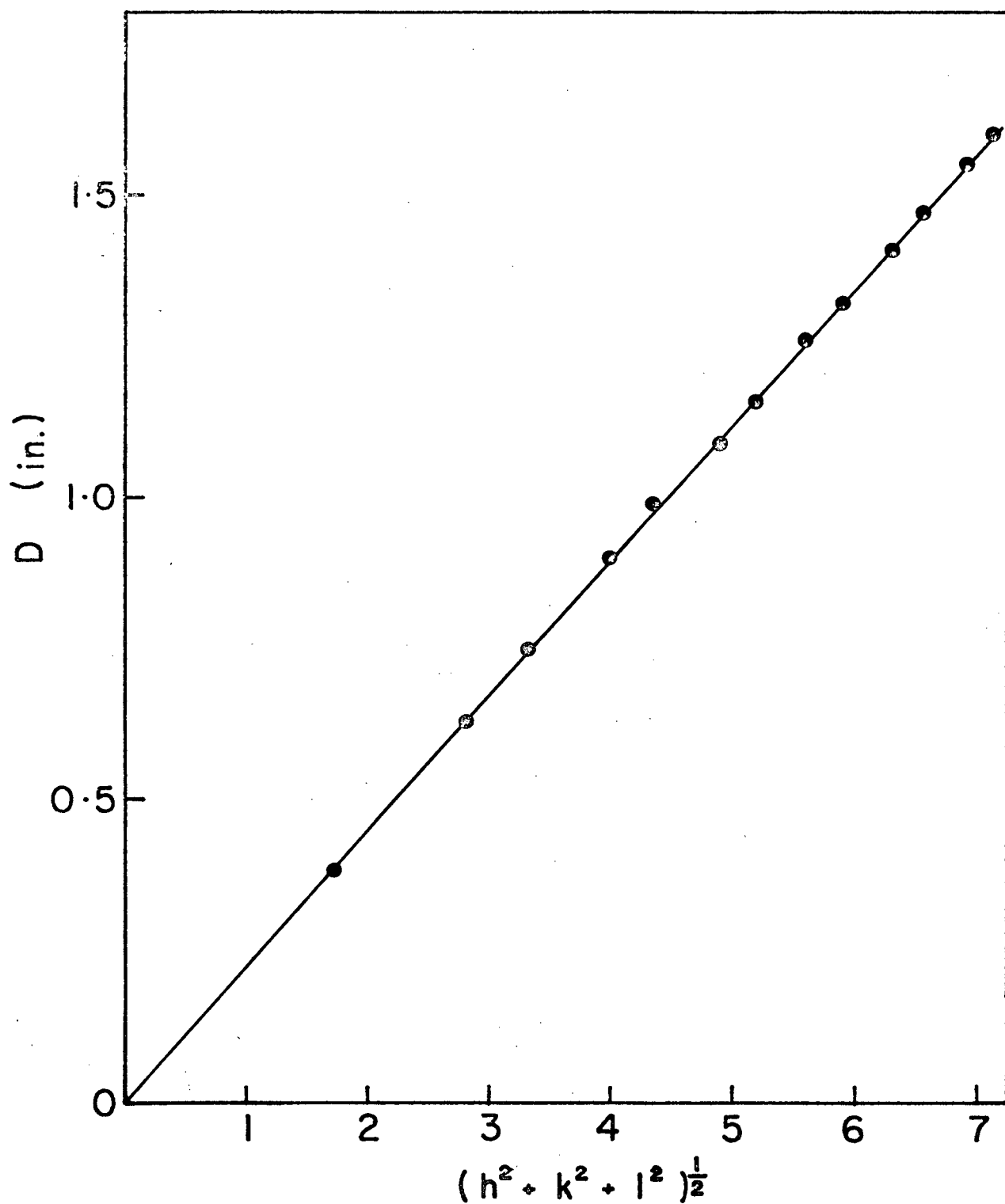
Fig. A10. Plot of D vs $(h^2 + k^2 + l^2)^{\frac{1}{2}}$ from Table A10. Diffraction pattern #23580, 304 s.c.c. in $MgCl_2$ + $FeCl_3$, oxide stripped with 1% bromine-methanol solution

Table A11. 304 S.C.C. in $MgCl_2$ + $FeCl_3$, Oxide Stripped with 1% Bromine-Methanol Solution
pattern #23579   camera constant K = 1.90 ins·A°

line	D in.	dA°	I_v	$FeCr_2O_4$ (hkl)	$\sqrt{h^2 + k^2 + l^2}$
1	0.39	4.87	M	111	1.73
2	0.44	4.32	VVW	–	–
3	0.515	3.70	W	–	–
4	0.635	2.99	M	220	2.83
5	0.71	2.68	W	–	–
6	0.75	2.53	S	311	3.32
7	0.86	2.21	W	–	–
8	0.90	2.11	M	400	4.0
9	1.03	1.85	VVW	–	–
10	1.1	1.73	W	422	4.9
11	1.17	1.62	M	511/333	5.2
12	1.27	1.50	M	440	5.66
13	1.33	1.43	VW	531	5.92
14	1.43	1.33	VW	620	6.32
15	1.47	1.29	W	533	6.56
16	1.56	1.22	VW	444	6.93
17	1.61	1.18	VW	711/551	7.14

Data plotted in Fig. A11, D vs $(h^2 + k^2 + l^2)^{\frac{1}{2}}$

Slope M = $\frac{K}{a_o}$ = 0.225 in

$a_o = \frac{1.90}{0.225}$ A°

Lattice parameter a_o = 8.44 A°
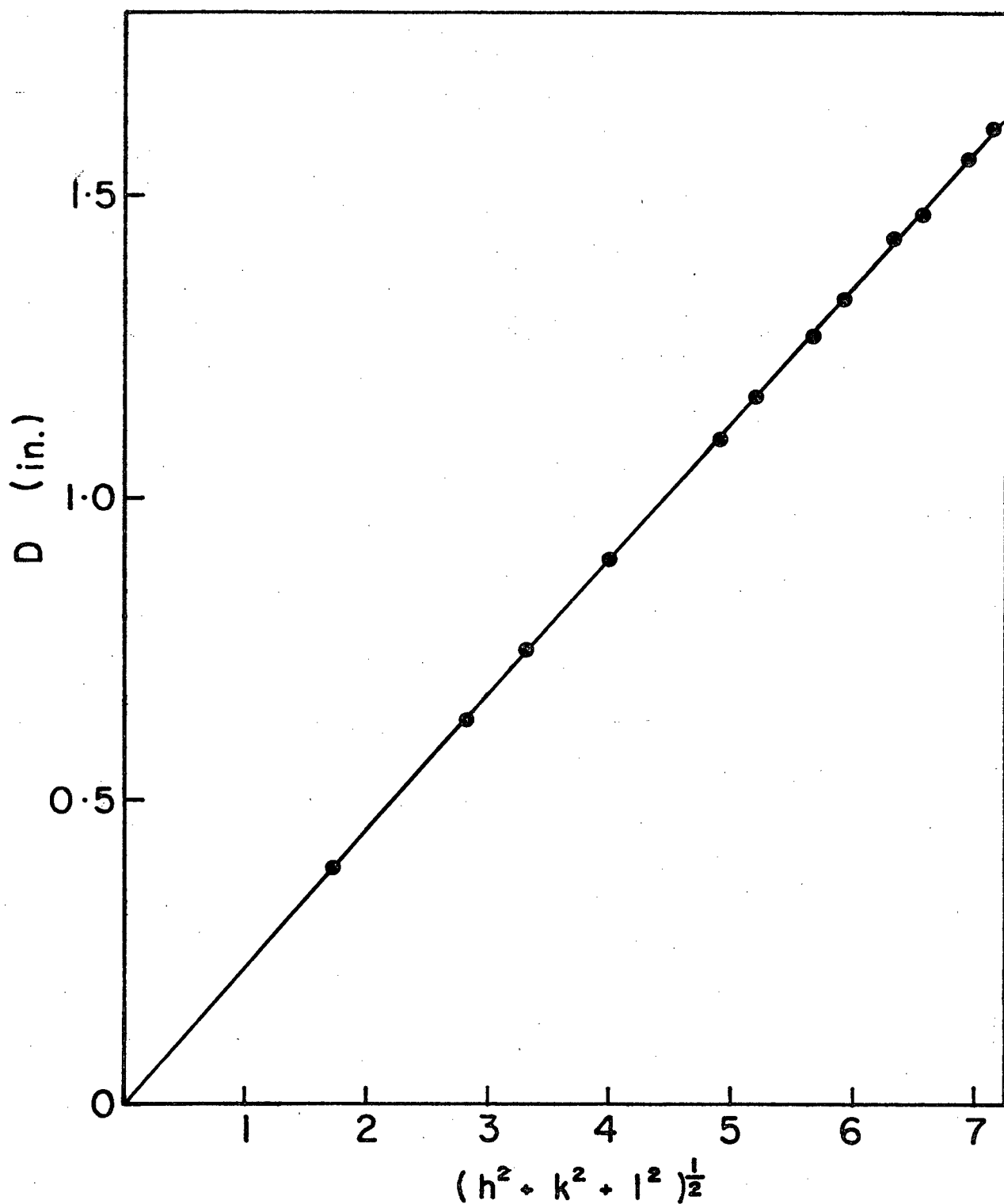
Fig. A11. Plot of D vs $(h^2 + k^2 + l^2)^{\frac{1}{2}}$ from Table A11. Diffraction pattern #23579, 304 s.c.c. in $MgCl_2$ + $FeCl_3$, oxide stripped with 1% bromine-methanol solution.

Table A12. 304 S.C.C. in $MgCl_2$ + $FeCl_3$, Oxide Stripped with 1% Bromine-Methanol Solution
pattern #23581   camera constant K = 1.90 ins·A°

line	D in.	dA°	I_v	$FeCr_2O_4$ (hkl)	$\sqrt{h^2 + k^2 + l^2}$
1	0.39	4.87	W	111	1.73
2	0.63	3.02	M	220	2.83
3	0.75	2.53	S	311	3.32
4	0190	2.11	M	400	4.0
5	1.1	1.73	VW	422	4.9
6	1.17	1.62	M	333/511	5.2
7	1.27	1.50	M-S	440	5.66
8	1.46	1.30	VW	533	6.56
9	1.57	1.21	VW	444	6.93

Data plotted in Fig. A12, D vs $(h^2 + k^2 + l^2)^{\frac{1}{2}}$

Slope $M = \dfrac{K}{a_o} = 0.225$ in

$a_o = \dfrac{1.90 \; A°}{0.225}$

Lattice parameter $a_o = 8.44 \; A°$

Fig. A12. Plot of D vs $(h^2 + k^2 + l^2)^{\frac{1}{2}}$ from Table A12. Diffraction pattern #23581, 304 s.c.c. in $MgCl_2$ + $FeCl_3$, oxide stripped with 1% bromine-methanol solution.

Table A13. 316 S.C.C. in $MgCl_2$, Oxide Stripped with 1% Bromine-Methanol
Solution
pattern #23333   camera constant K = 1.93 ins·A°

line	D in.	dA°	I_v	$FeCr_2O_4$ (hkl)	$\sqrt{h^2 + k^2 + l^2}$
1	0.39	4.95	W	111	1.73
2	0.65	2.97	M	220	2.83
3	0.76	2.54	S	311	3.32
4	0.92	2.10	M	400	4.00
5	1.00	1.93	VVW	331	4.36
6	1.12	1.72	W	422	4.90
7	1.2	1.61	M	511/333	5.20
8	1.3	1.48	M	440	5.66
9	1.36	1.42	VVW	531	5.92
10	1.46	1.32	VVW	620	6.32
11	1.51	1.28	M	533	6.56
12	1.60	1.21	W	444	6.93
13	1.64	1.18	W	711/551	7.14

Data plotted in Fig. A13, D vs $(h^2 + k^2 + l^2)^{\frac{1}{2}}$

Slope M = $\frac{K}{a_o}$ = 0.231 in

$a_o = \frac{1.93}{0.231}$ A°

Lattice parameter a_o = 8.36 A°

<u>Fig. A13.</u> Plot of D vs $(h^2 + k^2 + l^2)^{\frac{1}{2}}$ from Table A13. Diffraction pattern #23333, 316 s.c.c. in $MgCl_2$, oxide stripped with 1% bromine-methanol solution.

Table A14. 316 S.C.C. in $MgCl_2$, Oxide Stripped with 1% Bromine-Methanol
Solution
pattern #23329   camera constant K = 1.92 ins·A°

line	D in	dA°	I_v	$FeCr_2O_4$ (hkl)	$\sqrt{h^2 + k^2 + l^2}$
1	0.40	4.8	M	111	1.73
2	0.46	4.17	VVW	-	-
3	0.65	2.95	M	220	2.83
4	0.76	2.53	VS	311	3.32
5	0.92	2.09	S	400	4.0
6	1.01	1.91	VVW	331	4.36
7	1.125	1.71	W	422	4.90
8	1.2	1.60	M	333/511	5.20
9	1.31	1.47	M	440	5.66
10	1.36	1.41	M	531	5.92
11	1.46	1.32	VW	620	6.32
12	1.51	1.27	W	533	6.56
13	1.59	1.21	VW	444	6.93
14	1.64	1.17	VW	551/711	7.14

Data plotted in Fig. A14, D vs $(h^2 + k^2 + l^2)^{\frac{1}{2}}$

Slope $M = \dfrac{K}{a_o} = 0.230$ in

$a_o = \dfrac{1.92}{0.230}$ A°

Lattice parameter a_o = 8.35 A°

Fig. A14. Plot of D vs $(h^2 + k^2 + l^2)^{\frac{1}{2}}$ from Table A14. Diffraction pattern #23329, 316 s.c.c. in $MgCl_2$, oxide stripped with 1% bromine-methanol solution.

Table A15. 316 S.C.C. in $MgCl_2$, Oxide Stripped with 1% Bromine-Methanol Solution

pattern #22222   camera constant K = 1.91 ins·A°

line	D in.	dA°	I_v	$FeCr_2O_4$ (hkl)	$\sqrt{h^2 + k^2 + l^2}$
1	0.39	4.90	M	111	1.73
2	0.43	4.44	VW	-	-
3	0.53	3.60	VW	-	-
4	0.64	2.98	M	220	2.83
5	0.70	2.73	VVW	-	-
6	0.76	2.51	S	311	3.32
7	0.865	2.21	VVW	-	-
8	0.905	2.11	W	400	4.0
9	1.04	1.83	VVW	-	-
10	1.115	1.71	VW	422	4.90
11	1.18	1.52	W	333/511	5.20
12	1.285	1.49	S	400	5.66
13	1.32	1.45	VW	-	-
14	1.48	1.29	VVW	620	6.32
15	1.52	1.26	VVW	533	6.56
16	1.57	1.21	VW	444	6.93

Tata plotted in Fig. A15, D vs $(h^2 + k^2 + l^2)^{\frac{1}{2}}$

Slope M = $\dfrac{K}{a_o}$ = 0.230 in

$a_o = \dfrac{1.91}{.230}$ A°

Lattice parameter a_o = 8.30 A°
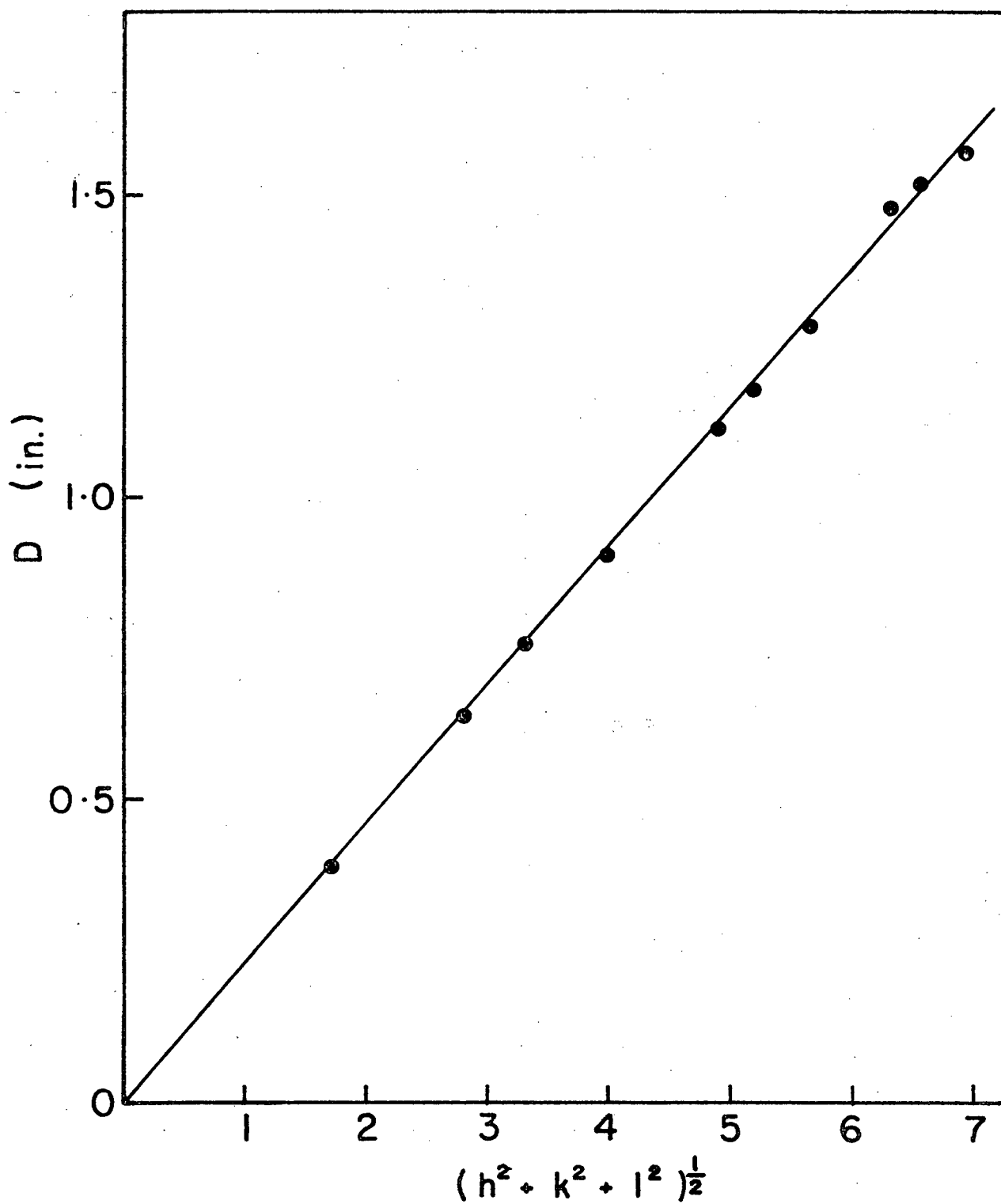
Fig. A15. Plot of D vs $(h^2 + k^2 + l^2)^{\frac{1}{2}}$ from Table A15. Diffraction pattern #22222, 316 s.c.c. in $MgCl_2$, oxide stripped with 1% bromine-methanol solution.

Table A16. 316 S.C.C. in $MgCl_2$ + HCl, Oxide Stripped with 1% Bromine-Methanol Solution

pattern #23406   camera constant K = 1.91 ins· A°

line	D in.	dA°	I_v	$FeCr_2O_4$ (hkl)	$\sqrt{h^2 + k^2 + l^2}$
1	0.395	4.84	M	111	1.73
2	0.46	4.15	VVW	–	–
3	0.525	3.64	M	–	–
4	0.56	3.41	VVW	–	–
5	0.64	2.98	M	220	2.83
6	0.705	2.71	M	–	–
7	0.76	2.51	S	311	3.32
8	0.875	2.18	M	–	–
9	0.91	2.10	M	400	4.0
10	1.01	1.89	VVW	331	4.36
11	1.05	1.82	W	–	–
12	1.12	1.71	W	422	4.90
13	1.18	1.62	M	511/333	5.20
14	1.29	1.48	M	440	5.66

Data plotted in Fig. A16, D vs $(h^2 + k^2 + l^2)^{\frac{1}{2}}$

Slope M = $\frac{K}{a_o}$ = 0.226 in

$a_o = \frac{1.91}{0.226}$ A°

Lattice parameter a_o = 8.45 A°
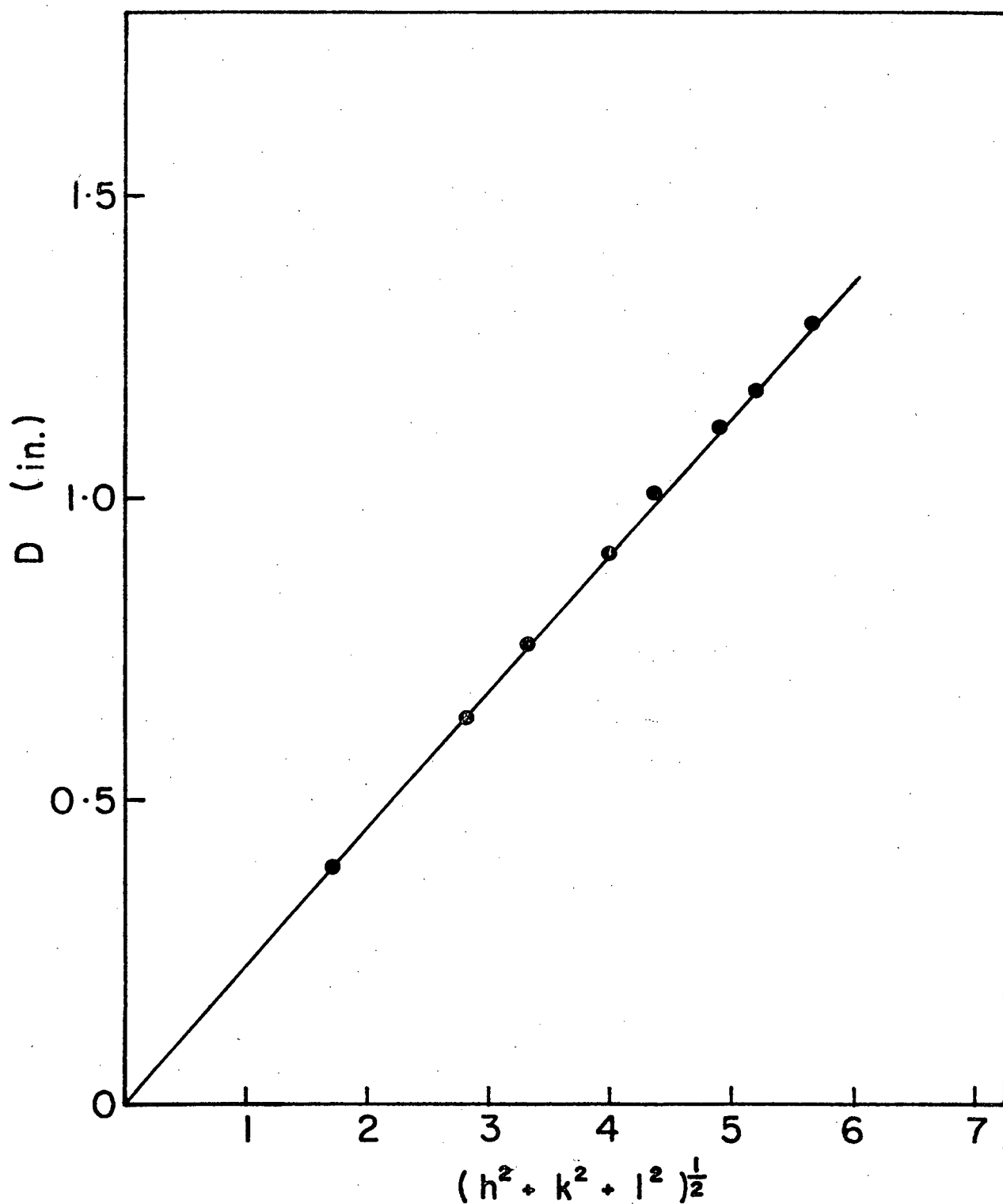
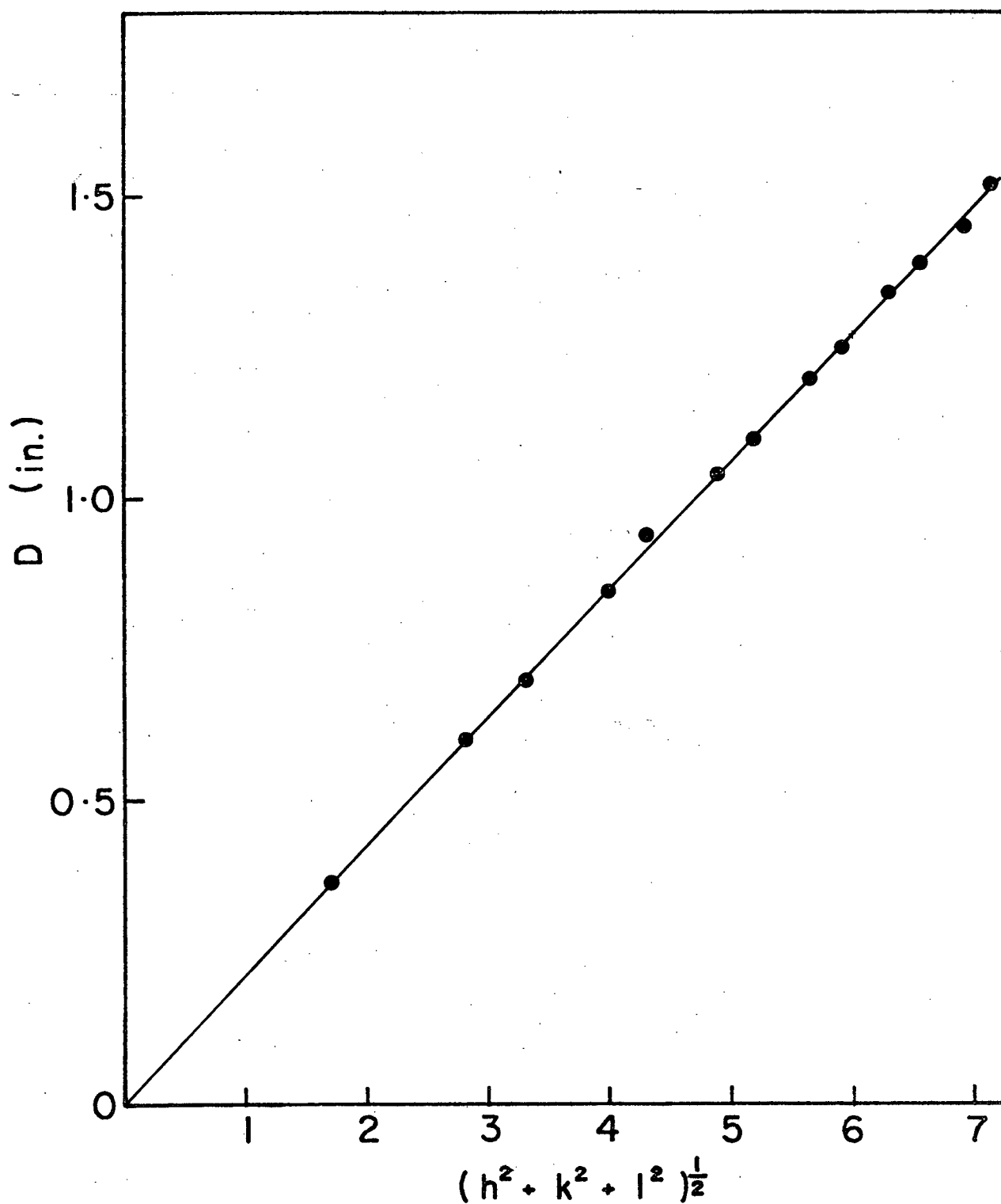<u>Fig. A16.</u> Plot of D vs $(h^2 + k^2 + l^2)^{\frac{1}{2}}$ from Table A16. Diffraction pattern #23406, 316 s.c.c. in $MgCl_2$+ HCl, oxide stripped with 1% bromine-methanol solution.

Table A17. 316 S.C.C. in $MgCl_2$ + HCl, Oxide Stripped with 1% Bromine-
Methanol Solution
pattern #23407   camera constant K = 1.91 ins.A°

line	D in.	dA°	I_v	$FeCr_2O_4$ (hkl)	$\sqrt{h^2 + k^2 + l^2}$
1	0.39	4.90	M	111	1.73
2	0.64	2.98	M	220	2.83
3	0.76	2.51	S	311	3.32
4	0.91	2.10	M	400	4.0
5	1.11	1.72	W	422	4.90
6	1.18	1.61	M	511/333	5.2
7	1.28	1.49	M	440	5.66
8	1.35	1.42	VW	531	5.92
9	1.43	1.34	VW	621	6.32
10	1.50	1.27	W	533	6.56
11	1.58	1.21	W	444	6.93
12	1.62	1.18	VW	551/711	7.14

Data plotted in Fig. A17, D vs $(h^2 + k^2 + l^2)^{\frac{1}{2}}$

Slope M = $\dfrac{K}{a_o}$ = 0.228 in.

$a_o = \dfrac{1.91}{0.228}$ A°

Lattice parameter a_o = 8.38 A°
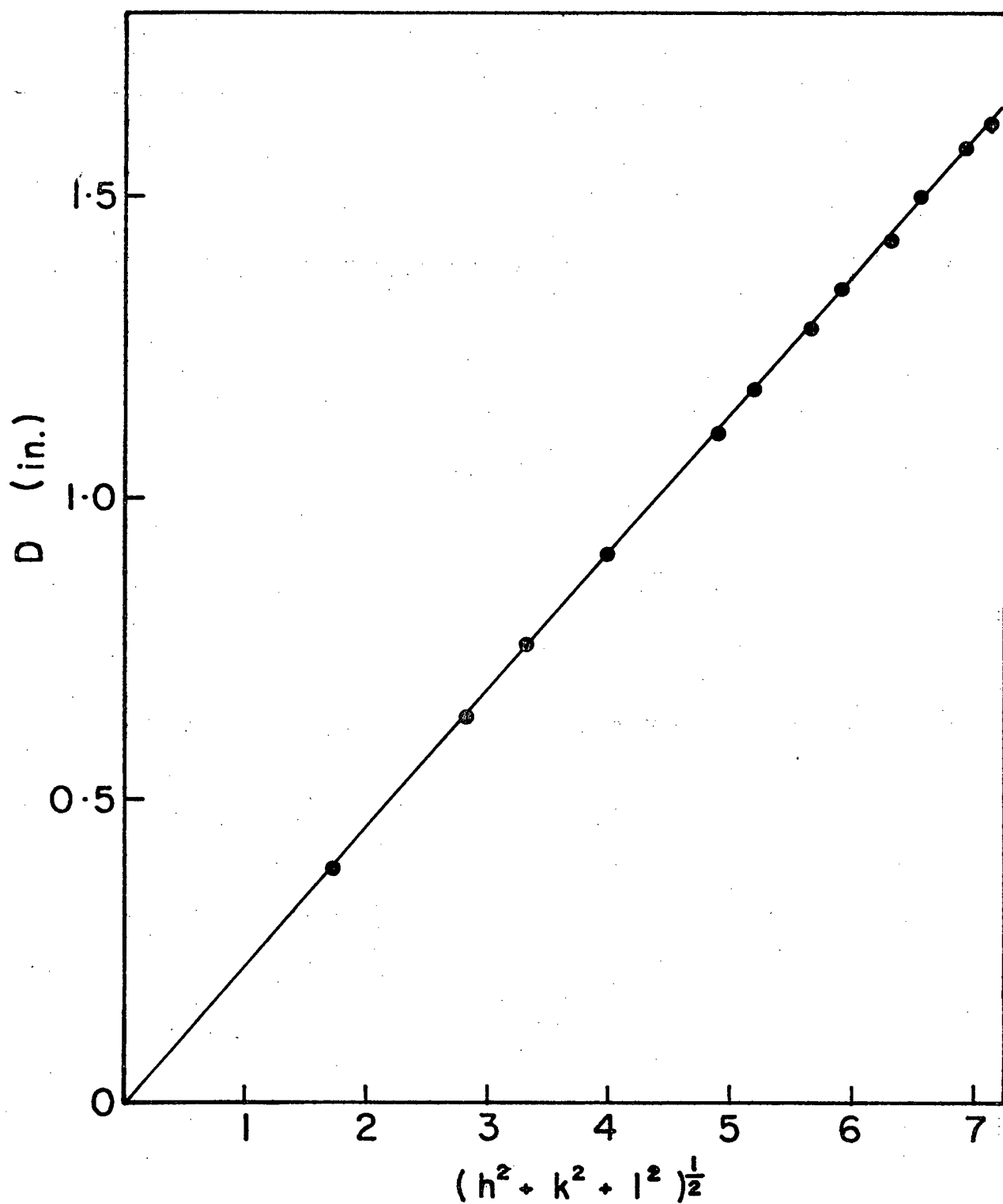
<u>Fig. A17.</u> Plot of D vs $(h^2 + k^2 + l^2)^{\frac{1}{2}}$ from Table A17. Diffraction pattern #23407, 316 s.c.c. in $MgCl_2$ + HCl, oxide stripped with 1% bromine-methanol solution

Table A18. 316 S.C.C. in $MgCl_2$ + HCl, Oxide Stripped with 1% Bromine-
Methanol Solution
pattern #23404   camera constant K = 1.91 ins·A°

line	D in.	dA°	I_v	$FeCr_2O_4$ (hkl)	$\sqrt{h^2 + k^2 + l^2}$
1	0.385	4.96	M	111	1.73
2	0.45	4.24	VVW	–	–
3	0.64	2.98	M	220	2.83
4	0.745	2.56	S	311	3.32
5	0.785	2.43	W	222	3.46
6	0.90	2.12	M	400	4.0
7	0.985	1.94	VVW	331	4.36
8	1.02	1.88	VVW	–	–
9	1.1	1.74	W	422	4.90
10	1.17	1.63	M	511/333	5.2
11	1.28	1.49	M	440	5.66
12	1.34	1.43	VW	531	5.92
13	1.42	1.34	VW	620	6.32
14	1.48	1.29	W	533	6.56
15	1.56	1.22	W	444	6.93

Data plotted in Fig. A18, D vs $(h^2 + k^2 + l^2)^{\frac{1}{2}}$

Slope M = $\frac{K}{a_o}$ = 0.226 in.

$a_o = \frac{1.91}{0.226}$ A°

Lattice parameter a_o = 8.45 A°
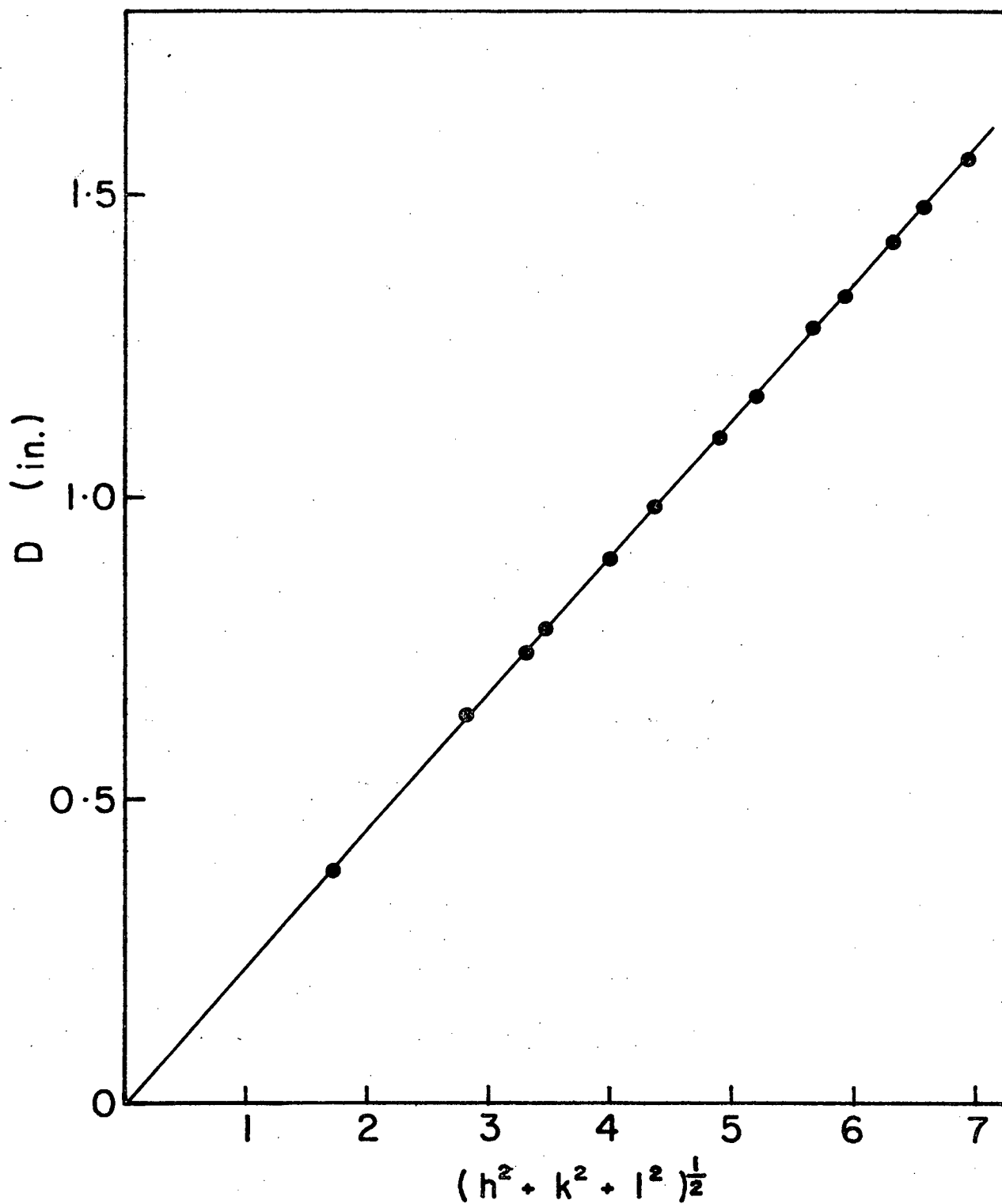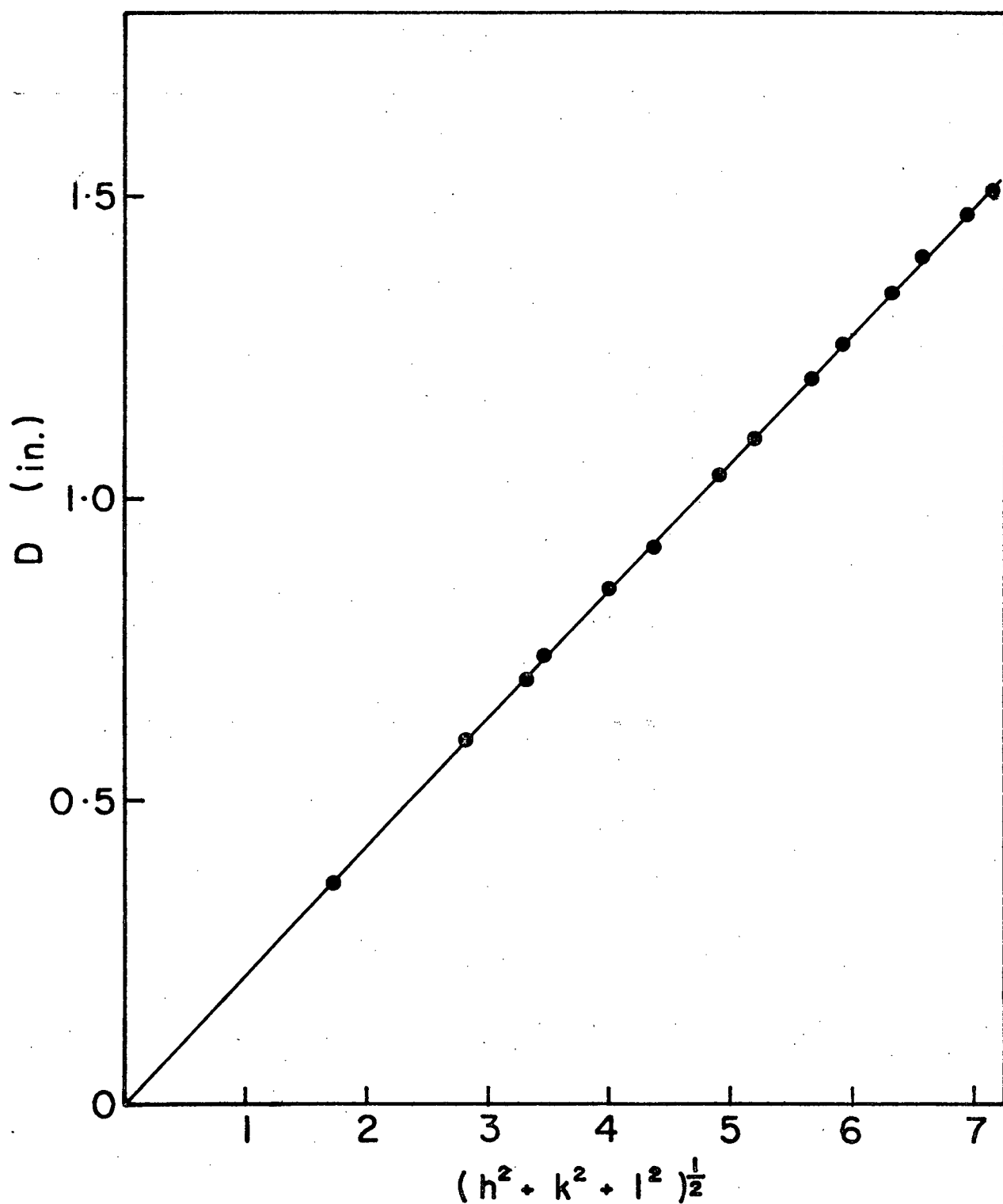
<u>Fig. A18.</u> Plot of D vs $(h^2 + k^2 + l^2)^{\frac{1}{2}}$ from Table A18. Diffraction pattern #23404, 316 s.c.c. in $MgCl_2$ + HCl, oxide stripped with 1% bromine-methanol solution.

Table A19. 316 S.C.C. in $MgCl_2$ + $CoCl_2$, Oxide Stripped with 1% Bromine-
Methanol Solution
pattern #23483   camera constant K = 1.80 ins·A°

line	-D in.	dA°	I_v	$FeCr_2O_4$ (hkl)	$\sqrt{h^2 + k^2 + l^2}$
1	0.365	4.93	M	111	1.73
2	0.60	3.0	M	220	2.83
3	0.70	2.57	S	311	3.32
4	0.80	2.25	VW	-	-
5	0.845	2.13	M	400	4.0
6	0.94	1.92	VVW	331	4.36
7	1.04	1.73	W	422	4.90
8	1.1	1.64	M	511/333	5.2
9	1.15	1.57	VVW	-	-
10	1.25	1.44	VVW	531	5.92
11	1.25	1.44	VVW	531	5.92
12	1.34	1.34	VW	620	6.32
13	1.39	1.30	W	533	6.56
14	1.45	1.24	VW	4.44	6.93
15	1.52	1.18	VW	551/711	7.14

Data plotted in Fig. A19, D vs $(h^2 + k^2 + l^2)^{\frac{1}{2}}$

Slope M = $\dfrac{K}{a_o}$ = 0.212 in.

$a_o = \dfrac{1.80}{0.212}$ A°

Lattice parameter a_o = 8.49 A°

Fig. A19.   Plot of D vs $(h^2 + k^2 + l^2)^{\frac{1}{2}}$ from Table A19.   Diffraction pattern #23483, 316 s.c.c. in $MgCl_2$ + $CoCl_2$, oxide stripped with 1% bromine-methanol solution

Table A20. 316 S.C.C. in $MgCl_2$ + $CoCl_2$, Oxide Stripped with 1% Bromine-Methanol Solution
pattern #23472   camera constant K = 1.80 ins·A°

line	D in.	dA°	I_v	$FeCr_2O_4$ (hkl)	$\sqrt{h^2 + k^2 + l^2}$
1	0.365	4.93	M	111	1.73
2	0.60	3.0	M	220	2.83
3	0.71	2.54	S	311	3.32
4	0.86	2.09	M	400	4.0
5	1.04	1.73	W	422	4.9
6	1.09	1.65	W	511/333	5.2
7	1.20	1.50	M	440	5.66
8	1.40	1.29	W	533	6.56
9	1.47	1.22	W	444	6.93
10	1.64	1.10	W	553/731	7.68
11	1.71	1.05	W	800	8.0

Data plotted in Fig. A20, D vs $(h^2 + k^2 + l^2)^{\frac{1}{2}}$

Slope $M = \dfrac{K}{a_o} = 0.213$ in.

$a_o = \dfrac{1.80 \; A°}{0.213}$

Lattice parameter a_o = 8.45 A°
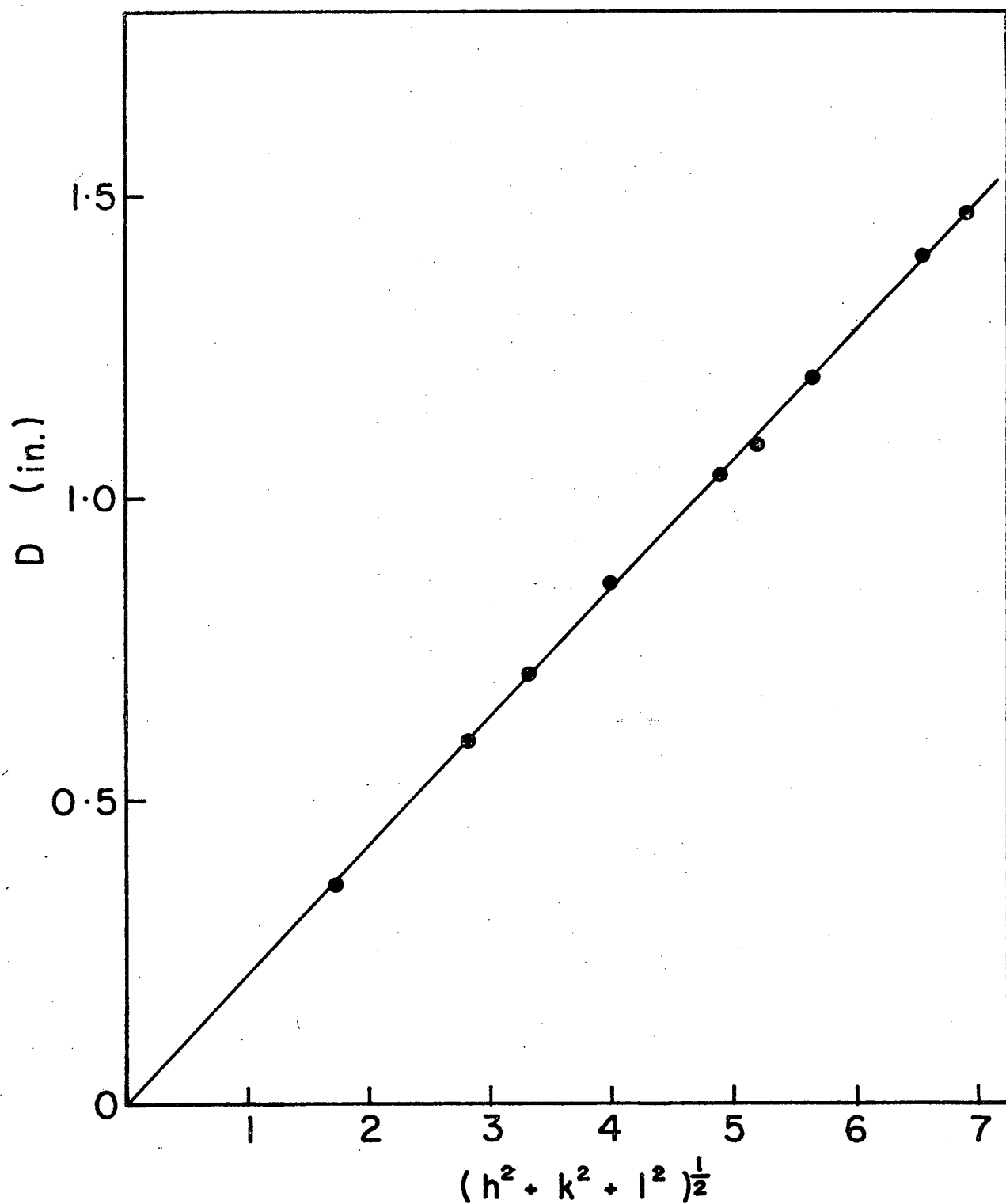
Fig. A20. Plot of D vs $(h^2 + k^2 + l^2)^{\frac{1}{2}}$ from Table A20. Diffraction pattern #23472, 316 s.c.c. in $MgCl_2$ + $CoCl_2$. oxide stripped with 1% bromine-methanol solution

Table A21. 316 S.C.C. in $MgCl_2$ + $CoCl_2$, Oxide Stripped with 1% Bromine-Methanol Solution
pattern #23474   camera constant K = 1.82 ins· A°

line	D in.	dA°	I_v	$FeCr_2O_4$ (hkl)	$\sqrt{h^2 + k^2 + l^2}$
1	0.365	4.99	M	111	1.73
2	0.60	3.03	M	220	2.83
3	0.70	2.6	S	311	3.32
4	0.74	2.46	W	222	3.46
5	0.85	2.14	M	400	4.0
6	0.92	1.98	VW	331	4.36
7	1.04	1.75	W	422	4.90
8	1.10	1.65	M	511/333	5.20
9	1.20	1.52	M	440	5.66
10	1.255	1.45	VW	531	5.92
11	1.34	1.36	VW	620	6.32
12	1.40	1.30	W	533	6.56
13	1.47	1.24	W	444	6.93
14	1.51	1.21	VW	711/551	7.14

Data plotted in Fig. A21, D vs $(h^2 + k^2 + l^2)^{\frac{1}{2}}$

Slope M = $\frac{K}{a_o}$ = 0.212 in.

$a_o = \frac{1.82}{0.212}$ A°

Lattice parameter a_o = 8.58 A°

Fig. A21. Plot of D vs $(h^2 + k^2 + l^2)^{\frac{1}{2}}$ from Table A21. Diffraction pattern #23474, 316 s.c.c. in $MgCl_2$ + $CoCl_2$, oxide stripped with 1% bromine-methanol solution.

Table A22. 310 S.C.C. in $MgCl_2$, Oxide Stripped with 1% Bromine-Methanol
Solution
pattern #22205   camera constant K = 1.91 ins. A°

line	D in.	dA°	I_v	$FeCr_2O_4$ (hkl)	$\sqrt{h^2 + k^2 + l^2}$
1	0.39	4.9	M	111	1.73
2	0.52	3.68	VW	–	–
3	0.64	2.98	W	220	2.83
4	0.72	2.66	VW	–	–
5	0.75	2.55	S	311	3.32
6	0.86	2.22	VW	–	–
7	0.91	2.10	M	400	4.0
8	1.04	1.84	VW	–	–
9	1.13	1.69	VW	422	4.9
10	1.18	1.62	W	333/511	5.2
11	1.29	1.48	M	440	5.66
12	1.27	1.30	VW	533	6.56

Data plotted in Fig. A22, D vs $(h^2 + k^2 + l^2)^{\frac{1}{2}}$

Slope $M = \dfrac{K}{a_o} = 0.227$ in.

$$a_o = \frac{1.91}{0.227} \text{ A°}$$
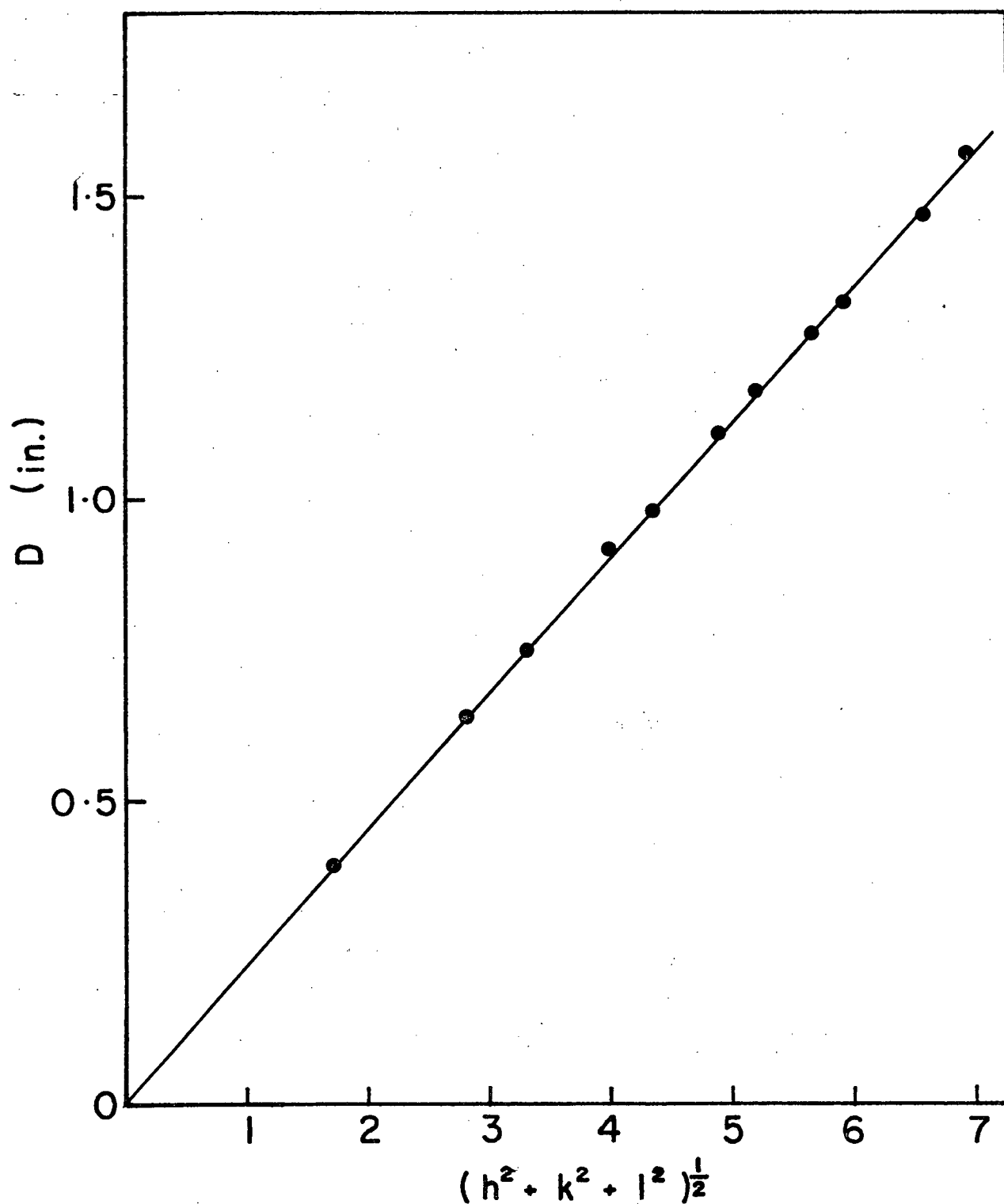
Lattice parameter $a_o = 8.41$ A°
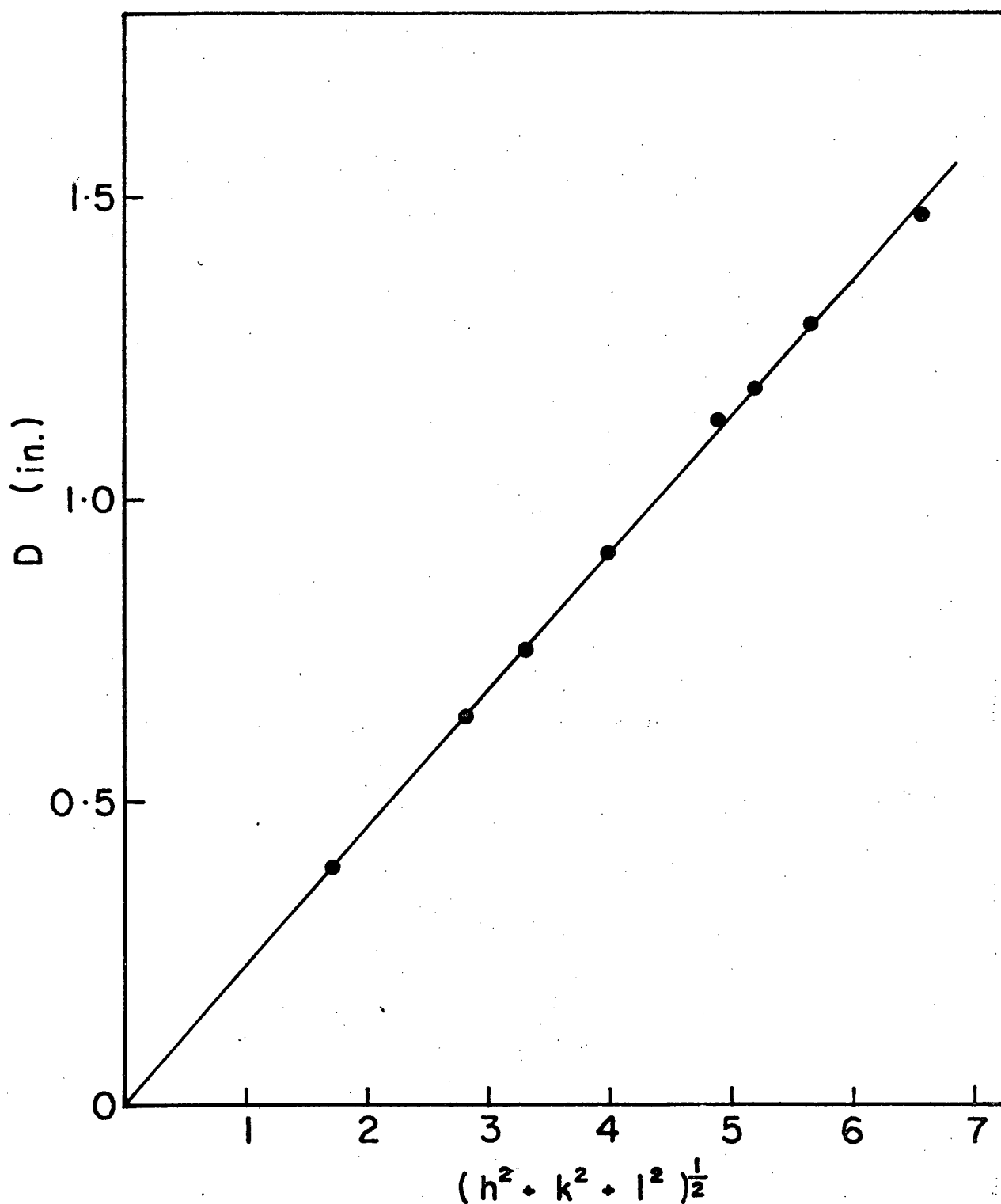
Fig. A22. Plot of D vs $(h^2 + k^2 + l^2)^{\frac{1}{2}}$ from Table A22. Diffraction pattern #22205, 310 s.c.c. in $MgCl_2$, oxide stripped with 1% bromine-methanol solution.

Table A23. 310 S.C.C. in MgCl$_2$, Oxide Stripped with 1% Bromine-
Methanol Solution
pattern #22200   camera constant K = 1.88 ins· A°

line	D in.	dA°	I$_v$	FeCr$_2$C$_4$ (hkl)	$\sqrt{h^2 + k^2 + l^2}$
1	0.39	4.82	M	111	1.73
2	0.42	4.48	Dots	–	0
3	0.54	3.48	Dota	–	–
4	0.635	2.96	S	220	2.83
5	0.74	2.54	S	311	3.32
6	0.79	2.38	Dots	222	3.46
7	0.89	2.11	VW	400	4.0
8	0.98	1.92	VW	331	4.36
9	1.11	1.70	VVW	422	4.9
10	1.17	1.61	W	333/511	5.2
11	1.27	1.48	VW	440	5.66
12	1.335	1.41	VW	531	5.92
13	1.42	1.32	Dots	620	6.32
14	1.47	1.29	Dots	533	6.56
15	1.56	1.21	Dots	444	6.93

Data plotted in Fig. A23, D vs $(h^2 + k^2 + l^2)^{\frac{1}{2}}$

Slope M = $\frac{K}{a_o}$ = 0.225 in.

$a_o = \frac{1.88}{0.225}$ A°

Lattice parameter a_o = 8.36 A°
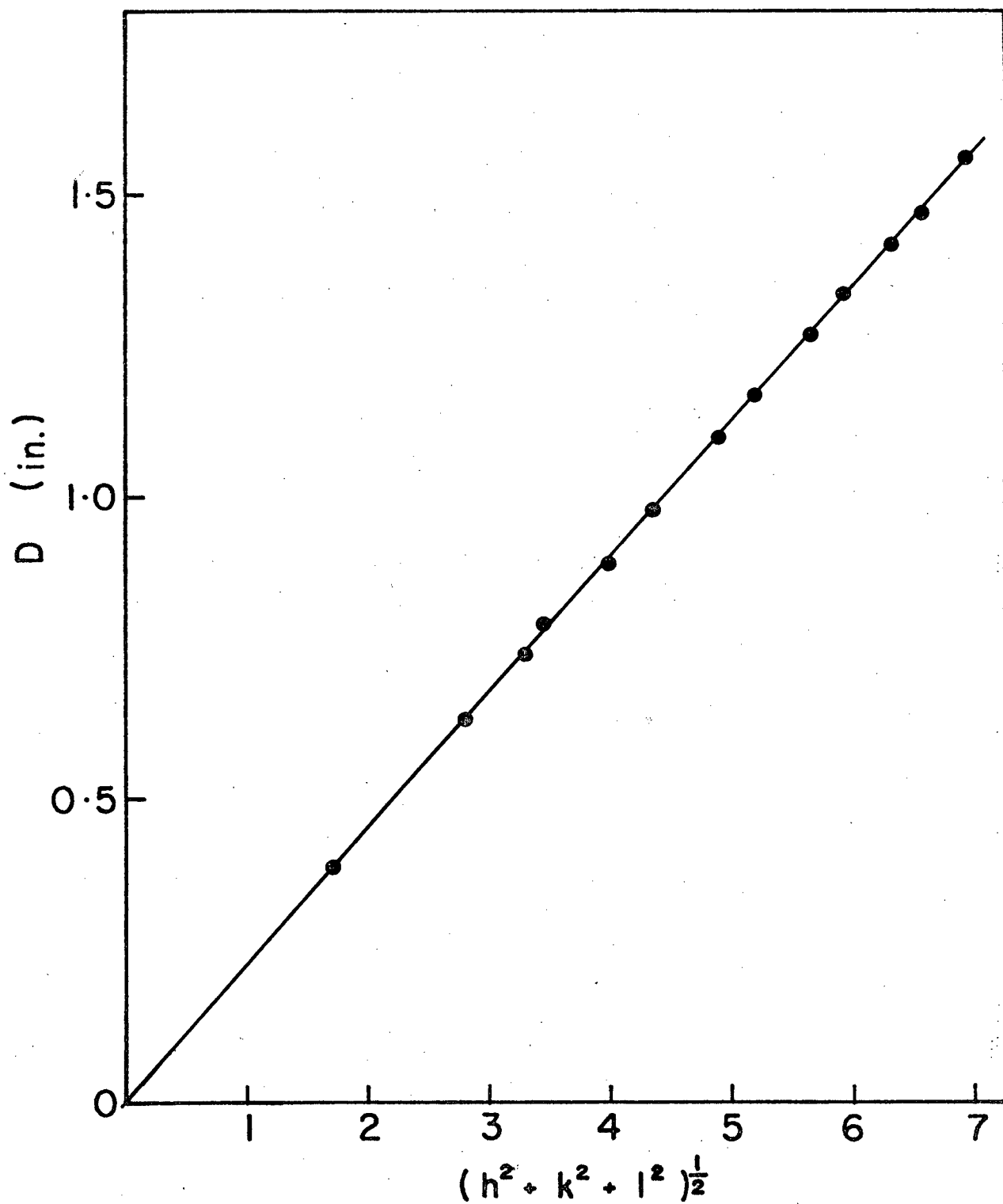
Fig. A23. Plot of D vs $(h^2 + k^2 + l^2)^{\frac{1}{2}}$ from Table A23. Diffraction pattern #22200, 310 s.c.c. in $MgCl_2$, oxide stripped with 1% bromine-methanol solution.

Table A24. 310 S.C.C. in $MgCl_2$, Oxide Stripped with 1% Bromine-Methanol Solution
pattern #22196   camera constant K = 1.88 ins· A°

line	D in.	dA°	I_v	$FeCr_2O_4$ (hkl)	$\sqrt{h^2 + k^2 + l^2}$
1	0.395	4.76	M	111	1.73
2	0.52	3.62	VW	-	-
3	0.64	2.94	W	220	2.83
4	0.72	2.61	VVW	-	-
5	0.75	2.51	S	311	3.32
6	0.86	2.19	VVW	-	-
7	0.915	2.06	S	400	4.0
8	0.98	1.92	VVW	331	4.36
9	1.04	1.81	VVW	-	-
10	1.11	1.69	VW	422	4.90
11	1.18	1.59	W	511/333	5.2
12	1.275	1.47	M	440	5.66
13	1.325	1.42	VW	531	5.92
14	1.47	1.28	VW	533	6.56
15	1.57	1.20	VW	444	6.93

Data plotted in Fig. A24, D vs $(h^2 + k^2 + l^2)^{\frac{1}{2}}$

Slope $M = \dfrac{K}{a_o} = 0.225$ in.

$$a_o = \frac{1.88 \text{ A}°}{0.225}$$

Lattice parameter $a_o = 8.36$ A°

Fig. A24. Plot of D vs $(h^2 + k^2 + l^2)^{\frac{1}{2}}$ from Table A24. Diffraction pattern #22196, 310 s.c.c. in $MgCl_2$, oxide stripped with 1% bromine-methanol solution.

Table A25. 310 S.C.C. in $MgCl_2$, Oxide Stripped with Cellulose
Acetate
pattern #23146   camera constant K = 2.28 ins. A°

line	D in.	dA°	I_v	$FeCr_2O_4$ (hkl)	$\sqrt{h^2 + k^2 + l^2}$
1	0.465	4.90	M	111	1.73
2	0.64	3.56	VVW	–	–
3	0.76	3.00	M	220	2.83
4	0.90	2.53	S	311	3.32
5	1.09	2.09	M	400	4.0
6	1.22	1.87	Dots	331	4.36
7	1.325	1.72	W	422	4.9
8	1.41	1.62	M	511/333	5.2
9	1.54	1.48	M	440	5.66
10	1.61	1.42	W	531	5.92
11	1.72	1.33	VVW	620	6.32
12	1.78	1.28	W	533	6.56
13	1.885	1.21	VW	444	6.93
14	1.95	1.17	VW	551/711	7.14

Data plotted in Fig. A 25, D vs $(h^2 + k^2 + l^2)^{\frac{1}{2}}$

Slope M = $\frac{K}{a_o}$ = 0.272 in.

$a_o = \frac{2.28 \text{ A}°}{0.272}$

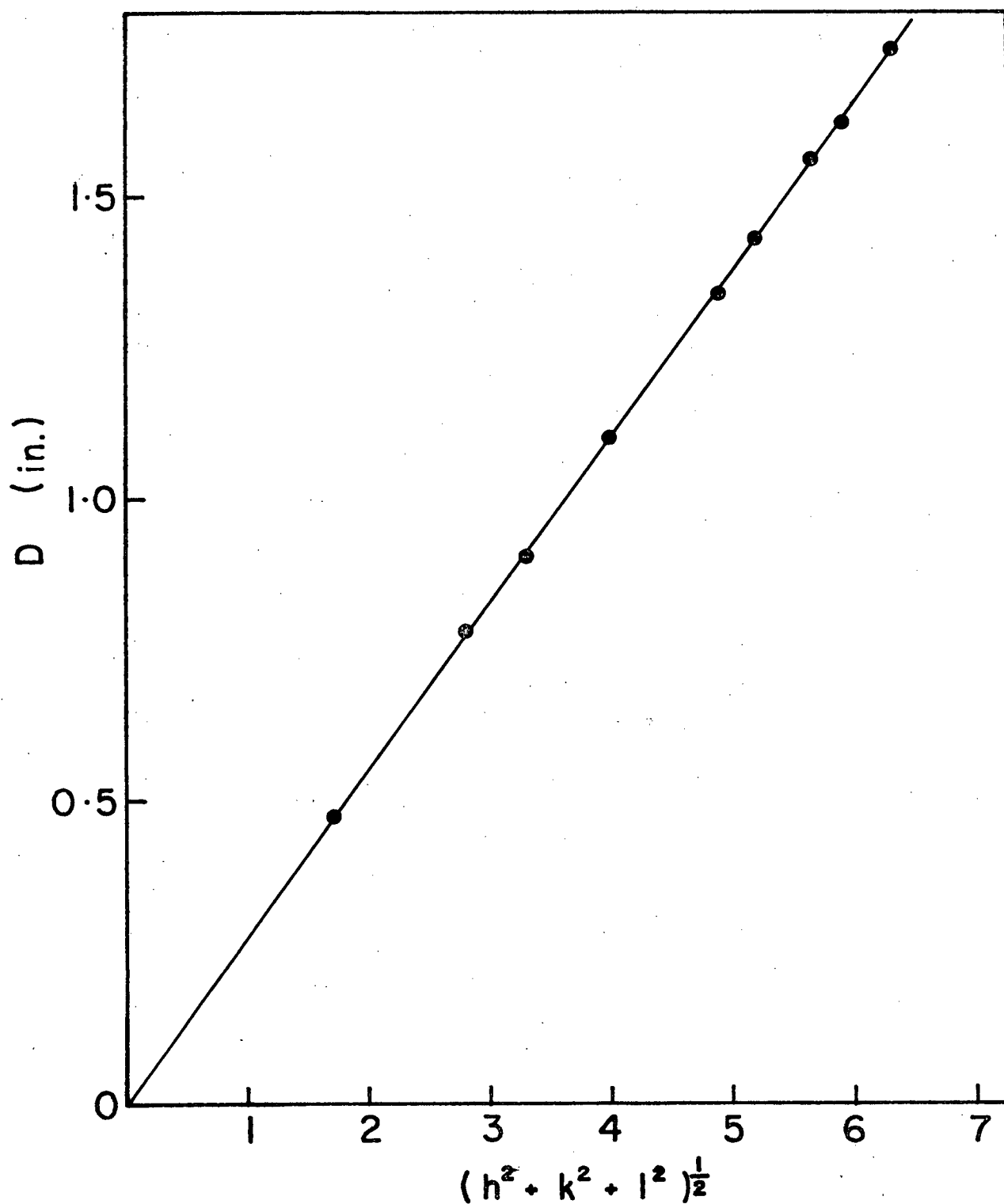Lattice parameter a_o = 8.38 A°
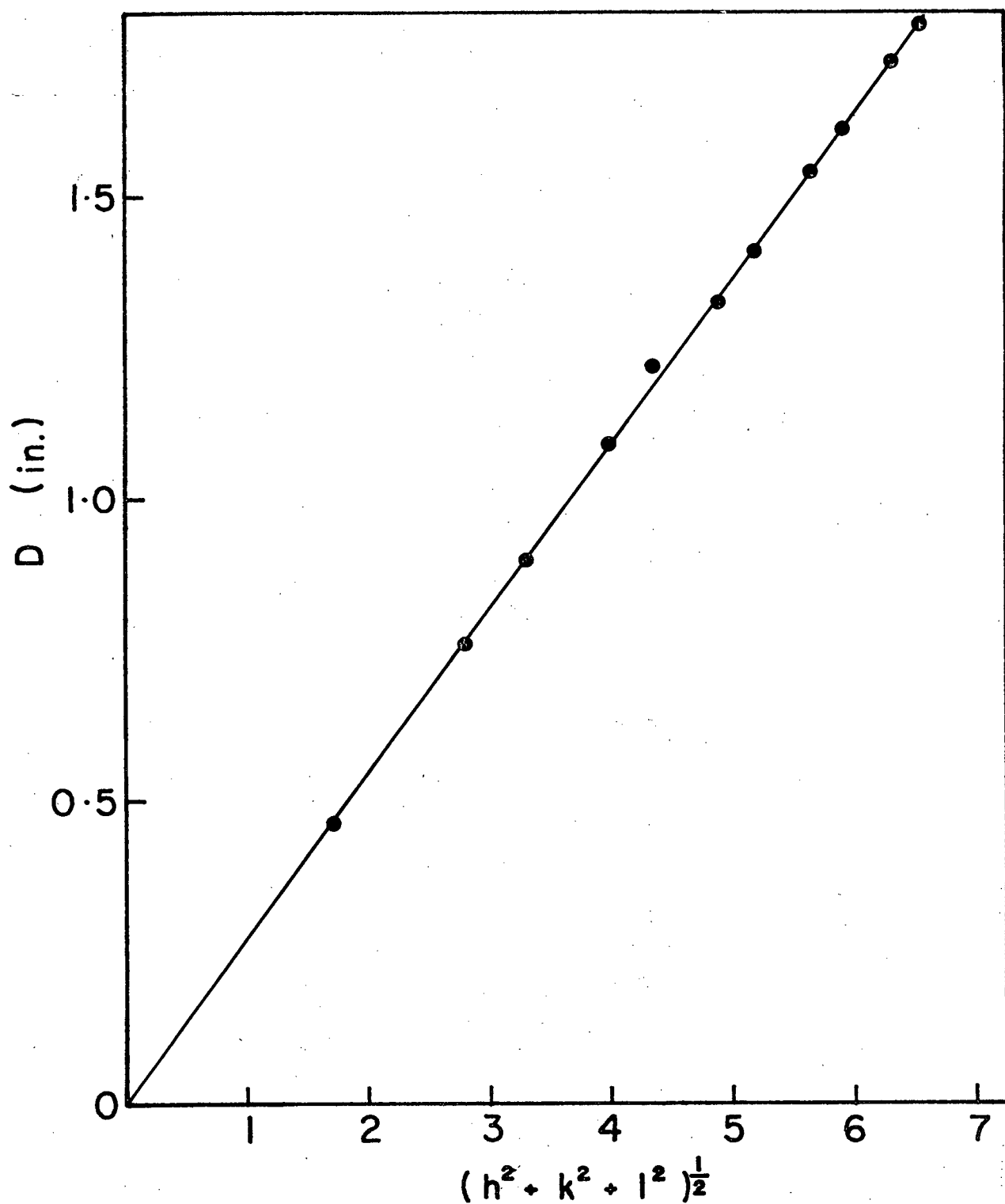
<u>Fig. A25.</u> Plot of D vs $(h^2 + k^2 + l^2)^{\frac{1}{2}}$ from Table A25. Diffraction pattern #23146, 310 s.c.c. in $MgCl_2$, oxide stripped with cellulose acetate

Table A26. 310 S.C.C. in $MgCl_2$, Oxide Stripped with Cellulose Acetate
pattern #23124   camera constant K = 2.31 ins·A°

line	D in.	dA°	I_v	$FeCr_2O_4$ (hkl)	$\sqrt{h^2 + k^2 + l^2}$
1	0.475	4.86	M	111	1.73
2	0.545	4.24	Dots	–	–
3	0.63	3.67	Dots	–	–
4	0.78	2.96	M	220	2.83
5	0.905	2.55	S	311	3.32
6	1.1	2.10	M	400	4.0
7	1.26	1.83	Dots	–	–
8	1.34	1.72	W	422	4.9
9	1.43	1.62	M	511/333	5.2
10	1.56	1.48	M	440	5.66
11	1.62	1.43	Dots	531	5.92
12	1.74	1.33	Dots	620	6.32
13	1.80	1.28	W	533	6.56

Data plotted in Fig. A26, D vs $(h^2 + k^2 + l^2)^{\frac{1}{2}}$

Slope $M = \dfrac{K}{a_o} = 0.275$ in.

$a_o = \dfrac{2.31 \text{ A}°}{0.275}$

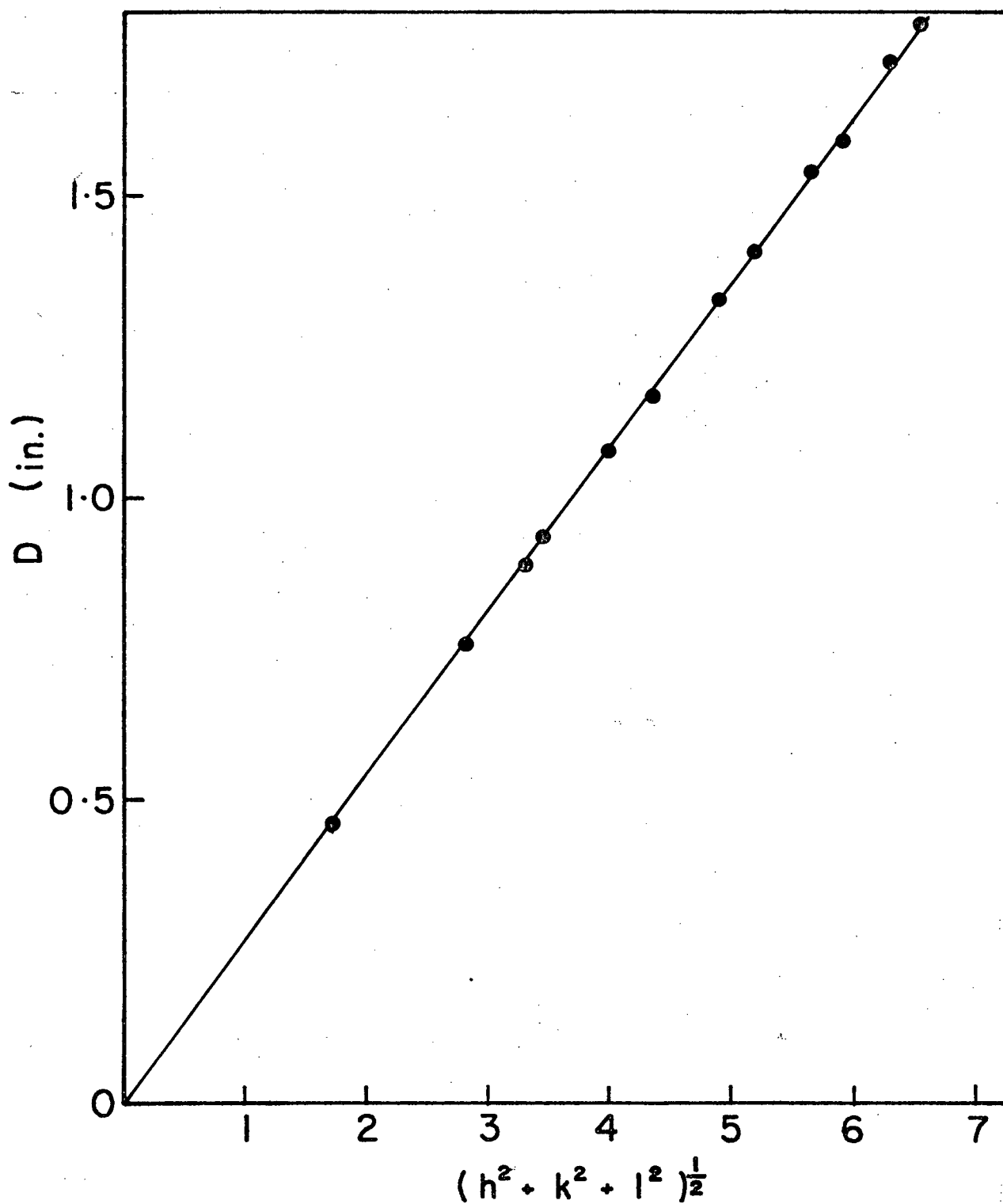Lattice parameter $a_o = 8.40$ A°

<u>Fig. A26.</u> Plot of D vs $(h^2 + k^2 + l^2)^{\frac{1}{2}}$ from Table A26. Diffraction pattern #23124, 310 s.c.c. in $MgCl_2$, oxide stripped with cellulose acetate

Table A27. 310 S.C.C. in $MgCl_2$, Oxide Stripped with Cellulose Acetate
pattern #23403   camera constant K = 2.28 ins·A°

line	D in.	dA°	I_v	$FeCr_2O_4$ (hkl)	$\sqrt{h^2 + k^2 + l^2}$
1	0.465	4.90	M	111	1.73
2	0.53	4.30	Dots	–	–
3	0.76	3.00	M	220	2.83
4	0.89	2.56	S	311	3.32
5	0.935	2.44	W	222	3.46
6	1.08	2.11	M	400	4.0
7	1.17	1.95	Dots	331	4.36
8	1.33	1.71	W	422	4.9
9	1.41	1.62	M	511/333	5.2
10	1.54	1.48	M	440	5.66
11	1.59	1.43	VVW	531	5.92
12	1.72	1.33	VVW	620	6.32
13	1.78	1.28	VW	533	6.56
14	1.84	1.24	VVW	444	6.93

Data plotted in Fig. A27, D vs $(h^2 + k^2 + l^2)^{\frac{1}{2}}$

Slope M = $\dfrac{K}{a_o}$ = 0.270 in.

$a_o = \dfrac{2.28}{0.270}$ A°

Lattice parameter a_o = 8.44 A°

Fig. A27.   Plot of D vs $(h^2 + k^2 + l^2)^{\frac{1}{2}}$ from Table A27.   Diffraction pattern #23043, 310 s.c.c. in $MgCl_2$, oxide stripped with cellulose acetate

Table A28. 310 S.C.C. in $MgCl_2$ + HCl, Oxide Stripped with 1% Bromine-
Methanol Solution
pattern #23418   camera constant K = 1.91 ins·A°

line	D in.	dA°	I_v	$FeCr_2O_4$ (hkl)	$\sqrt{h^2 + k^2 + l^2}$
1	0.40	4.78	S	111	1.73
2	0.53	3.60	Dots	-	-
3	0.65	2.94	M	220	2.83
4	0.77	2.48	VS	311	3.32
5	0.92	2.08	S	400	4.0
6	1.00	1.91	W	331	4.36
7	1.06	1.80	Dots	-	-
8	1.14	1.68	W	422	4.9
9	1.2	1.60	M	511/333	5.2
10	1.31	1.46	S	440	5.66
11	1.37	1.39	W	531	5.92
12	1.46	1.30	VW	620	6.32
13	1.51	1.26	W	533	6.56
14	1.6	1.2	M	444	6.93
15	1.65	1.16	W	711/551	7.14

Data plotted in Fig. A28, D vs $(h^2 + k^2 + l^2)^{\frac{1}{2}}$

Slope $M = \dfrac{K}{a_o} = 0.231$ in.

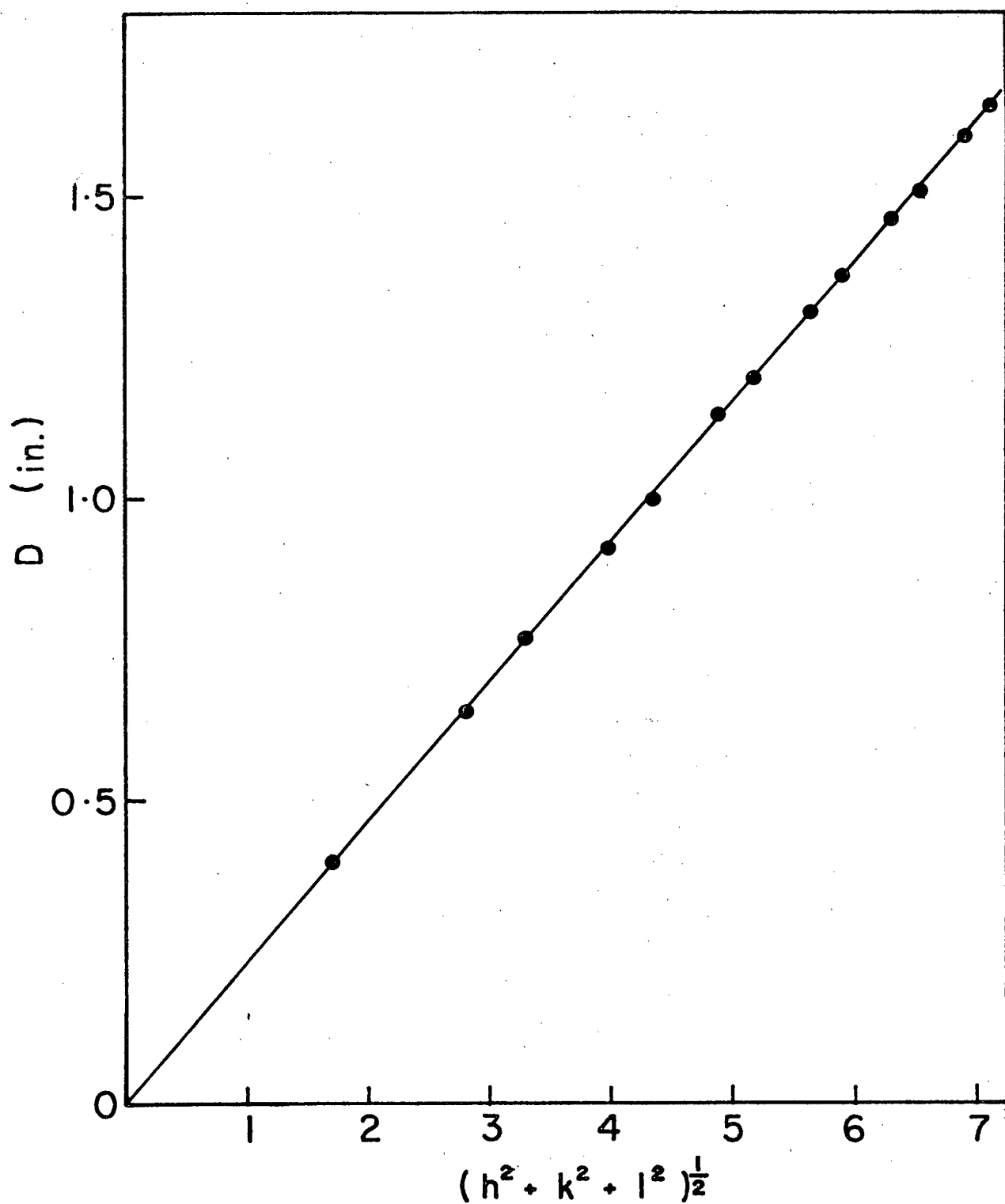$a_o = \dfrac{1.91 \text{ A°}}{0.231}$

Lattice parameter a_o = 8.27 A°

Fig. A28. Plot of D vs $(h^2 + k^2 + l^2)^{\frac{1}{2}}$ from Table A28. Diffraction pattern #23418, 310 s.c.c. in $MgCl_2$ + HCl, oxide stripped with 1% bromine-methanol solution.

Table A29. 310 S.C.C. in $MgCl_2$ + HCl, Oxide Stripped with 1% Bromine-
Methanol Solution
pattern #23417   camera constant K = 1.91 ins·A°

line	D in.	dA°	I_v	$FeCr_2O_4$ (hkl)	$\sqrt{h^2 + k^2 + l^2}$
1	0.40	4.78	S	111	1.73
2	0.66	2.90	M	220	2.83
3	0.77	2.48	VS	311	3.32
4	0.92	2.08	S	400	4.0
5	1.01	1.89	VW	331	4.36
6	1.15	1.66	VW	422	4.9
7	1.2	1.60	M	511/333	5.2
8	1.31	1.46	S	440	5.66
9	1.36	1.40	VW	531	5.92
10	1.52	1.26	W	533	6.56
11	1.61	1.19	W	444	6.93
12	1.66	1.15	W	711/551	7.14

Data plotted in Fig. A29, D vs $(h^2 + k^2 + l^2)^{\frac{1}{2}}$

Slope M = $\dfrac{K}{a_o}$ = 0.232 in.

$a_o = \dfrac{1.91 \text{ A}°}{0.232}$

Lattice parameter a_o = 8.23 A°
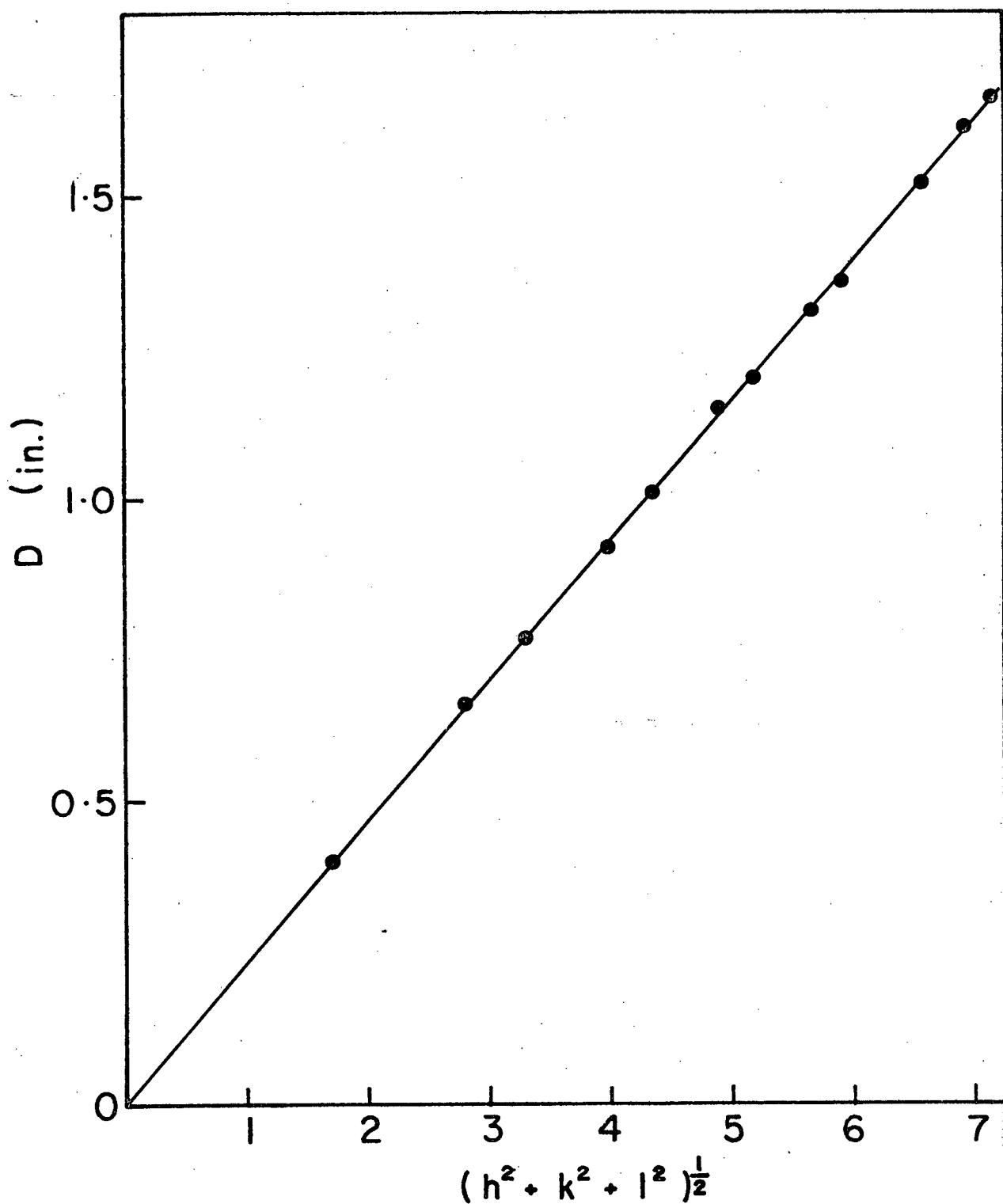
<u>Fig. A29.</u> Plot of D vs $(h^2 + k^2 + l^2)^{\frac{1}{2}}$ from Table A29. Diffraction pattern #23417, 310 s.c.c, in $MgCl_2$+ HCl, oxide stripped with 1% bromine-methanol solution.

Table A30. 310 S.C.C. in $MgCl_2$ +$CoCl_2$, Oxide Stripped with 1% Bromine-
Methanol Solution
pattern #23488   camera constant K = 1.85 ins·A°

line	D in.	dA°	I_v	$FeCr_2O_4$ (hkl)	$\sqrt{h^2 + k^2 + l^2}$
1	0.375	4.93	M	111	1.73
2	0.47	3.94	VW	–	–
3	0.61	3.03	VW	220	2.83
4	0.73	2.53	S	311	3.32
5	0.875	2.11	S	400	4.0
6	1.04	1.78	Dots	–	–
7	1.13	1.64	VW	511/333	5.2
8	1.23	1.50	M	440	5.66
9	1.42	1.30	VVW	533	6.56
10	1.50	1.23	W	444	6.93
11	1.72	1.08	W	553/731	7.68

Data plotted in Fig. A30, D vs $(h^2 + k^2 + l^2)^{\frac{1}{2}}$

Slope $M = \dfrac{K}{a_o} = 0.219$ in.

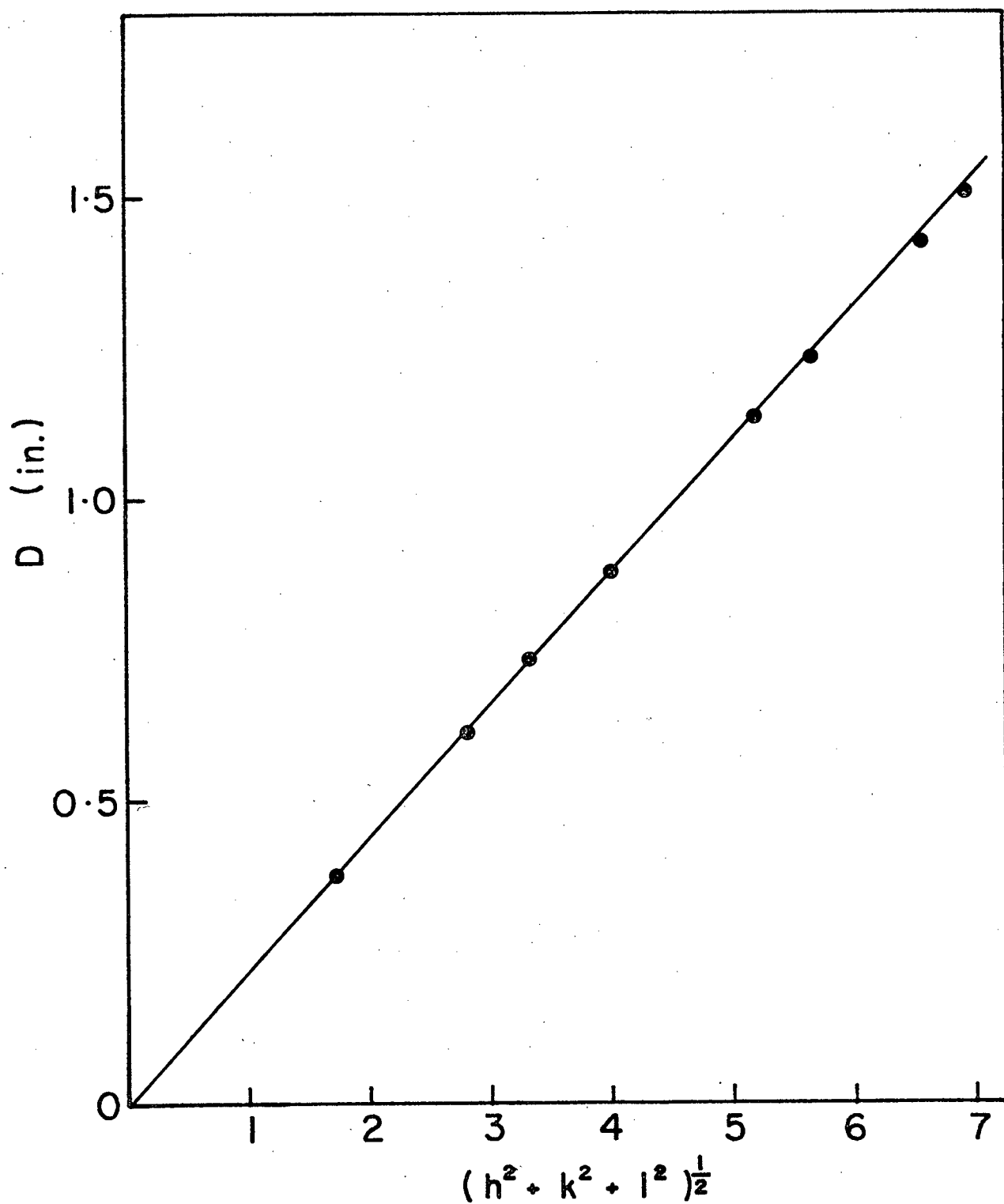$$a_o = \frac{1.85}{0.219} \text{ A°}$$

Lattice parameter $a_o = 8.45$ A°

Fig. A30. Plot of D vs $(h^2 + k^2 + l^2)^{\frac{1}{2}}$ from Table A30. Diffraction pattern #23488, 310 s.c.c. in $MgCl_2$ + $CoCl_2$, oxide stripped with 1% bromine-methanol solution.

APPENDIX B

Appendix B contains examples of x-ray spectrum taken from fracture surface oxides of the different alloys stress corroded in the various hot chloride environments. The oxides were stripped with a 1% bromine-methanol solution and examined in the scanning electron microscope at a gun voltage of 20 kv. All spectrum normalized to the chromium $K\alpha$ peak.
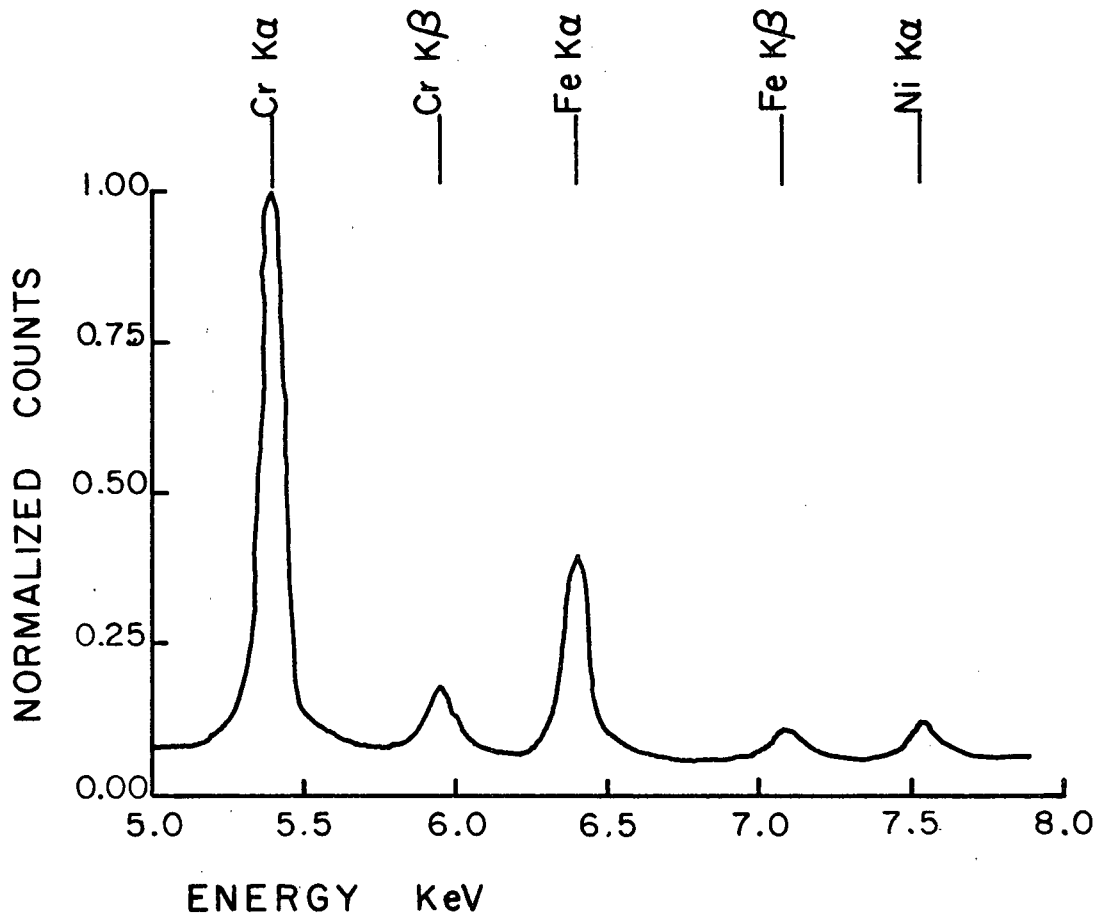
Fig. B1. S.E.M. x-ray spectrum from fracture surface oxide of type 304 stress corroded in $MgCl_2$ solution. Stripped with bromine-methanol solution.
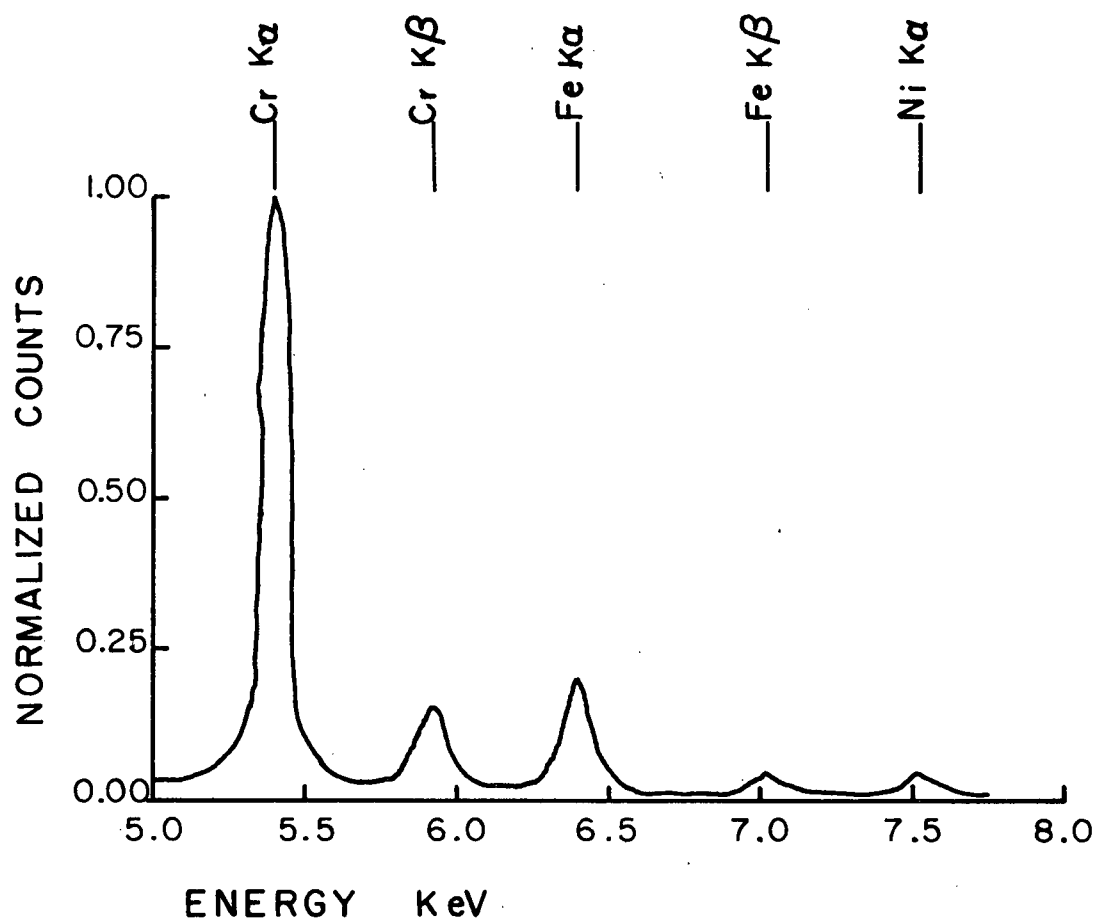
<u>Fig. B2.</u> S.E.M. x-ray spectrum from fracture surface oxide of type
304 stress corroded in $MgCl_2$ + HCl solution stripped with
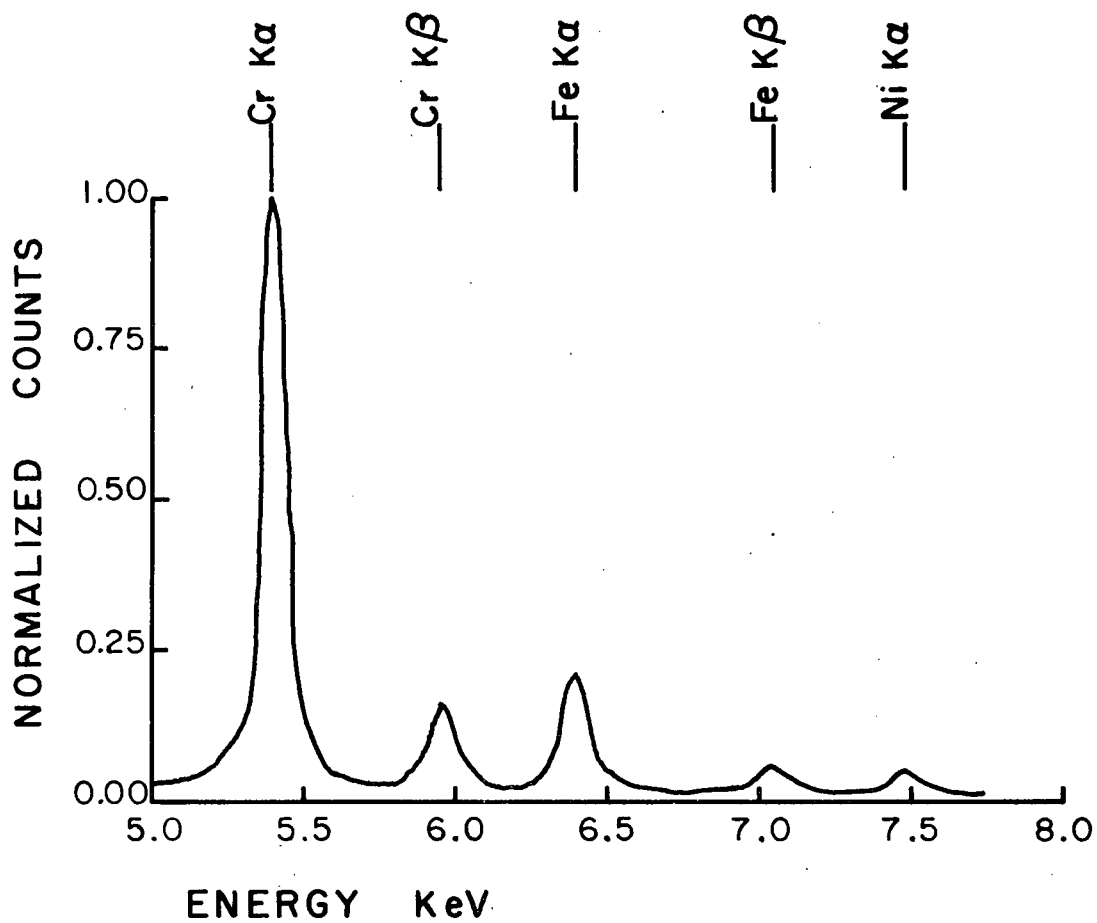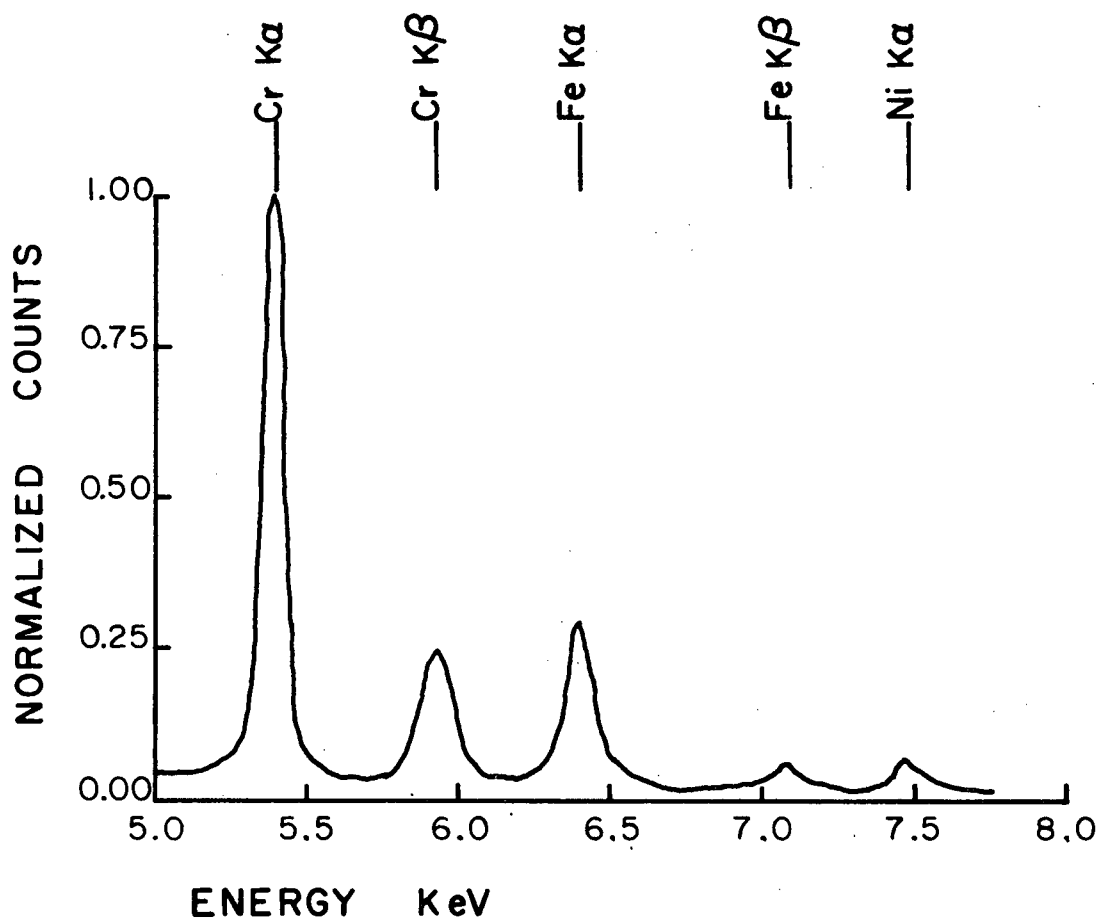bromine-methanol solution.

Fig. B3.   S.E.M. x-ray spectrum from fracture surface oxide of type 304
           stress corroded in $MgCl_2$ + $CoCl_2$ solution. Stripped with
           bromine-methanol solution.

Fig. B4. S.E.M. x-ray spectrum from fracture surface oxide of type 316 stress corroded in $MgCl_2$ solution. Stripped with bromine-methanol solution.
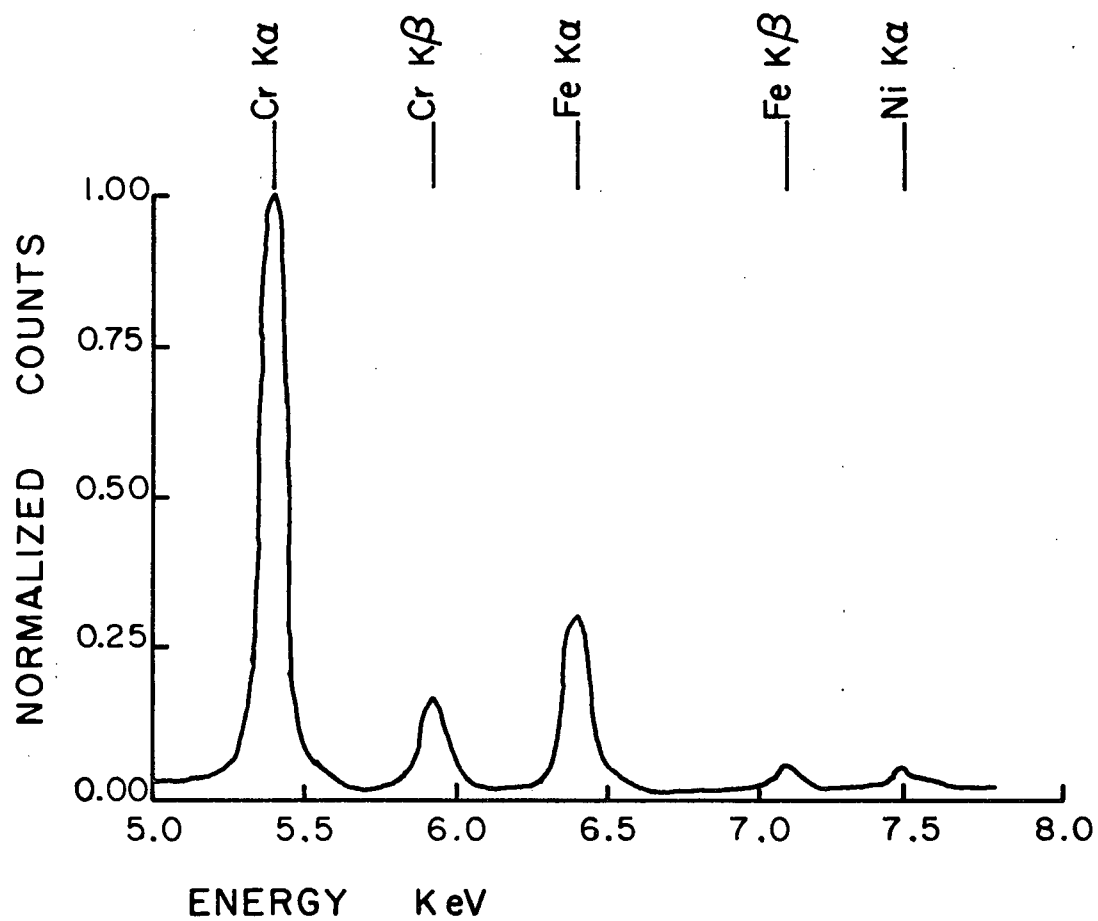
Fig. B5. S.E.M. x-ray spectrum from fracture surface oxide of type 316
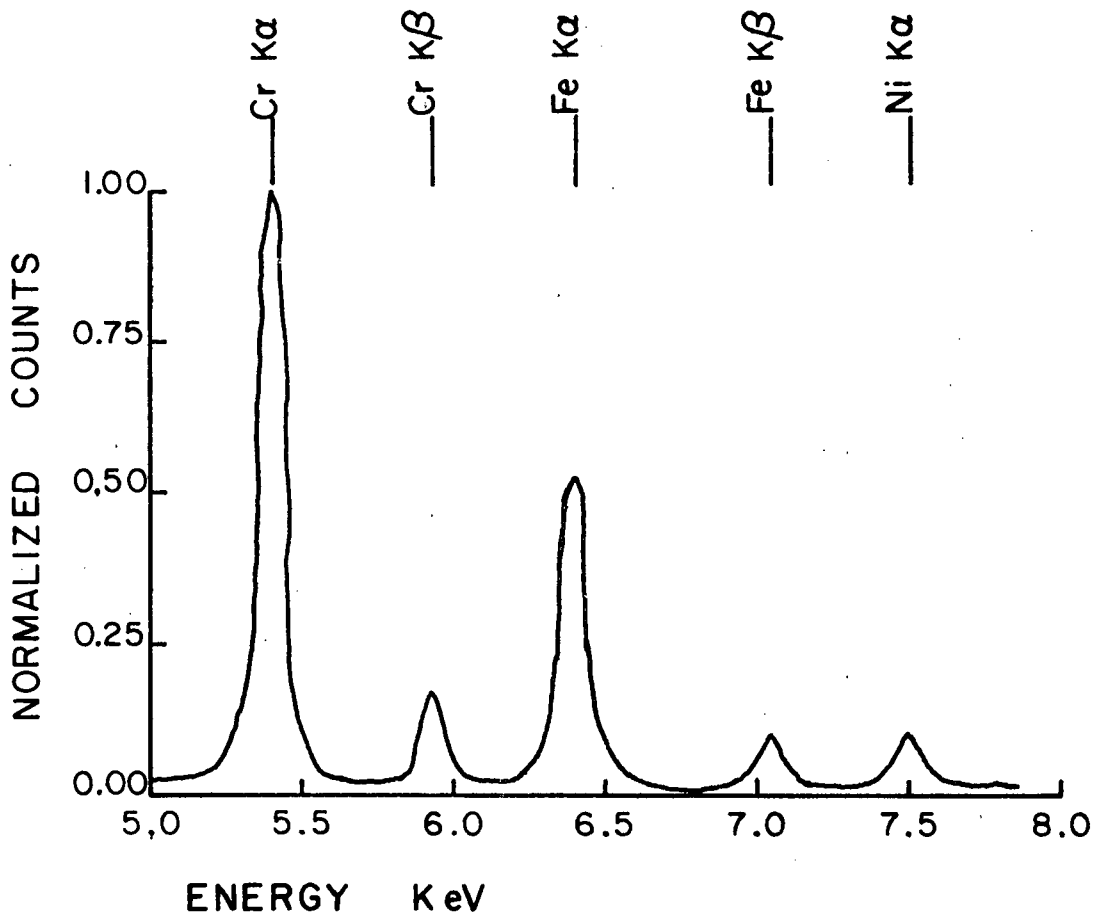stress corroded in $MgCl_2$ + HCl solution. Stripped with
bromine-methanol solution.

Fig. B6. S.E.M. x-ray spectrum from fracture surface oxide of type 316 stress corroded in $MgCl_2$ + $CoCl_2$ solution. Stripped with bromine-methanol solution.
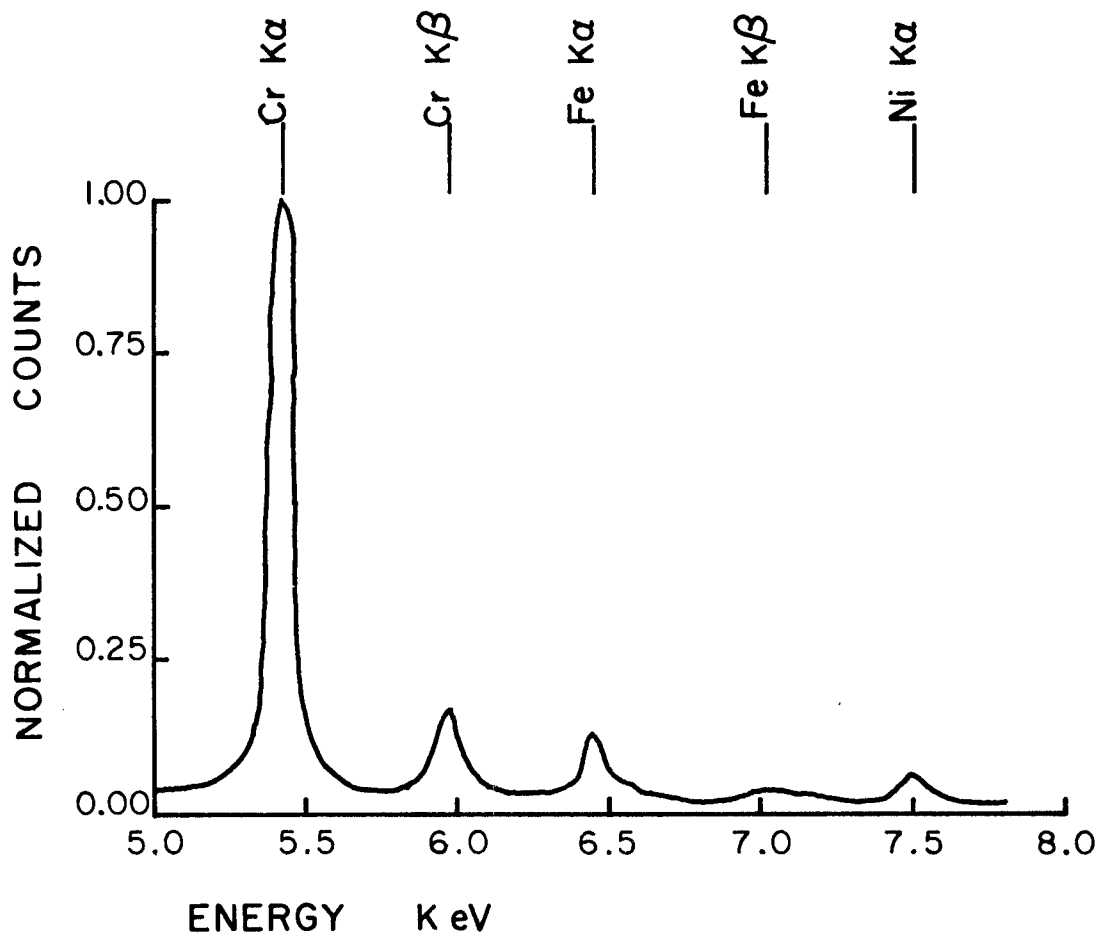
Fig. B7. S.E.M. x-ray spectrum from fracture surface oxide of type 310 stress corroded in $MgCl_2$ solution. Stripped with bromine-methanol solution.
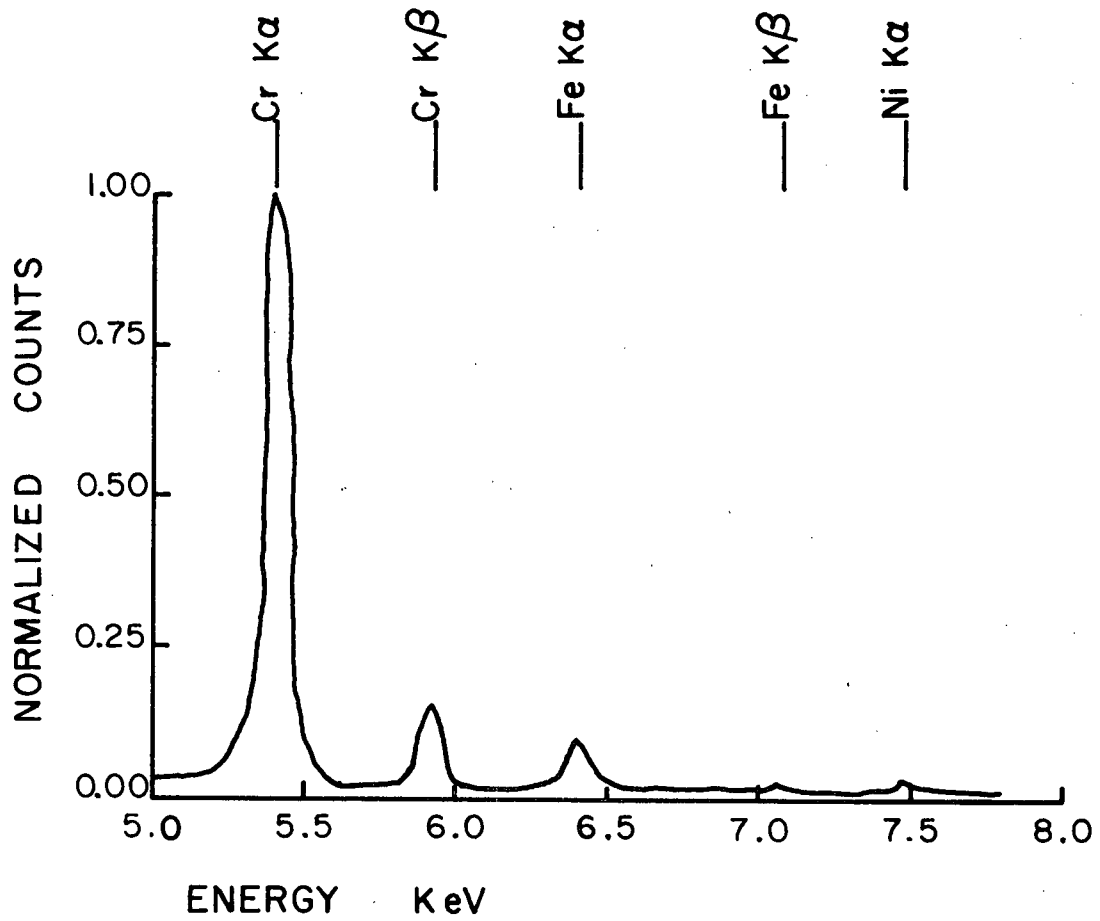
<u>Fig. B8.</u>   S.E.M. x-ray spectrum from fracture surface oxide of type 310
stress corroded in $MgCl_2$ + HCl solution.   Stripped with bromine-
methanol solution.
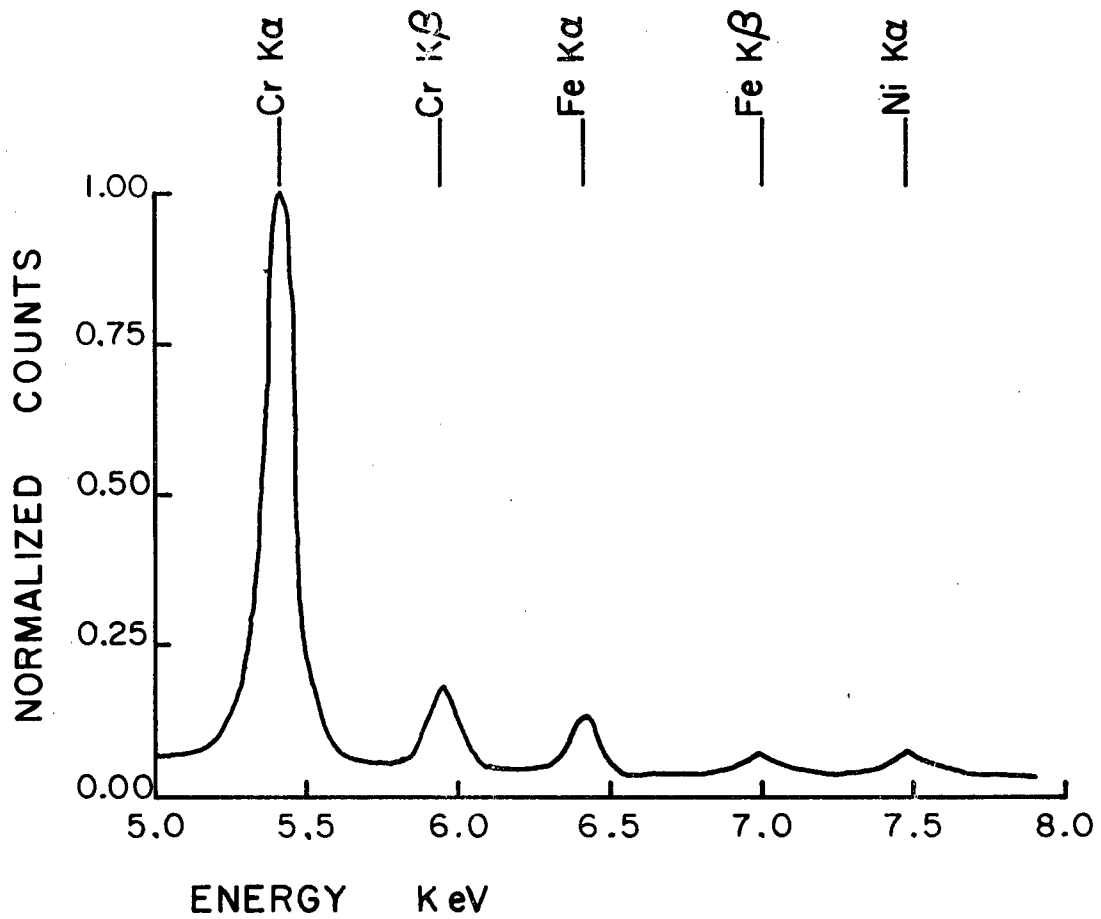
Fig. B9. S.E.M. x-ray spectrum from fracture surface oxide of type 310 stress corroded in $MgCl_2$ + $CoCl_2$ solution. Stripped with bromine-methanol solution.